UNIVERSITY OF CALIFORNIA
RIVERSIDE

Development of New Generation Eletrocatalysts for the Oxygen Reduction Reaction

A Dissertation submitted in partial satisfaction
of the requirements for the degree of

Doctor of Philosophy

in

Materials Science and Engineering

by

Yuan Wang

December 2016

Dissertation Committee:
Dr. Pingyun Feng, Chairperson
Dr. Yadong Yin
Dr. Juchen Guo

The Dissertation of Yuan Wang is approved:

_____

_____

_____

Committee Chairperson

University of California, Riverside

Acknowledgement

The past four years are one of the most important periods of my lifetime. It witnessed the growth of my knowledge, the broadening of my horizon in life, and the deepening of my understanding in philosophy. I wish to express my sincere appreciation to those who have contributed to this thesis and supported me in one way or the other during this amazing journey.

First of all, I would like to express my special appreciation and thanks to my advisor Prof. Pingyun Feng. You have been a tremendous mentor for me. I would like to thank you for encouraging my research and for allowing me to grow as a research scientist. Your guidance, all the useful discussions and brainstorming sessions, especially during the difficult conceptual development stage helped me at various stages of my research. Your advice on both research as well as on my career have been priceless.

I would also like to thank my committee members, Prof. Yadong Yin and Prof. Juchen Guo for serving as my committee members. I want to thank you for letting my defense be an enjoyable moment, and for your brilliant comments and suggestions.

I am also grateful to Materials Science and Engineering program and Chemistry department for giving me the opportunity to carry out my doctoral research and use the facilities. I am also honored that I was appointed to the Ph.D. part time teaching assistant and research assistant in the school during my four years' study which was valuable memory ever.

I am greatly indebted to many past and current members of Prof. Feng's group and my collaborators for their creating a rich working experience, intellectual stimulation and friendship: Dr. Aiguo Kong, Dr. Qipu Lin, Dr. Quanguo Zhai, Dr. Chengyu Mao, Dr. Xiang Zhao, Dr. Fan Zuo, Dr. Yang Hou, Dr. Jian Guo, Dr. Shuanghong Tian, Dr. Dezhi Chen, Dr. Koroush Sasan, Dr. Jikai Liu, Dr. Xiao Wei, Dr. Na Li, Dr. Zhonghua Li, Dr. Fei Bu, Dr. Dongsheng Liu, Dr. Quan Huo, Dr. Hai Yang, Dr. Mingming Zheng, Dr. Guoping Yang, Dr. Wei Jiao, Xitong Chen, Zhao Zhao, Shilei Xie and Yanxiang Wang.

At last, a special thanks to my family. Words cannot express how grateful I am to my father, my mother and all my family members for all of the sacrifices that you've made on my behalf. Your love for me was what sustained me thus far. I would also like to thank all of my friends who supported me on the way, and incented me to strive towards my goal.

Dedication

To My FAMILY

ABSTRACT OF THE DISSERTATION

Development of New Generation Eletrocatalysts for the Oxygen Reduction Reaction

by

Yuan Wang

Doctor of Philosophy, Graduate Program in Materials Science and Engineering
University of California, Riverside, December 2016
Dr. Pingyun Feng, Chairperson

Development of non-precious metal catalysts (NPMCs) has become a well-known strategy to replace the platinum-based catalysts for the oxygen reduction reactions at the cathode of fuel cells, metal–air batteries and air-breathing cathodes in industrial electrocatalytic processes. There are two crucial factors governing the performance of carbon based catalysts. One is the intrinsic nature of the active sites which are determined by the selection of the doping elements. Another important factor is the large specific area and porous structure feature which can introduce more active sites and promote the electrons and oxygen species transportation. Among numerous carbon-based electrode materials, hollow carbonaceous spheres have attracted attention due to the high surface-to-volume ratios and more accessible active sites on the shell. Here, hierarchical porous carbon-nanoshells with about 40 nm cavities are synthesized by using CdS@mSiO_2 core-

shell structured materials as hard templates and 4, 4'-bipyridine, $FeCl_3$ as nitrogen, carbon and iron sources. This method demonstrates outstanding stability and electrocatalytic activity for ORR.

Moreover, Metal–organic frameworks (MOFs) as new classes of crystalline porous materials with high surface area, large pore volume and uniform pore distribution can be suitable candidates as precursors and/or templates for the formation of high quality porous carbons for ORR application. The diversity in types of metal ions and organic ligands in MOFs with cavities and pore spaces make them versatile precursors and/or templates for the synthesis of carbon/metal oxide composites and doped carbon-metal materials.

Apart from the above-mentioned advantages, there are some open coordination sites on the metals species or functional groups in the ligands of the developed MOFs. Those open coordination sites can function as the specific interaction sites and be further utilized for the post-synthesis to introduce different heteroatoms with different coordination environments and different functionalities. Targeted species, like metals, heterometals and heteroatoms can be integrated into the targeted materials via different interactions to further maximize the electrocatalytic activities of the synthesized materials.

Table of Contents

List of Figures

List of Tables

List of Schemes

CHAPTER ONE: AN INTRODUCTION TO FUEL CELLS AND OXYGEN REDUCTION REACTION

1.1 Fuel Cell Technology

1.1.1 Fuel Cell Basics

A fuel cell is an electrical cell, which convert hydrogen, or hydrogen-containing fuels, directly into electrical energy plus heat through the electrochemical reaction of hydrogen and oxygen into water.[1] Fuel cell technology is based upon the simple reaction given in Eq. (1.1):

$$H_2(gas) + O_2(gas) \rightarrow 2\ H_2O + energy \quad (Eq.1)$$

In theory, a fuel cell will produce electricity if fuel is constantly supplied. The basic design of a fuel cell involves two electrodes on either side of an electrolyte. Hydrogen and oxygen pass over each of the electrodes and through means of a chemical reaction, electricity, heat, and water are produced. Because hydrogen and oxygen gases are electrochemically converted into water, fuel cells have many advantages over heat engines. These include: high efficiency, virtually silent operation and, if hydrogen is the fuel, there are no pollutant emissions. If the hydrogen is produced from renewable energy sources, then the electrical power produced can be truly sustainable.

1.1.2 The Chemistry of a Single Cell

Among all the existing fuel cells, the proton exchange membrane fuel cell (PEMFC) has been actively developed for use in vehicles, portable electronics, and combined heat and power (CHP) systems due to its simplicity, low working temperature, high power density, and quick start-up.[2, 3] In a PEM fuel cell, two half-cell reactions take place simultaneously, an oxidation reaction (loss of electrons) at the anode and a reduction reaction (gain of electrons) at the cathode. These two reactions make up the total oxidation-reduction (redox) reaction of the fuel cell, the formation of water from hydrogen and oxygen gases. The anode and cathode are separated by an electrolyte, which allows ions to be transferred from one side to the other (Figure 1.1). The electrolyte in a PEM fuel cell is a solid acid supported within the membrane. The solid acid electrolyte is saturated with water so that the transport of ions can proceed.

PEM Fuel Cell:

Anode reaction: $H_2 \rightarrow 2H^+ + 2e^-$ (Eq. 2)

Cathode reaction: $\frac{1}{2}O_2 + 2e^- + 2H^+ \rightarrow H_2O$ (Eq. 3)

Overall reaction: $H_2 + 1/2\ O_2 \rightarrow H_2O$ (Eq. 4)

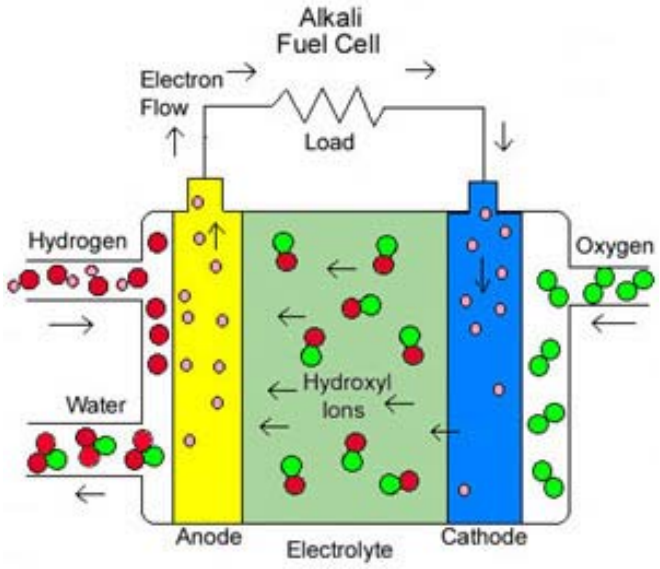

Figure 1.1 Schematics of a fuel cell. Reprinted with permission from Ref 2. Copyright 2015 American Chemical Society

1.2 Oxygen Reduction Reaction based on Rotating Disk Electrode

In fuel cells, at the anode the hydrogen molecules first come into contact with a platinum catalyst on the electrode surface. At the cathode, oxygen molecules come into contact with a platinum catalyst on the electrode surface. The reaction rate of HOR on the anode is very fast that the loading amount of Pt can be less than 0.05 mg cm^{-2}. However, the reaction rate of ORR on the cathode has sluggish reaction kinetics. It requires much more Pt loading (~0.4 mg cm^{-2}) to achieve a desirable fuel cell performance.[4] Since Pt is scares and expensive, reducing its loading or even completely replacing it with an

abundant and cheap metal or other materials would be advantageous for future fuel cell application. Nowadays, more and more efforts are led to the development of less expensive and more abundant electrocatalysts for oxygen reduction reaction for PEMFCs. These include advanced Pt alloys and carbon-based non-noble metal composite catalysts.

In theory, newly researched ORR catalyst should be applied in fuel cell environment and then evaluated and compared with benchmark, like the state-of-the-art Pt/C. However, applying the new developed ORR catalyst into a fuel cell is impractical due to that the membrane electrode assembly (MEA) fabrication and test require special skills, equipment, and abundant materials which is not suitable at the lab scale. In practical case, a ring-disk electrode (RDE) with a glassy carbon disk and a Pt ring was served as the substrate for the working electrode (Figure 1.2).[5-7] The catalyst ink was prepared by mixing the catalyst powder with Nafion solution (5wt %) and ethanol in an ultrasonic bath. Then catalyst ink was pipetted onto the GC electrode. As a comparison, commercial 20 wt. % platinum on Vulcan carbon black (Pt/C from Alfa Aesar) was prepared by blending Pt/C (10 mg) with 80 μL Nafion solution (5wt %) and 1.2 ml ethanol in an ultrasonic bath. A Pt loading about 20 μg cm^{-2} was applied in both alkali and acid conditions. To mitigate the mass transfer effect during ORR activity measurements, glassy carbon electrodes are rotated to increase the mass transfer rates of O_2 at the electrode surface. The intrinsic activity (kinetic current without mass transfer effect) of the catalysts can be derived according to the Koutecky−Levich equation:

$1/j=1/j_L+1/j_K$

$j_L=0.62nFCD^{2/3}\upsilon^{-1/6}w^{-1/2}=Bw^{-1/2}$

$1/j=1/Bw^{-1/2}+1/j_K$

where $B=0.62nFC_0\ D_0^{\ 2/3}\ \upsilon^{-1/6}$, j was the measured current density, j_K and j_L were the kinetic- and diffusion-limiting current densities, *w* was the rotation speed, *n* was the electron transfer number, *F* was the Faraday constant (*F* = 96485 C mol^{-1}), C was the bulk concentration of O_2, D was the diffusion coefficient of dissolved oxygen, v was the kinematic viscosity of the electrolyte.

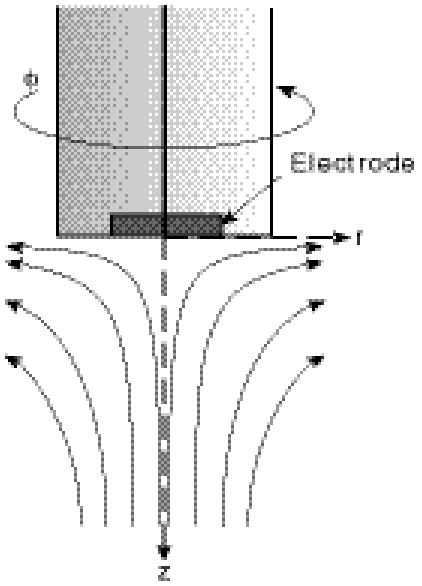

Figure 1.2 Diagram of Ring Disc Electrode (RDE)

1.3 Pt-based catalyst

The oxygen reduction reaction occurring at the cathode of proton exchange membrane fuel cells (PEMFCs) and metal-air batteries is a bottleneck reaction for the commercialization of these energy techniques. Currently, platinum and platinum-based alloys are the most efficient catalysts for the oxygen reduction reaction (ORR). However, the high cost, scarcity, low tolerance to methanol fuel, and poor stability of Pt-based materials hinder the widespread utilization of these noble metal cathode catalysts. To have effective Pt-based catalysts for ORR, rational optimizing the intrinsic reactivity of Pt-involved active sites and maximizing their utilization based on the understanding of mechanism of ORR are two important factors.[8] Since the surface electronic properties and electronic surface atomic arrangement or coordination of the catalyst are important for ORR, surface properties engineering, including the surface electronic structure and atomic arrangement of the catalysts, can be believed to effectively tune both activity and durability of Pt catalyst.[9]

Generally, four routes can be applied to control the surface structure properties of Pt: (i) controlling the exposed facet (or the shape) of Pt nanocrystals and thus maximizing expression of the facetsmost active towards ORR. Single Pt electrodes show different ORR activity at different crystal facets. Studies of structure sensitivity of ORR on the Pt low-index single-crystal surfaces in perchloric acid revealed that in nonadsorbing $HClO_4$ electrolytes, single crystal Pt (110), (111), and (100) surfaces were observed to have the

activity for ORR following a descending order.[10] (ii) Pt can be combining with another metal to generate multimetallic nanocrystals with structures in the form of alloys, core–shells, branches or anisotropies. It is expected that a bimetallic system can display not only a combination of the properties associated with each distinct metal, but also new or unexplored properties due to a possible synergistic effect between each metal.[11-12] In addition, the final performance can be boosted by reasonable selection of the alloy metals and the precise control of the size, compositional profile and inner structures of this Pt-based system. Many Pt-based alloy systems such as PtPd, PtAu, PtAg, PtCu, PtFe, PtNi, PtCo and PtW, have been studied and accordingly improved ORR activities of these alloy systems have been reported (Figure 1.3 and Figure 1.4). It is shown that catalysts with a lower content of expensive Pt metal can not only inherit the properties of the Pt constituent but also usually show a superior performance when compared with monometallic Pt.[13-14]

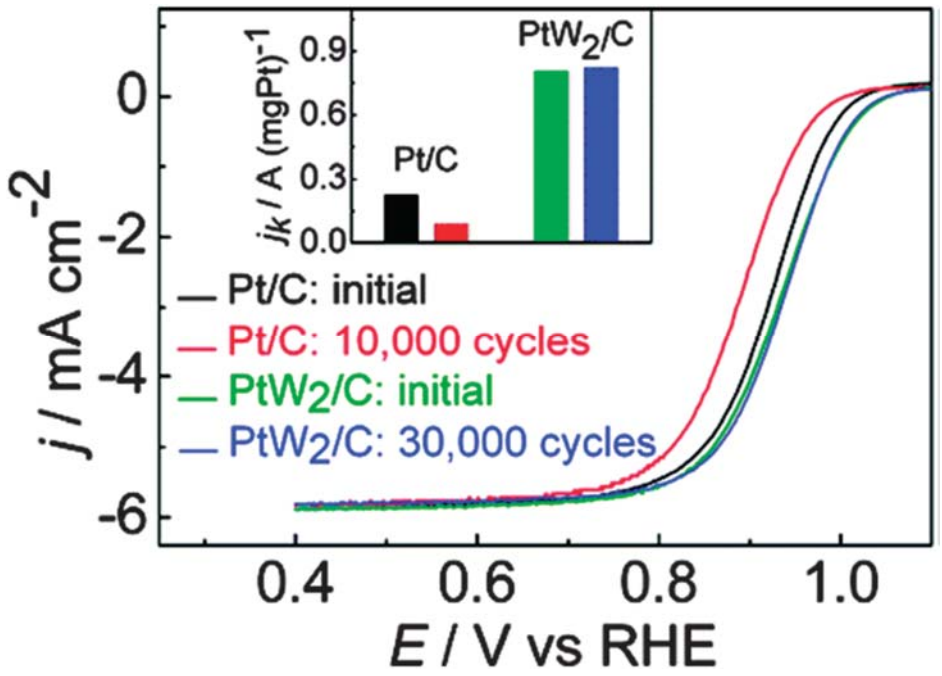

Figure 1.3 ORR polarization curves before and after 30000 cycles of potential cycling for Pt/C and PtW_2/C catalysts in O_2-saturated 0.1 M $HClO_4$ at 1600 rpm. Reprinted with permission from Ref.15. Copyright 2011, American Chemical Society.

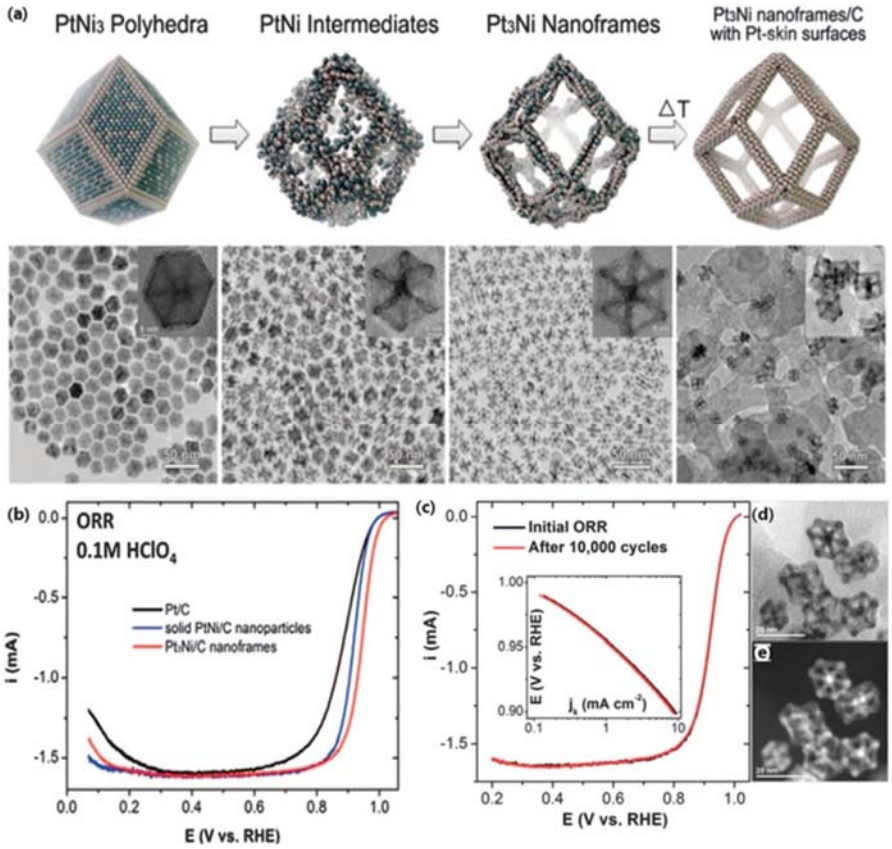

Figure 1.4 (a) Schematic illustrations and corresponding TEM images of the samples obtained at four representative stages during the evolution process from polyhedra to nanoframes. (b) ORR polarization curves. The ORR activity (c) and TEM images of Pt3Ni nanoframes before (d) and after (e) the stability test. Reprinted with permission from Ref. 16. Copyright 2014, American Association for the Advancement of Science.

(iii) In addition to modulating exposed facets of Pt nanocrystals and combining Pt with other metals to generate bimetallic nanocrystal with structures in the form of alloys, core–shells branches or anisotropies, another way is to modifying Pt nanoparticle surfaces with elaborately selected foreign species, such as metal clusters, molecules, ions, organic or inorganic compounds.[17-26] For example, modifying Pt nanoparticles with Au clusters has been already proved to be efficient in stabilizing Pt against dissolution under harsh fuel cell work environment (Figure 1.5).[17]

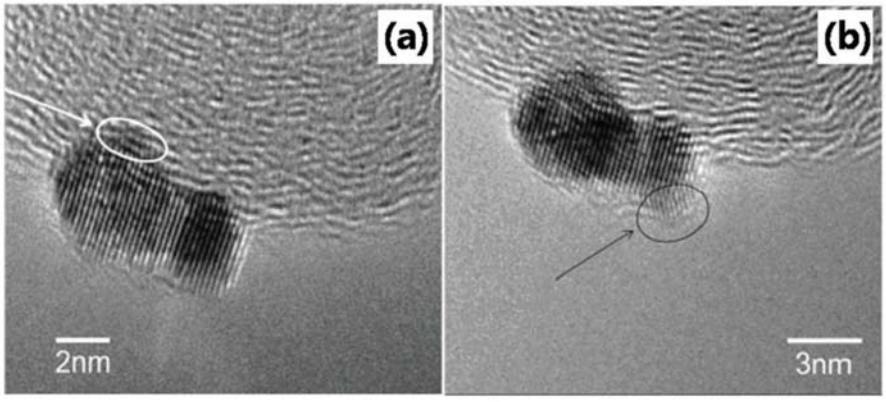

Figure 1.5 Electron micrographs of a Au-modified Pt/C catalyst made by displacement of a Cu monolayer by Au. High-resolution images (a) and (b) show atomic rows with spacings that are consistent with the Pt(111) single crystal structure. Reprinted with permission from ref. 17. Copyright 2007, American Association for the Advancement of Science.

(iv) A catalyst support with high corrosion resistance and with strong interactions with the supported metallic catalyst can be applied to Pt. Currently, the most commonly used support for ORR catalyst is the carbon black.[27-28]

1.4 Pt-free catalyst

1.4.1 Transition metal–nitrogen–carbon catalysts

Since cobalt phthalocyanine as the ORR electrocatalyst in alkaline electrolytes in 1964 reported by Jasinski, carbon-supported non-precious metal (Co, Fe, etc.) and metal-free catalyst to replace the expensive Pt-based electrode in fuel cells started.[29] Among non-precious metal catalysts, Fe, N-codoped carbon-based (Fe/N/C) electrocatalysts (Fe-based catalysts) are the most promising candidates because the state-of-the art Fe-based catalysts exhibit much higher ORR activity and durability than those of Pt-Based catalysts in alkaline electrolytes and comparable ORR activity in acidic media.[30, 31] Due to the excellent ORR activity obtained by diverse Fe-based catalysts, the ORR mechanisms along with the achievement of the ORR activity on Fe-based catalysts were widely studied by many groups.

Research in Fe-based catalysts include the non-pyrolyzed Fe-based macrocycle compounds and pyrolyzed Fe-based macrocycle compounds or some proper Fe- and N-containing precursor materials. The former is important for fundamental understanding

due to their preserved well-defined structure during synthesis procedures. While the latter shows a higher ORR catalytic activity because of the introduction of high temperature heat treatment procedures to the catalyst synthesis process. The structures of active sites on these Fe-based catalysts have been proposed by different groups including the structure of in-plane coordination of an iron atom and four pyridinic or pyrrolic type of nitrogen atoms embedded in a graphene-type matrix (Fe–N_4/C or Fe–N_{2+2}/C), the structure of coordination of an iron atom and two pyridinic type of nitrogen atoms embedded in a graphene-type matrix (Fe–N_2/C) and N-doped carbon-based structure (N–C).[32-39] However, there is still an ongoing debate about the active sites of these materials because of different preparation protocols used for Fe-based catalysts. There is still a long way to go to reach the practical usage and understanding of Fe-Based catalysts in fuel cells.

The factors of influence on ORR catalytic activity and stability of Fe-based catalysts have also been studied such iron and nitrogen sources, heat-treatment conditions, Fe content and carbon support properties including surface nitrogen content and microporosity. Among them, two crucial factors govern the performance of Fe–N–C catalysts, as follows: (I) the elemental composition and the interactions between different components, which determine the intrinsic nature of active sites. (II) Specific surface area and porous structure, which determine the accessible part of active sites and the transport properties of ORR-relevant species. Introducing well-defined nanoporous structures is an effective way can solve this problem. Muellen and Feng et al. prepared a family of

mesoporous nonprecious metal catalysts for ORR in acidic media, including cobalt–nitrogen–doped carbon (C–N–Co) and iron–nitrogen–doped carbon (C–N–Fe), by employing vitamin B12 (VB12) and the polyaniline–Fe (PANI–Fe) complex as precursors.[40] Silica nanoparticles, ordered mesoporous silica SBA-15, and montmorillonite were used as templates for achieving mesoporous structures (Figure 1.6).

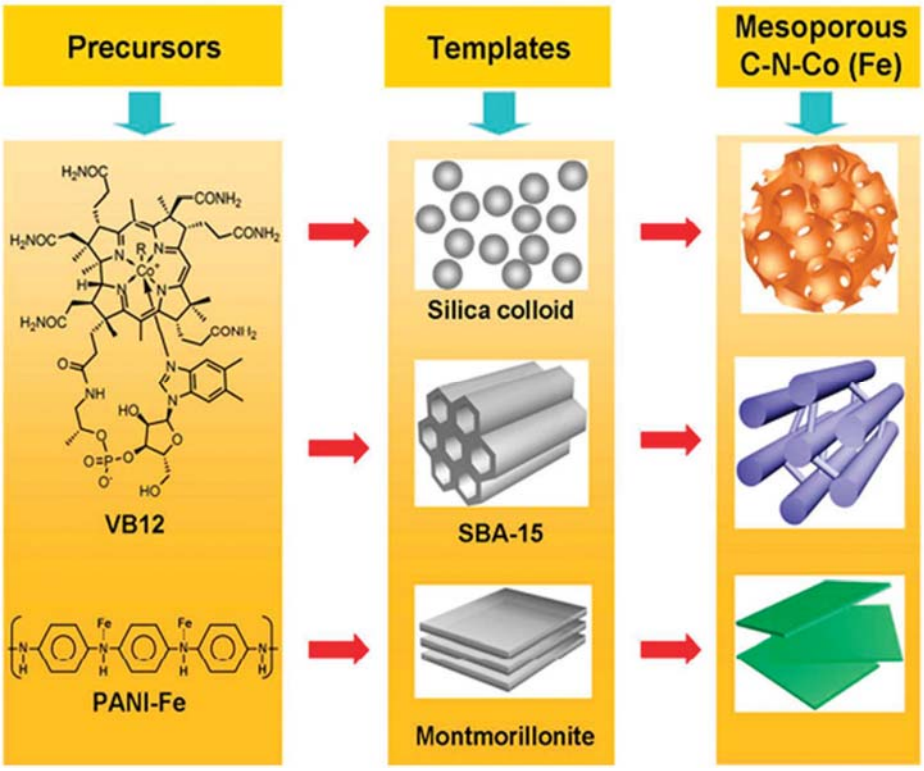

Figure 1.6 Templating synthesis of mesoporous C–N–Co (Fe) catalysts for ORR. Reprinted with permission from ref. 40. Copyright 2013, American Chemical Society.

1.4.2 Metal free catalysts

Metal free catalysts are various carbon-based materials such as graphite, graphene, carbon nanotubes and ordered mesoporous carbon with a series of heteroatoms, such as B, N, S, Se, P, and F, plenty of doped carbon-based catalysts, including dual-doped and trinary-doped.[41-51] The series of heteroatoms can tune the intrinsic property of these carbon materials. Among the above various dopants, the N dopant is the most popular dopant. The catalytic mechanism of different doped carbon catalysts is complicated. Dai et al. proposed that the high activity of nitrogen doped carbon (NC) catalysts may be attributed to the larger electronegativity of N (electronegativity of nitrogen: 3.04) with respect to C atoms (electronegativity of carbon: 2.55), and the creating of positive charge density on the adjacent C atoms. These factors may result in the very favorable adsorption of O_2.[42]

In an NC-based catalyst, the molecular structure of nitrogen seems to play a critical role in affecting the properties of the N-doped nanocarbon materials. A schematic representation of the common N bonding configurations is illustrated in Figure 7. Pyridinic N and pyrrolic N atoms are located at edge or defect sites; they do not increase the number of electrons in the delocalized p-system. Graphitic N atom substitutes carbon atom within the graphitic structure. Therefore, they have the same configuration as graphitic carbon atoms but they introduce extra electrons in the delocalized p-system. Pyridinic N can also be present in its oxidized form. These different N-functionalities are

often coexisting and their concentrations are practically adjustable. Among these N functionalities, pyridinic, pyrrolic, and graphitic N are generally believed to contribute to the ORR catalytic activity (Figure 1.7).[50]

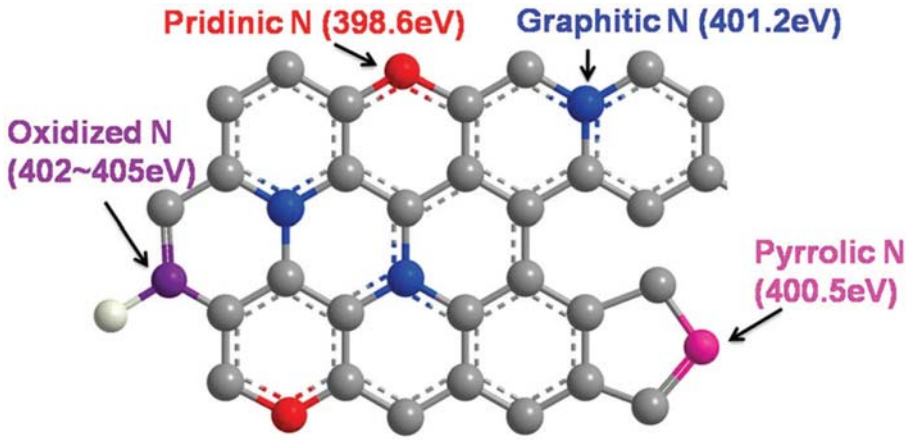

Figure 1.7 Schematic representation of the common N bonding configurations. Reprinted with permission from ref. 50. Copyright 2013 Wiley-VCH Verlag GmbH & Co. KGaA, Weinheim.

Generally, nitrogen doped carbon materials are prepared through three different routes. First, nitrogen atom can be in situ doped into carbon framework upon the formation of graphitic plane via processes like chemical vapor deposition (CVD).[52-54] Although high nitrogen content in carbon materials can be made in this approach, it is not practicable for mass production of the catalysts. Second is the post-heating graphitic carbon, including carbon nanotubes (CNTs), graphene and fullerene, with nitrogen-containing substances.[55, 56] However, due to the incorporation resistance from pre-existing graphitic

structure, the nitrogen fraction is usually too insufficient to make enough catalytic sites. Third is direct pyrolysis of organic nitrogen-rich precursors with well-defined uniform N-containing structures, such as graphitic carbon nitride, melamine foam and polymer framework which is the most popular method used nowadays due to its facile managed preparation technology.[57] However, limited formation of the ORR active sites and relatively poor transport properties can be obtained by this method since direct pyrolysis of the nitrogen precursors at high temperature frequently leads to remarkable loss of active N species and fails in controlling the inner porous structure (Figure 1.8).

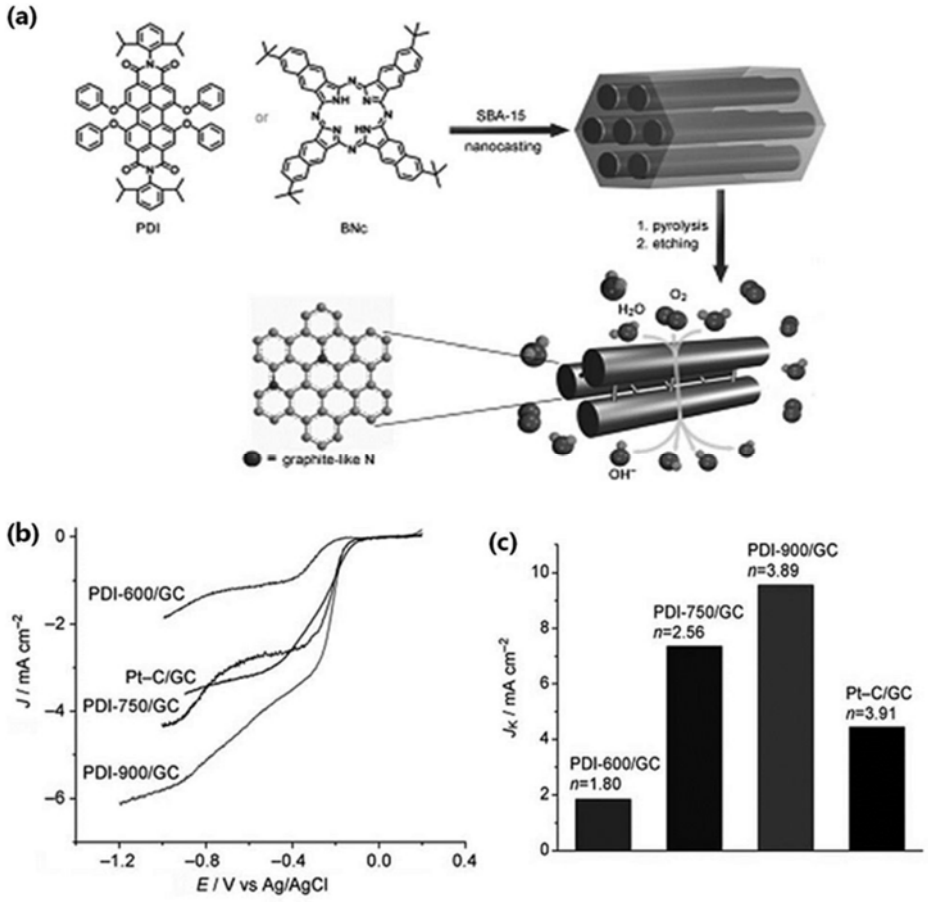

Figure 1.8 Preparation of nitrogen-doped ordered mesoporous graphitic arrays as metal-free catalysts for the ORR. Reprinted with permission from ref. 46. Copyright 2010 Wiley-VCH Verlag GmbH & Co. KGaA, Weinheim.

1.4.3 Metal-Organic Framework-based nanomaterials

Easy access of the O_2 species to the active species along with large exposure of the catalyst surface atoms is the basic for the developed ORR catalyst. Metal Organic Frameworks (MOFs) which can provide an extremely high surface area framework with

active metal centers should ensure ease access for the O_2 species while active metal centers act as basis for catalysis reaction. However, pristine MOFs exhibit poor conductivity which certainly limits their catalytic performance.[58-60] Several approaches have been adopted to address the issue of poor conductivity and improve the electrode/electrolyte interface (Figure 1.9).

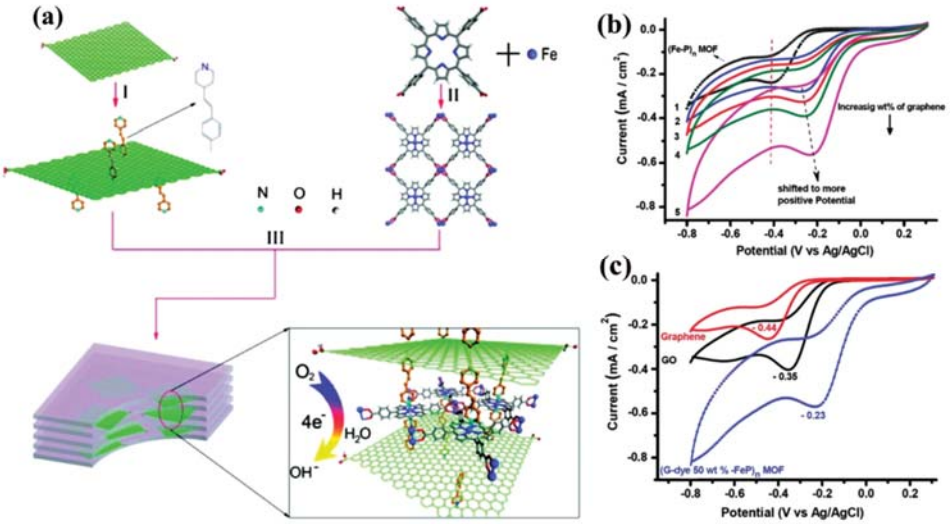

Figure 1.9 a) Schematic of the chemical structures of r-GO, G-dye, and (G-dye-FeP) n MOF, and magnifi ed view of layers. Inside the framework of (G-dye-FeP) n MOF showing how graphene sheets intercalated between prophyrin networks (Synthetic routes to make Graphene−Porphyrin MOF: (I) G-dye synthesized from r-GO sheets via diazotization with 4-(4-aminostyryl) pyridine, (II) (Fe−P)n MOF synthesized via reaction between TCPPs and Fe ions, (III) (G-dye-FeP) n MOF formed via reaction between (Fe−P) n MOF and G-dye). b) Cyclic voltammograms of oxygen reduction on the (1) (Fe−P) n MOF, (2) (G-dye 5 wt %-FeP)n MOF, (3) (G-dye 10 wt %-FeP)n MOF, (4) (G-dye 25 wt %-FeP)n MOF, (5) (G-dye 50 wt %-FeP)n MOF electrodes obtained in O 2 -saturated 0.1 M KOH at a scan rate of 50 mV/s. c) Cyclic voltammograms of oxygen reduction on (1) exfoliated graphene, (2) GO, (3) (G-dye 50 wt %-FeP) n MOF electrodes in 0.1 M KOH O_2 -saturated at a scan rate of 50 mV/s. Reproduced with permission Ref. 60 Copyright 2012, American Chemical Society.

Nowadays, non-precious metal catalyst (NPC) has aroused a lot of attention as metal free electrocatalysts due to strong activity, large abundance and longer durability. MOFs which have their high surface area, inherent porosity and ordered structure, have been widely used as precursors to derive nanoporous carbonaceous structures. Zn-based MOFs/ZIFs has been identified as an easy and direct way of fabricating NPC.[61] The conversion of organic ligands into carbon reduces Zn moieties which are eventually evaporated from the product at elevated temperature (≈900 °C). In addition, the presence of heteroatoms (N-, S-, P-, B- etc.) in the ligand backbone provide an ample opportunity for in situ addition of heteroatoms into the resulting NPC. In addition to deriving carbonaceous materials from pure MOFs, secondary sources for carbon and doped species have also been made to obtain highly active electrode materials. The use of secondary source has been suggested to improve the porosity and doping of heteroatoms in the final product. Peng et al., used ZIF-7 (Zn-benzimidazole) along with glucose as secondary carbon source. [62]

Moreover, the basic understanding of interactions of reactive and intermediate species with the catalyst surface is highly important, given the complex nature of pure MOFs and variety of MOF derived heterostructures. For example, in pure MOFs, the inherent structures could have different local environments in the vicinity of coordinated metal and the organic ligands. In addition, the porous carbon derived from MOFs may or may not have the hetero-atom dopants. The presence of dopants can provide various energy levels that can affect the ORR kinetics significantly. Hence, the role of metal

centers and doping atoms like nitrogen, boron, phosphorous and sulfur must be understood through theoretical calculations in addition to actual experimentation.[63]

1.5 Reference

1. Winter, M.; Brodd, R. J., Chem. Rev., 2004, 104 (10), 4245.

2. Dai, L.; Xue, Y.; Qu, L.; Choi. H.-J.; Baek, J.-B., Chem. Rev., 2015, 115 (11), 4823.

3. Ramaswamy, P.; Wong, N.E.; Shimizu, G.K.H.; Chem. Soc. Rev., 2014, 43, 5913.

4. Vesborg, P. C. K.; Jaramillo, T. F. RSC Adv. 2012, 2 (21), 7933.

5. Stonehart, P.; Ross, P. N., Jr. Electrochim. Acta 1976, 21 (6), 441.

6. Gloaguen, F.; Andolfatto, F.; Durand, R.; Ozil, P. J. Appl. Electrochem. 1994, 24 (9), 863.

7. Vielstich, W., Gasteiger, H. A., Lamm, A., Eds.; John Wiley & Sons: New York, 2003; Vol. 2, pp 316.

8. P. Strasser, S. Koh, T. Anniyev, J. Greeley, K. More, C. Yu, Z. Liu, S. Kaya, D. Nordlund and H. Ogasawara, Nat. Chem., 2010, 2, 454.

9. J. R. Kitchin, J. K. Norskov, M. A. Barteau and J. G. Chen, J. Chem. Phys., 2004, 120, 10240.

10. N. M. Markovic, R. R. Adzic, B. D. Cahan and E. B. Yeager, J. Electroanal. Chem., 1994, 377, 249.

11. C. T. Campbell, Annu. Rev. Phys. Chem., 1990, 41, 775.

12. J. A. Rodriguez, Surf. Sci. Rep., 1996, 24, 225.

13. V. R. Stamenkovic, B. Fowler, B. S. Mun, G. F. Wang and N. M. Markovic, Science, 2007, 315, 493.

14. J. Greeley, I. E. L. Stephens, A. S. Bondarenko, T. P. Johansson, H. A. Hansen, T. F. Jaramillo, J. Rossmeisl, I. Chorkendorff and J. K. Nørskov, Chem. Rev., 2009, 1, 552.

15. Y. Dai and S. Chen, J. Phys. Chem. C, 2011, 115, 2162.

16. C. Chen, P. Yang and V. Stamenkovic, Science, 2014, 343, 1339.

17. J. Zhang, K. Sasaki, E. Sutter and R. R. Adzic, Science, 2007,315.

18. A. C. Ferrandez, P. Buvat and C. Coutanceau, Chem. Mater.,2013, 25, 3797.

19. K. Miyabayashi and M. Miyake, Langmuir, 2014, 30, 2936.

20. J. Snyder, K. Livi and J. Erlebacher, Adv. Funct. Mater., 2013, 23, 5494.

21. Z. Z. Jiang and Z. Wang, Chem. Commun., 2010, 46, 6998.

22. S. Takenaka and H. Miyamoto, J. Phys. Chem. C, 2014, 118, 774.

23. S. Takenaka and H. Miyamoto, J. Phys. Chem. C, 2007, 111, 15133.

24. S. Chen, Z. Wei and L. Wan, J. Am. Chem. Soc., 2012, 134, 13252.

25. L. Li, Y. Xue, M. R. Xia, S. G. Chen and Z. D. Wei, Sci. Sin.:Chim., 2013, 43, 1566.

26. Y. Nie, S. Chen and Z. Wei, Chem. Commun., 2014, 50, 15431.

27. Z. B. Wang and G. P. Yin, J. Phys. Chem. C, 2010, 114, 672.

28. B. Fang, N. K. Chaudhari and J. S. Yu, J. Am. Chem. Soc., 2009, 131, 15330.

29. R. Jasinski, Nature, 1964, 201, 1212.

30. C. W. B. Bezerra, L. Zhang, K. Lee, H. Liu, A. L. B. Marques, E. P. Marques, H. Wang and J. Zhang, Electrochim. Acta, 2008, 53, 4937.

31. Y. Hu, W. Xing and Q. Li, Angew. Chem., Int. Ed., 2014, 53, 3675.

32. K. Wiesener, Electrochim. Acta, 1986, 31, 1073.

33. R. Franke, D. Ohms and K. Wiesener, J. Electroanal. Chem., 1989, 260, 63.

34. G. Liu, X. Li, P. Ganesan and B. N. Popov, Appl. Catal., B, 2009, 93, 156.

35. E. J. Biddinger and U. S. Ozkan, J. Phys. Chem. C, 2010, 114, 15306.

36. J. A. R. van Veen, H. A. Colijn and J. F. van Baar, Electrochim. Acta, 1988, 33, 801.

37. A. L. B. Wijnoltz, W. Visscher, J. A. R. van Veen, E. Boellaard, A. M. Van der Kraan and S. C. Tang, J. Phys. Chem. B, 2002, 106, 12993.

38. M. Bron, J. Radnik, M. Fieber-Erdmann and S. Fiechter, J. Electroanal. Chem., 2002, 535, 113.

39. H. Schulenburg, S. Stankov, V. Schunemann, J. Radnik, I. Dorbandt, S. Fiechter and H. Tributsch, J. Phys. Chem. B, 2003, 107, 9034.

40. H. W. Liang, X. Feng and K. Mu¨llen, J. Am. Chem. Soc., 2013, 135, 16002.

41. L. Yang, Y. Ma and Z. Hu, Angew. Chem., 2011, 123, 7270.

42. K. P. Gong and L. M. Dai, Science, 2009, 323, 760.

43. L. T. Qu and L. M. Dai, ACS Nano, 2010, 4, 1321.

44. S. S. Yu and L. M. Dai, J. Am. Chem. Soc., 2010, 132, 15127.

45. Z. H. Sheng and X. H. Xia, ACS Nano, 2011, 5, 4350.

46. R. L. Liu and K. Mu¨llen, Angew. Chem., Int. Ed., 2010,49, 2565.

47. C. Xiong and Z. Wei, J. Power Sources, 2012, 215, 216.

48. Z. Yang and S. Huang, ACS Nano, 2012, 6, 205.

49. D. Yang and J. Yu, J. Am. Chem. Soc., 2012, 134, 16127.

50. Z. Liu and F. Peng, Angew. Chem., Int. Ed., 2011, 50, 3257.

51. X. Sun, W. Xu and W. Xing, ACS Catal., 2013, 3, 1726.

52. D. Wei and G. Yu, Nano Lett., 2009, 9, 1752.

53. A. L. M. Reddy and P. M. Ajayan, ACS Nano, 2010, 4, 6337.

54. Z. Jin and J. M. Tour, ACS Nano, 2011, 5, 4112.

55. X. Wang and H. Dai, Science, 2009, 324, 768.

56. F. Gao and J. J. Spivey, J. Am. Chem. Soc., 2012, 135, 3315.

57. Y. Zheng and S. Z. Qiao, J. Am. Chem. Soc., 2011, 133, 20116.

58. K. F. Babu , M. A. Kulandainathan , I. Katsounaros , L. Rassaei , A. D. Burrows , P. R. Raithby , F. Marken , Electrochem. Commun. 2010 , 12 , 632.

59. J. Mao , L. Yang , P. Yu , X. Wei , L. Mao , Electrochem. Commun. 2012 , 19 , 29.

60. M. Jahan , Q. Bao , K. P. Loh , J. Am. Chem. Soc. 2012 , 134 , 6707.

61. A. Aijaz , N. Fujiwara , Q. Xu , J. Am. Chem. Soc. 2014 , 136 , 6790.

62. Z. Peng , S. Fang , X. Zhonghua , S. Zhigang , J. Yun , C. Dapeng , Energy. Environ. Sci. 2014 , 7 , 442.

63. S. Kattel , P. Atanassov , B. Kiefer , J. Mater. Chem. A. 2014 , 2 , 10273.

CHAPTER TWO: EFFICIENT OXYGEN ELETRORUDCITON: HIERARCHICAL POROUS FE-N-DOPED HOLLOW CARBON NANOSHELLS

2.1 Introduction

The oxygen reduction reaction occurring at the cathode of proton exchange membrane fuel cells (PEMFCs) and metal-air batteries is a bottleneck reaction for the commercialization of these energy techniques. Currently, platinum and platinum-based alloys are the most efficient catalysts for the oxygen reduction reaction (ORR).[1] However, the high cost, scarcity, low tolerance to methanol fuel, and poor stability of Pt-based materials hinder the widespread utilization of these noble metal cathode catalysts. There are currently extensive efforts devoted to the development of non-precious metal catalysts (NPMCs). Among the various catalysts, transition metal−nitrogen-carbon (Me−N−C) containing materials, especially Fe−N−C, have been demonstrated as a family of promising NMPCs for oxygen reduction reaction (ORR) due to their high ORR activity in both alkaline and acidic electrolytes.[2,3] However, the ORR activities of the present Fe-N-C materials are still less than that of Pt/C, especially in acidic conditions. The development of non-precious metal catalyst with highly active ORR activity remains a challenge.

To construct highly active Fe-N_x sites for ORR, in addition to introducing iron-containing active sites, the selection of other reaction precursors also plays a pivotal role in ORR activity and durability. Generally, three different nitrogen bonding environments exist in

Fe-N-C catalysts: C≡N based non-aromatic bonds; C-N based non-aromatic bonds and N-containing aromatic bonds.[4] These can be obtained with different precursors. It is noticed that catalysts derived from aromatic precursors, such as polyaniline (PANI), exhibit a better combination of activity and durability than that of catalysts derived from non-aromatic precursors.[4] This is because heat treatments of aromatic precursors like aniline are believed to facilitate the incorporation of nitrogen containing active sites into the graphitized carbon matrix in the presence of iron and/or cobalt.[4,5] However, the nitrogen atoms in PANI are outside of the aromatic ring and thus have a great tendency of loss during high temperature heat treatments. It would be beneficial to have precursors with N-containing aromatic rings. Such a compound, 2, 2'-bipyridine, has been reported to have good ORR properties.[6,7] Unlike 2, 2'-bipyridine, 4, 4'-bipyridine can form coordination compounds with extended structure through Fe and N bonding. Not investigated in the ORR field yet, it could have advantages of preventing the agglomeration during the heat treatment process and facilitating uniform distribution of active sites on the catalyst surface.[8]

In order to maximize the number of active sites, different templates, Ni foam, SBA 15, melamine foam, silica colloid, metal organic frameworks (MOFs) have been developed to prepare porous metal-containing nitrogen-doped carbon materials.[9-12] Among the various porous materials, hierarchical porous materials tend to provide more active sites and facilitate the transport and adsorption of oxygen.[6] Among numerous carbon-based electrode materials, hollow carbonaceous spheres have attracted attention due to the high surface-to-volume ratios and more accessible active sites on the shell.[13] The nanoshells

act as release pathways and nanoreactors for encapsulated substances and outside species.[13] Nitrogen-doped hollow carbon spheres were investigated in the past few years and showed promising ORR properties.[13-18] However, hierarchical porous materials of small monodispersed sizes (< 50 nm) with Fe-N-C hollow shells are rarely reported.

Here, we demonstrate a new design for the synthesis of Fe-N-doped hierarchical porous carbon hollow nanoshells employing core-shell CdS@mSiO_2 as templates. Cheap and abundant 4, 4'-bipyridine and $FeCl_3$•$6H_2O$ are chosen as carbon, nitrogen and iron sources. The prepared hollow porous Fe-N-C catalysts possess uniform particle sizes less than 50 nm. The Fe-Nx active sites in the synthesized materials are homogeneously distributed on the surface, which has a Brunauer–Emmett–Teller (BET) surface area up to 1189 m^2/g with both microporosity and mesoporosity. These structural features together with an experimentally optimized graphitization process endow the materials with enhanced mass transfer efficiencies, large accessible pore volume, and good electrical conductivity. These characteristics are desirable for efficient electrocatalytic activity.

2.2 Experimental Section

2.2.1 Synthesis of CdS nanoparticles:[19] 3 mmol sulfur powder, 3 mmol $Cd(CH_2COO)_2 \cdot 2H_2O$, and 120 ml oleic acid (OA) were added to a 250 ml three-neck flask. The reaction mixture was heated to 285 °C for 4 h under argon flow. After cooling to room temperature, excess methanol was added with subsequent centrifugation and washing with ethanol for three times.

2.2.2 Synthesis of CdS@mSiO2 core-shell nanoparticles:20 The CdS@mSiO$_2$ core-shell nanoparticles were prepared through a versatile sol–gel method. 18 mg CdS nanoparticles with oleic acid capping agent were dispersed in 3 ml chloroform. Then 300 ml 0.55 M aqueous ethyltrimethylammonium bromide (CTAB) solution was poured to the above solution and stirred vigorously for 30 min. The resulting oil-in-water microemulsion was then heated up to 60 °C and aged at that temperature for 10 min to evaporate chloroform under argon flow. Then 1.8 ml of 2 M NaOH solution was added to the mixture and heated to 70 °C in argon flow. After that, 18 ml ethylacetate and 3 ml TEOS was added to the reaction solution in sequence and stirred for 3 hours. After cooling, the resultant product was separated followed by washing with ethanol for 3 times. Finally, the purified samples were re-dispersed in 300 ml acetone and refluxed at 80 °C for 48 h to remove the CTAB template.

2.2.3 Synthesis of carbon nanoshell: The carbon nanoshell was prepared through a nanocasting procedure. Typically, 10ml water was added to a 15 ml ethanol solution containing 346 mg $FeCl_3 \cdot 6H_2O$ and 200 mg 4, 4'-bipyridine with a molar ratio of $FeCl_3 \cdot 6H_2O$ to 4, 4'-bipyridine was 1:1. After the solution became clear, 250 mg CdS@mSiO$_2$ core-shell nanoparticles were poured into the above solution and stirring vigorously overnight to evaporate the solvent at room temperature. Then the material was pyrolyzed at 900 °C in argon atmosphere for 3 hours with a heating speed of 3 °/min. Finally, the materials were etched with 5 wt% HF to remove CdS@mSiO$_2$ template. The carbon sheet was prepared by the same procedure but with no addition of CdS@mSiO$_2$ core-shell templates.

2.2.4 Electrocatalytic activity measurements: Electrochemical characterization of the catalysts was performed in a conventional three-electrode cell using CHI760D electrochemical workstation (CH Instruments, USA) controlled at room temperature and under atmospheric pressure. Ag/AgCl and platinum wire were used as reference and counter electrodes, respectively. All potentials in this report were converted into reversible hydrogen electrode (RHE).

A ring-disk electrode (RDE) with a glassy carbon disk and a Pt ring was served as the substrate for the working electrode. The catalyst ink was prepared by mixing the catalyst powder (10 mg) with 80 μL Nafion solution (5wt %) and 1.2 ml ethanol in an ultrasonic bath. Then 2.5 μL of catalyst ink was pipetted onto the GC electrode with a catalyst loading of 0.1 mg cm^{-2} in 0.1 M KOH. In 0.1M HClO4 solutions, 15 μL of catalyst ink was deposited onto the GC electrode corresponding a catalyst loading of 0.6 mg cm^{-2}. As a comparison, commercial 20 wt. % platinum on Vulcan carbon black (Pt/C from Alfa Aesar) was prepared by blending Pt/C (10 mg) with 80 μL Nafion solution (5wt %) and 1.2 ml ethanol in an ultrasonic bath. A Pt loading about 20 μg cm^{-2} was applied in both alkali and acid conditions.

Linear sweep voltammetry (LSV) polarization curves for the oxygen reduction reaction (ORR) were measured in an oxygen saturated 0.1 M KOH and 0.1 M HClO4 electrolyte with a sweep rate of 10 mV s^{-1} at various rotating speeds from 400 to 2500 rpm. The cyclic voltammogram (CV) were recorded in solutions saturated with either Ar or O_2 gas without rotation with same sweep rate as that of LSV curve. The electron transfer number

(n) and kinetic current density (j_K) were analyzed on the basis of Koutecky– Levich equations shown in below:

$$1/j=1/j_L+1/j_K$$

$$j_L=0.62nFCD^{2/3}\upsilon^{-1/6}w^{-1/2}=Bw^{-1/2}$$

$$1/j=1/Bw^{-1/2}+1/j_K$$

where $B=0.62nFC_0\ D_0^{\ 2/3}\ \upsilon^{-1/6}$, j was the measured current density, j_K and j_L were the kinetic- and diffusion-limiting current densities, *w* was the rotation speed, *n* was the electron transfer number, *F* was the Faraday constant (F = 96485 C mol^{-1}), C was the bulk concentration of O_2, D was the diffusion coefficient of dissolved oxygen, v was the kinematic viscosity of the electrolyte.

2.2.5 Characterization: The crystal structures of the materials were characterized by X-ray diffractometer (XRD) (D/Max2000, Rigaku) using a Bruker D8-Advance powder diffractometer operating at 40 kV, 40 mA for Cu Kα radiation (λ=1.5406 Å). The morphology and composition of the samples were analyzed with a Tecnai T12 transmission electron microscope (TEM) and a Philips FEI XL30 field emission scanning electron microscope (FESEM) equipped with a LaB6 electron gun, and an EDAX energy-dispersive spectrometer (EDS). The surface properties and composition of the materials were studied by X-ray photoelectron spectroscopy (XPS) characterization using a Kratos AXIS ULTRADLD XPS system equipped with an Al K monochromated X-ray source and a 165 mm electron energy hemispherical analyzer. The shifts in energy

(charging) of the XPS spectra were calibrated using the C1s peak at 284.6 eV as a reference peak. Nitrogen sorption analysis was conducted at 77 K using a Micromeritics ASAP 2020 surface-area and pore-size analyzer. The specific surface areas were calculated using the Brunauer–Emmett–Teller (BET) equation from the nitrogen adsorption data in the relative range (P/P_0) of 0.04-0.20. The pore size distribution (PSD) plot was recorded from the adsorption and desorption branch of the isotherm based on the Barrett–Joyner–Halenda (BJH) and Horvath-Kawazoe (H-K) model. The elemental analysis was performed by the Atlantic Microlab in Georgia.

2.3 Results and Discussion

2.3.1 Catalyst Preparation and Characterization

The fabrication process of the carbon-nanoshells is depicted in scheme 2.1. First CdS nanoparticles with a size around 25 nm are synthesized and serve as seeds for the synthesis of CdS@mSiO_2 core-shell nanoparticles.[20] The thickness of mesoporous silica shell can be tuned by the amount of silica precursors used and gelation temperatures. The precursors 4, 4'-bipyridine and $FeCl_3$•$6H_2O$ are first dissolved in water-ethanol solution and then the solution is mixed with CdS@mSiO_2 core-shell nanoparticles. The precursors are introduced into the mesoporous silica shell during the water and ethanol evaporation process. The obtained solid composites are then calcinated at 900 °C and subsequently treated with HF to remove the template. All atoms on the aromatic ring structures of 4, 4'-bipyridine possess sp2 hybridization which promotes the doping of nitrogen atoms in the graphitized carbon matrix at high temperature.[4] In addition, the surface pyridinic

nitrogen coordinated with iron can lead to catalytically favorable active sites for ORR.[21,22]

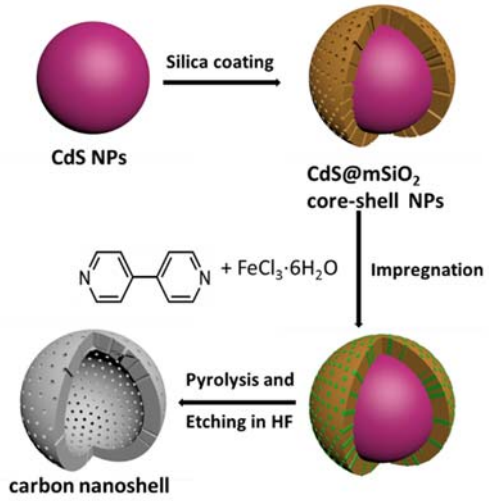

Scheme 2.1 Schematic illustration of the synthetic process of hierarchical hollow carbon-nanoshells.

Powder X-ray diffraction (XRD) patterns (Figure 2.1) indicate that the synthesized carbon-nanoshells are graphitic carbon with the (002) and (100) planes appearing at diffraction peaks of 26.1 and 43.2.[23] Figure 2.2a shows the typical transmission electron microscopy (TEM) images of the prepared CdS nanoparticles and Figure 2.2b shows the corresponding CdS@mSiO2 core-shell nanoparticles with 10 to 15 nm mesoporous silica shells (the porosity feature and surface area of CdS@mSiO2 core-shell template are shown in Figure 2.3 and Table 2.1). After pyrolysis at 900 °C and the etching off the hard templates, monodisperse mesoporous carbon-nanoshells with a thickness about 10 nm

(Figure 2.2e) are successfully obtained. The diameters of such nanoshells are less than 50 nm (Figure 2.2c-e) and these are consistent with the sizes of the core-shell templates. Monodisperse carbon-nanoshells with a particle size less than 100 nm are scarcely reported.[4,24,25]

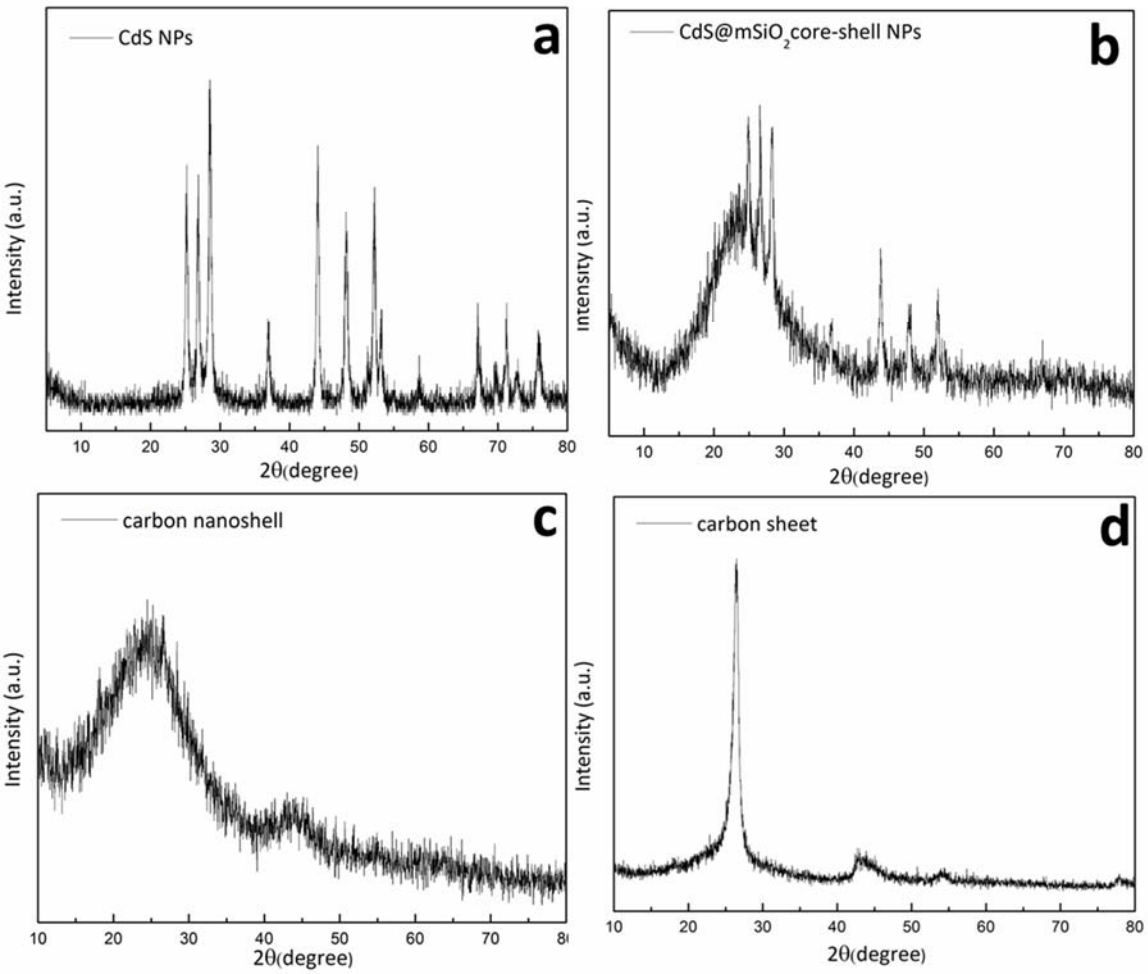

Figure 2.1 XRD patterns of CdS nanoparticle (a), CdS@mSiO$_2$ core-shell nanoparticles (b), carbon nanoshells (c) and carbon sheets (d) pyrolyzed at 900 °C and HF etching.

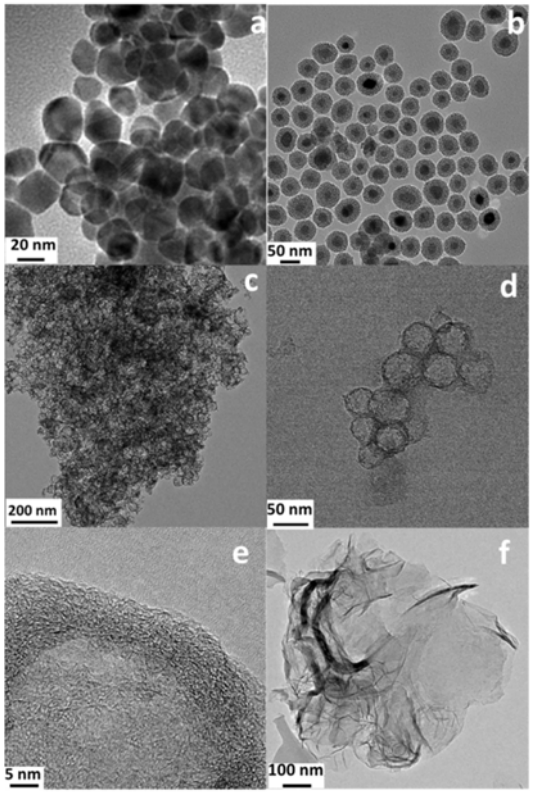

Figure 2.2 TEM and HRTEM images of a), CdS nanoparticles, b) CdS@mSiO$_2$ core-shell nanoparticles, c-e) carbon-nanoshell after pyrolyzed at 900 °C and HF etching, f) carbon sheet pyrolyzed at 900 °C and HF etched.

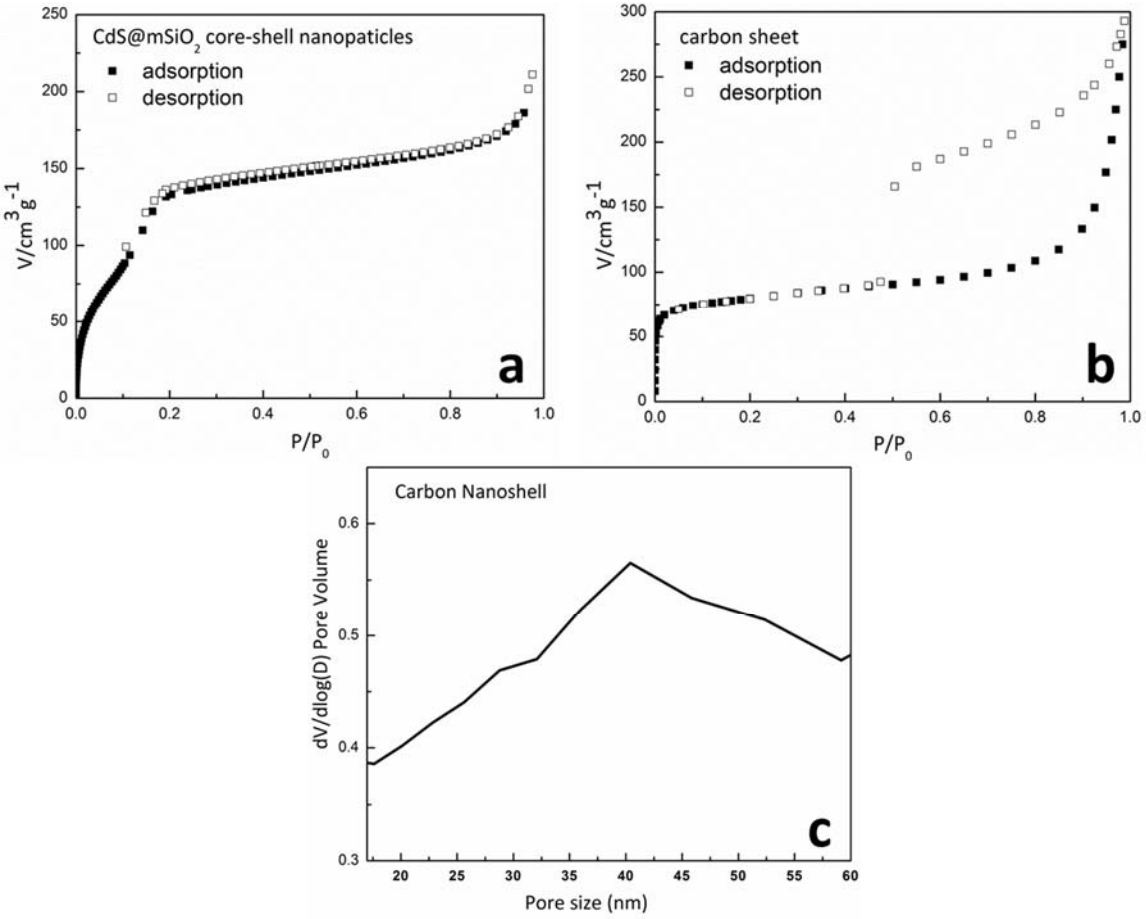

Figure 2.3 Nitrogen adsorption/desorption isotherms of a) CdS@mSiO2 core-shell nanoparticles, b) carbon sheets, pyrolyzed at 900 °C and HF etching. c) Pore size distribution curve for carbon nanoshells pyrolyzed at 900 °C and HF etching.

Table 2.1 Elemental compositions of carbon nanoshells and carbon sheets pyrolyzed at 900 °C and HF etching determined by elemental analysis.

Samples	C wt %	H wt %	N wt %
Carbon nanoshell	82.20	1.78	4.11
Carbon nanosheet	91.83	1.19	1.02

The synthesized carbon-nanoshells show a BET surface area of 1189 m^2/g. The hysteresis loop in Figure 2.4 indicates the microporous and mesoporous nature of the materials. The pore size distribution of the carbon-nanoshells is centred around 0.5 nm in micropore range and around 3.0 nm and 40 nm in mesopore range (Figure 2.3) according to the Barrett−Joyer−Halenda (BJH) and Horvath-Kawazoe (H-K) model (Figure 2.4). The hollow, hierarchical porosity and small size carbon-nanoshells all contribute to a large surface area which could help the transportation and adsorption of the reactant O_2. The carbon-nanoshells also exhibit high CO_2 uptakes of 105 and 70 cm^3/g at 273 and 298 K, respectively (Figure 2.5). The high CO_2 uptake values of carbon-nanoshells are among the highest level of reported N-decorated carbons and larger than those of well-known zeolitic imidazolate frameworks and MIL-53 (Al) under the same conditions.[10,26-28] This high CO_2 uptake could be partially attributed to the N-doping in the carbon-nanoshells that can act as basic centres for attracting acidic CO_2 molecules.[10]

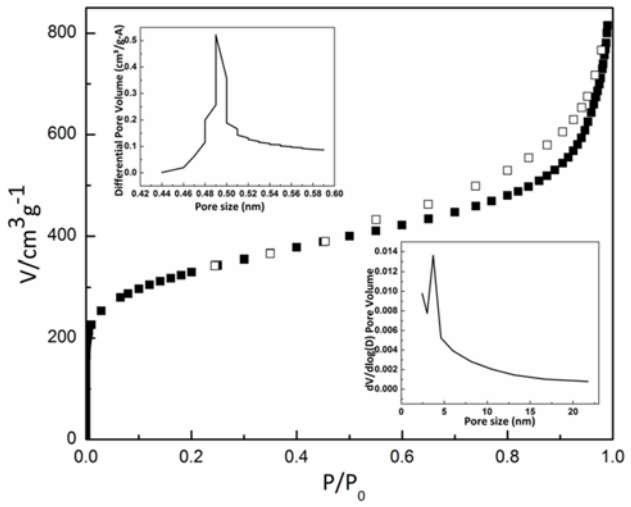

Figure 2.4 Nitrogen adsorption/desorption isotherms and the corresponding pore size distribution curves for carbon-nanoshells pyrolyzed at 900 °C and HF etched.

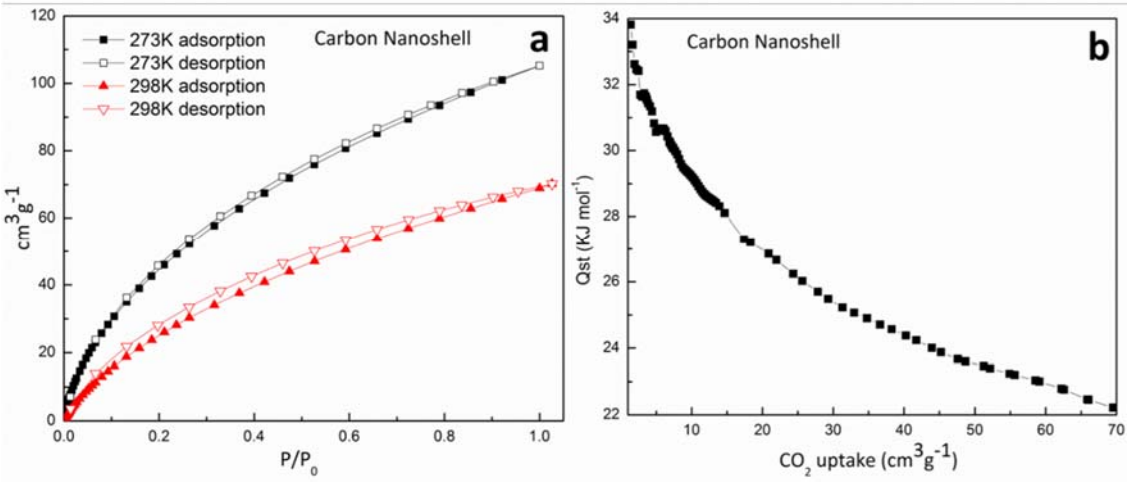

Figure 2.5 CO_2 uptakes at 273K and 298K a), Isosteric heats of adsorption b) of the carbon nanoshells pyrolyzed at 900 °C and HF etching.

Energy dispersive X-ray (EDX) analysis on carbon-nanoshell confirms the presence of carbon, nitrogen and iron (Figure 2.6). It is considered that metal species stabilized by nitrogen coordination can be durable and positive for oxygen reduction reaction activity although the exact mechanism remains unknown.[8,11,29,30] No metal-containing nanoparticles are observed in TEM and EDX data. By XRD, no crystalline metals or metal oxides can be observed.

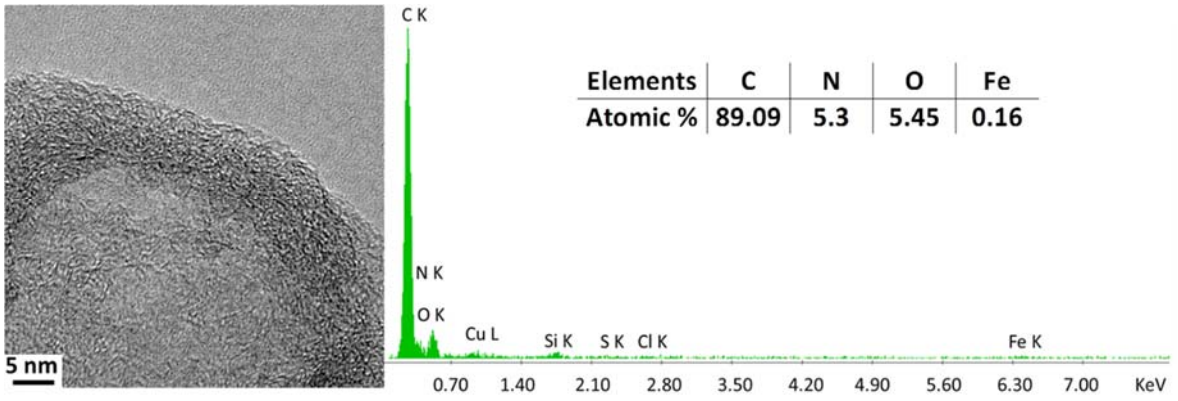

Figure 2.6 EDX spectrum of the synthesized carbon nanoshells pyrolyzed at 900 °C and HF etching and the corresponding analysis of elemental composition. (The copper peaks originated from the TEM grid holding the sample.)

The surface Fe, N contents are also confirmed by XPS. The survey scan in Figure 2.7 reveals the successful introduction of nitrogen and iron atoms into carbon-nanoshells after pyrolysis. The contents of nitrogen and iron in the carbon-nanoshells are estimated to be 3.71 at% N and 0.34 at% Fe (Table 2.2). The high resolution N1s spectra of carbon-nanoshells demonstrate the presence of pyridinic, metal-coordinated and graphitic N fitting three different binding energies of 398.3, 399.6 and 401.2 eV, respectively (Figure 2.8).[31] It is believed that Fe-Nx, pyridinic N, and graphitic N could all make positive contributions to the ORR activity and durability.[11,32,33] Figure 2.8 shows the high-resolution Fe 2p spectra. The peaks at 709.2 and 711.9 eV can be assigned to Fe^{2+} and Fe^{3+} species 2p3/2 orbitals binding energies. For the 2p1/2 band, the peak at 721.2 eV is attributed to the binding energy of Fe^{2+} and 723.3 eV for Fe^{3+}. The binding energies of

the Fe2p (around 711 eV) could be ascribed to the N-coordinated Fe^{3+} or Fe^{2+}.[33,34] In addition, both the EDX and XPS results show that after pyrolysis and etching with HF, the carbon-nanoshells show no Cadmium left.

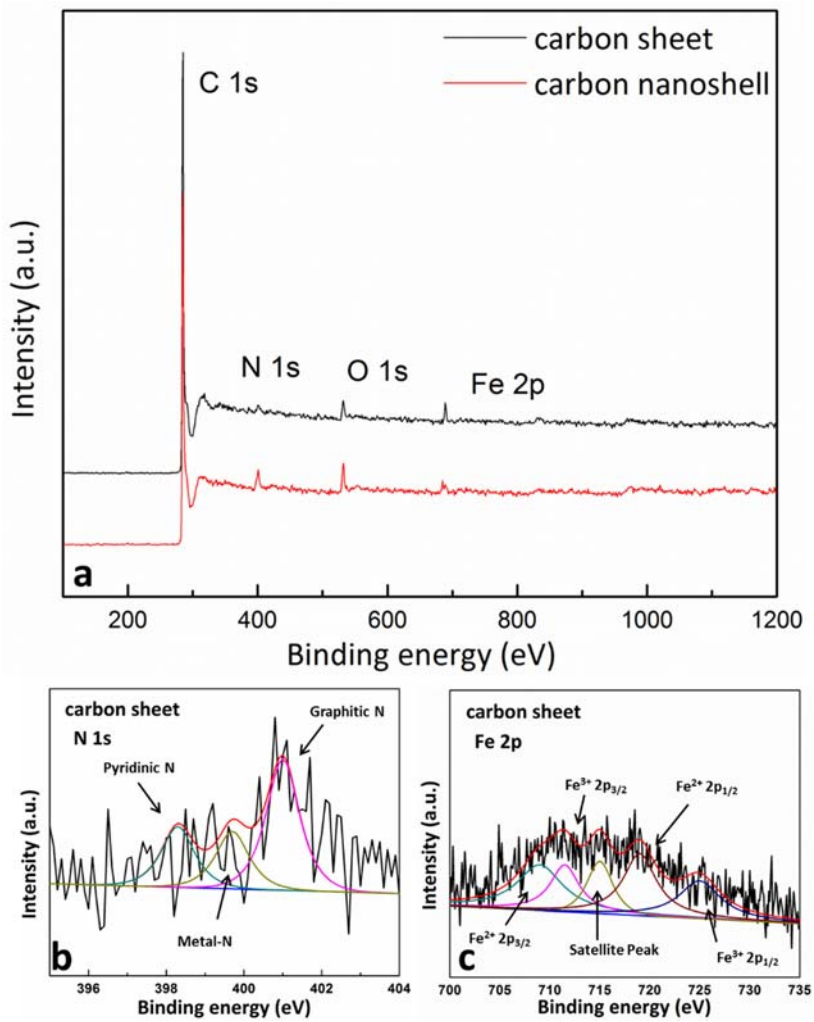

Figure 2.7 XPS survey scan of carbon nanoshells and carbon sheets (a), high-resolution Fe 2p and N 1s XPS spectra of carbon sheet (b,c) pyrolyzed at 900 °C and HF etching.

Table 2.2 Elemental compositions of carbon nanoshells and carbon sheets pyrolyzed at 900 °C and HF etching determined by XPS.

Samples	N atom %	Fe atom %	Graphitic nitrogen atom %	Metal nitrogen atom %	Pyridinic nitrogen atom %
Carbon nanoshell	3.71	0.34	51.83	32.11	16.06
Carbon sheet	1.22	0.13	33.33	33.33	33.33

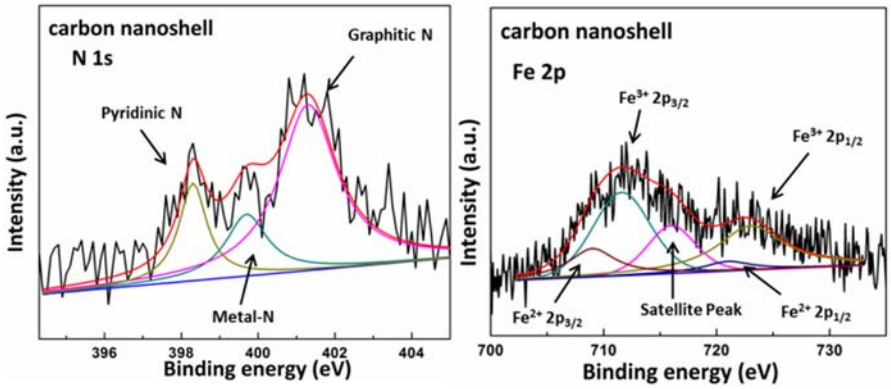

Figure 2.8 High-resolution N 1s and Fe 2p XPS spectra of carbon-nanoshell pyrolyzed at 900 °C and HF etched.

For comparison, 4, 4'-bipyridine and $FeCl_3 \cdot 6H_2O$ without $CdS@mSiO_2$ core-shell templates are also prepared under similar conditions. After impregnation, pyrolysis and etching with HF, these materials show randomly distributed large carbon sheets in TEM (Figure 2.2f) (called carbon sheets in the following). The carbon sheets show much lower BET surface area (262 m^2/g) (Figure 2.3, Table 2.3). Powder X-ray diffraction (XRD) patterns (Figure 2.1) indicate that the synthesized carbon sheets are graphitic carbon with the (002) and (100) planes but with a higher crystallinity; sharp diffraction peaks appear at 26.1 and 43.2 in XRD. However the higher crystallinity in carbon sheets results in lower nitrogen content as can be seen in the XPS surface content analysis and elemental analysis (Table 2.1, 2.2). The pyrolysis of 4, 4'-bipyridine and $FeCl_3 \cdot 6H_2O$ without template could lead to the easy **loss** of nitrogen and iron species.

Table 2.3 Textural properties of carbon nanoshells and carbon sheets pyrolyzed at 900 °C and HF etching determined by nitrogen adsorption-desorption isotherms.

Samples	BET surface area (m^2/g)	Micropore surface area (m^2/g)	Mesopore surface area (m^2/g)	Macropore size distribution (nm)	Mesopore size distribution (nm)	Micropore size distribution (nm)
$CdS@mSiO_2$ core-shell template	457	398	59		2	
Carbon nanoshell	1189	462	727	40	3.0	0.5
Carbon sheet	262	161	101	60	2.5	1.0

2.3.2 Catalytic Activity Evaluation

The ORR activity and kinetics of the obtained catalysts is evaluated using ring-disk electrode (RDE) technique at a catalyst loading of 0.1 mg cm^{-2} in 0.1 M KOH and 0.6 mg cm^{-2} in 0.1 M $HClO_4$ at room temperature. The effect of $FeCl_3$•$6H_2O$ and 4, 4'-bipyridine ratios on the catalyst activity for ORR is also studied. We find that a ratio of 1:1 is optimal (Figure 2.9a, b) as revealed by the onset and half-wave potentials in the ORR polarization plots. Therefore, this ratio is used in this project. Calcination temperature also plays an important role in the ORR activity of the produced materials.[33] The best ORR activity of the hollow carbon-nanoshells is achieved at 900 °C (Figure 2.9c, d). Therefore, the catalysts discussed below are all produced at 900 °C.

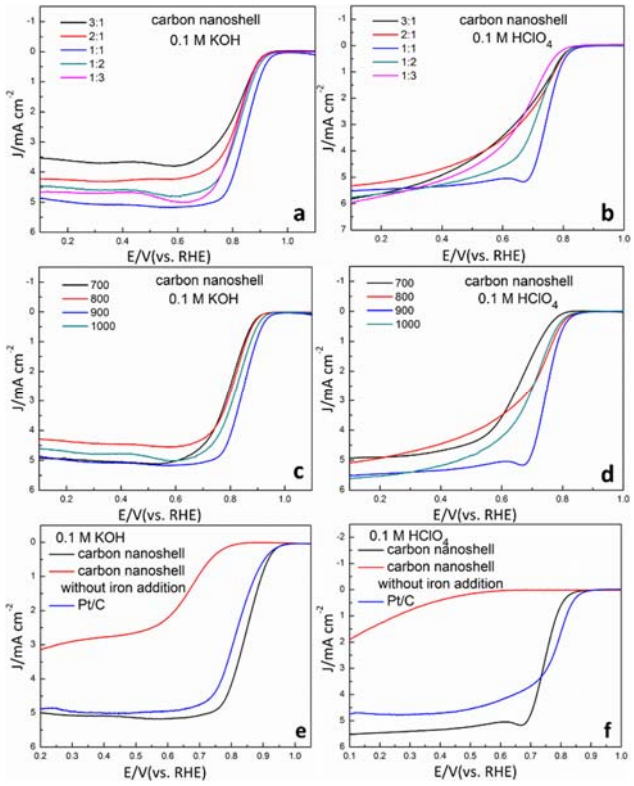

Figure 2.9 RDE voltammograms of carbon nanoshells catalysts pyrolyzed by heating the mixtures containing different molar ratio of $FeCl_3 \cdot 6H_2O$ and 4, 4'-bipyridine at 900 °C and HF etching in O_2-saturated 0.1 M KOH (a) and 0.1 M $HClO_4$ (b). RDE voltammograms of carbon nanoshells pyrolyzed at different temperatures in O_2-saturated 0.1 M KOH (c) and 0.1 M $HClO_4$ (d). RDE voltammograms of carbon nanoshells, carbon nanoshells without iron addition pyrolyzed at 900 °C and HF etching, and Pt/C in O_2-saturated 0.1 M KOH (e) and in O_2-saturated 0.1 M $HClO_4$ (f). For all tests, the catalyst loading is 0.1 mg cm^{-2} and the scan rate is 10 mV s^{-1} in O_2-saturated 0.1 M KOH. The catalyst loading is 0.6 mg cm^{-2} and the scan rate is 10 mV s^{-1} in O_2-saturated 0.1 M $HClO_4$.

The steady-state ORR polarization curves in 0.1 M KOH indicate that the carbon-nanoshells exhibit an ORR onset potential of 0.98 V vs. reversible hydrogen electrode (RHE) determined from a RDE polarization curves at a rotation rate of 1600 rpm (Figure 2.10a). This is similar to that of Pt/C catalyst (20 μg/cm^2 Pt) at the same catalyst loading (0.1 mg cm^{-2}). The half-wave potential obtained on the carbon-nanoshell is 0.85 V at 1600 rpm (Figure 2.10a). Additionally, the carbon-nanoshell shows a higher limiting current density of 5.1 mA cm^{-2} at 0.3 V in alkaline condition, which is larger than that of Pt/C. Figure 2.10g shows the cyclic voltammograms (CVs) of the carbon-nanoshell in Ar and O_2 saturated 0.1 M KOH. Though the CVs for the nanoshell show nearly rectangular shapes in Ar and a well-defined reduction peak at 0.86 V in the O_2 saturated solution which are comparable to that of Pt/C, nanoshells are distinguished by a high peak current of 1.1 mA cm^{-2}.

The electrochemical catalytic activities of carbon-nanoshell for ORR in acidic media (0.1 M $HClO_4$) are also studied at a catalyst loading of 0.6 mg cm^{-2}. The polarization curves in 0.1 M $HClO_4$ are displayed in Figure 2.10b, with the onset potential and the half-wave potential only 30 mV and 20 mV more negative than those of Pt/C. The decrease of the current density at the potential about 0.7 V in acidic condition may be attributed to the full integration between catalyst and oxygen causing the rapid depletion of the latter. Additionally, the carbon-nanoshell shows a limiting current density of 5.4 mA cm^{-2} at 0.3V acidic conditions, higher than that of Pt/C. In the acidic cyclic voltammograms (CVs) curves, the reduction peak potential of carbon-nanoshell is 0.72 V, only 88 mV smaller than that of Pt/C and with a higher peak current of 2.4 mA cm^{-2}, highlighting the

pronounced electrocatalytic activity of carbon-nanoshells for oxygen reduction in acidic conditions (Figure 2.10h).

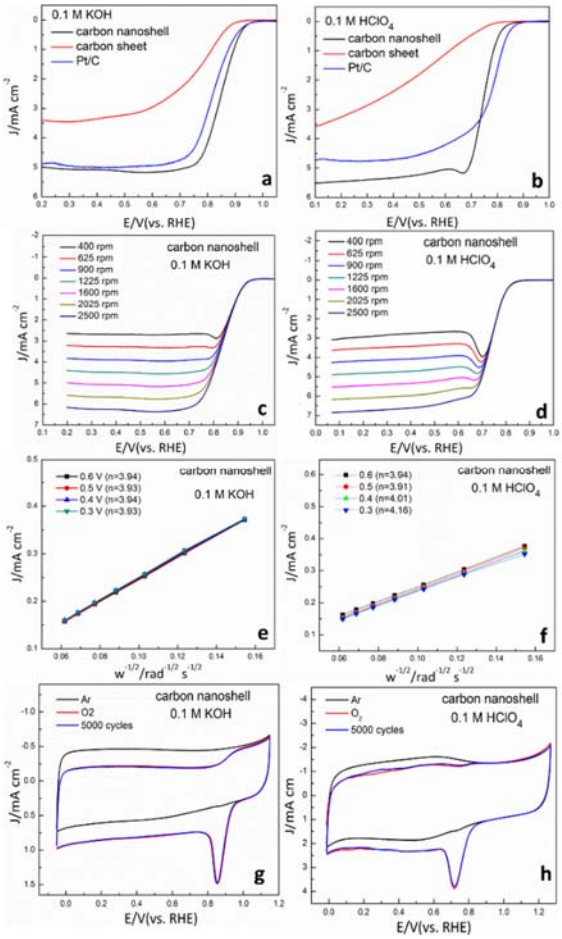

Figure 2.10 RDE voltammograms of carbon-nanoshells, carbon sheet pyrolyzed at 900 °C, HF etched and Pt/C in O_2-saturated 0.1 M KOH (a) and in O_2-saturated 0.1 M $HClO_4$ (b).RDE voltammograms at different rotation rates and Koutecky-Levich plots of carbon-nanoshell in O_2-saturated 0.1 M KOH (c,e) and in O_2-saturated 0.1 M $HClO_4$ (d,f). Cyclic voltammograms of carbon nanoshells pyrolyzed at 900 °C and HF etching in O_2-saturated 0.1 M KOH (g) and 0.1 M $HClO_4$ (h). For all tests, the catalyst loading is 0.1 mg cm^{-2} and the scan rate is 10 mV s^{-1} in O_2-saturated 0.1 M KOH. The catalyst loading is 0.6 mg cm^{-2} and the scan rate is 10 mV s^{-1} in O_2-saturated 0.1 M $HClO_4$.

To the best of our knowledge, the values of onset and half wave potentials of the carbon-nanoshells in both alkaline and acid conditions are among the best in NPMCs reported to date.[8,35,36] It is worth noting that the onset and half wave potential for the carbon sheets significantly shifted to a more negative potential and lower limiting current density (Figure 2.10a, b) in both alkaline and acid conditions. This sharp contrast implies the hierarchically porous hollow carbon shell design provides larger surface area and consequently more active sites, facilitating oxygen and electrons transport and diffusion.

In addition, to investigate how the iron affects the electrochemical properties of carbon-nanoshells, a controlled experiment is conducted under the same conditions to produce carbon-nanoshells but without $FeCl_3 \bullet 6H_2O$ in the preparation. As a result, the polarization curves, the onset and half wave potentials of the obtained material shift negatively in comparison with the prepared carbon-nanoshells with iron (Figure 2.9e, f). The result indicates that the Fe-Nx active sites indeed contributed to the electroactivity in the obtained carbon-nanoshells, though more systematic study is needed to verify the mechanism of active sites in the carbon-nanoshells materials.[8,37]

The selectivity of oxygen for the synthesized carbon-nanoshells is depicted in linear Koutecky–Levich (K-L) plots obtained from the polarization curves at various rotating speeds (Figure 2.10e, f). The Linear Sweep Voltammetry (LSVs) of carbon-nanoshells measured with an RDE at various rotating speeds (Figure 2.10c, d) shows an increasing cathodic current with increasing rotating speed because of the improved mass transport at the electrode surface. The electron transfer number is calculated from the slope of the K-

L plots to be about 4 at 0.30–0.60 V in alkali and acidic conditions, suggesting that the four-electron reduction pathway to produce water as the main product is favoured, a promising characteristic for fuel cell application.

In addition, the material also shows good stability. The carbon-nanoshells show a stable current-time (i–t) chronoamperometric response after the introduction of 3.0 M methanol in both alkaline and acidic conditions (Figure 2.11a, b). No noticeable changes are observed in the peak current or capacitive current for the carbon-nanoshells in the corresponding cyclic voltammograms for 5000 cycles in 0.1 M KOH and 0.1 $HClO_4$ solutions (Figure 2.10g, h). Moreover, the carbon-nanoshells are also subjected to a chronoamperometric durability test around 50,000 s at ~0.55V (vs. RHE) in alkaline and acidic condition. As shown in Figure 2.11c, d carbon nanoshells exhibit a slow attenuation with ~93% and 95% of the relative current persisted in alkaline and acidic conditions respectively.

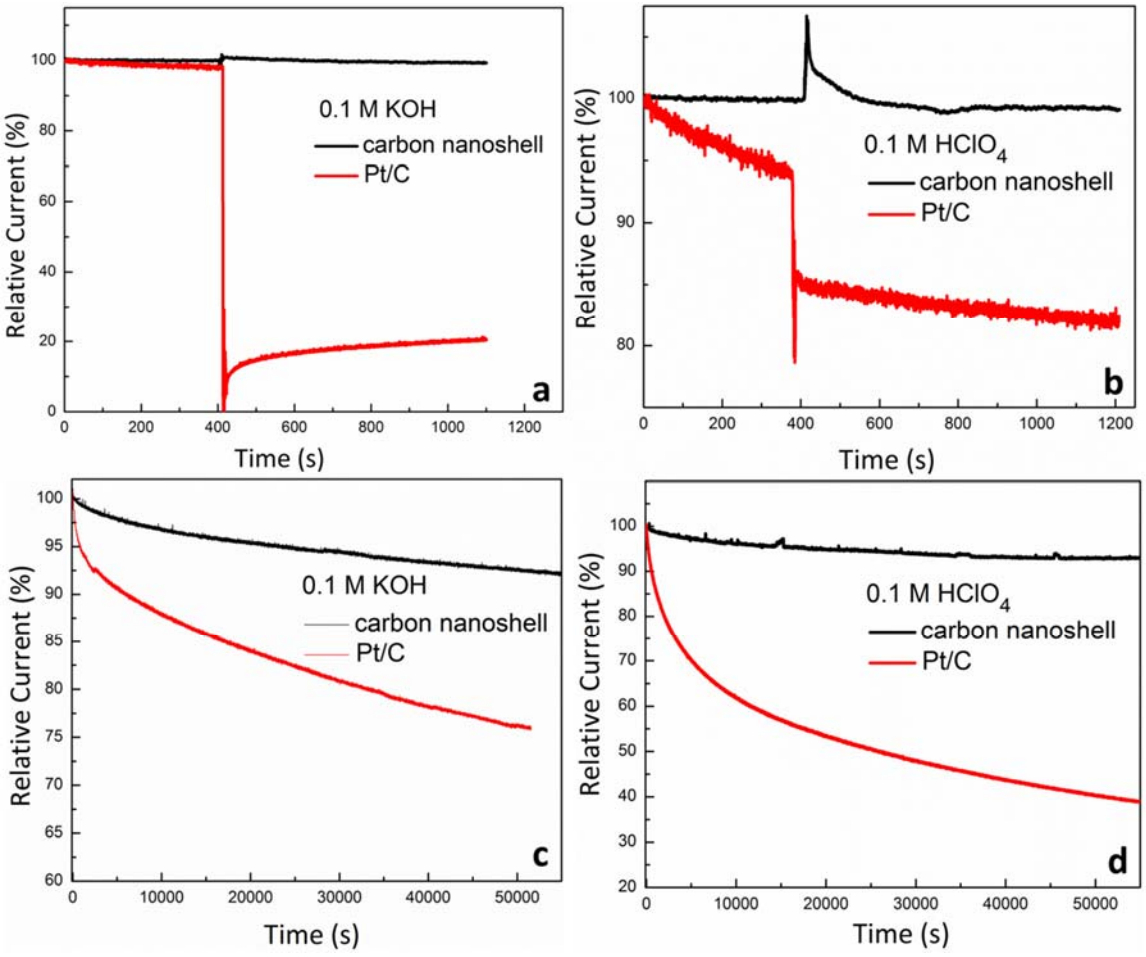

Figure 2.11 The chronoamperometric responses (i–t) of carbon naonoshells pyrolyzed at 900 °C and HF etching and Pt/C at 0.55 V vs. RHE in O_2-saturated 0.1 M KOH (a) and at 0.55 V vs. RHE in 0.1 M $HClO_4$ (b). Methanol crossover tests by introducing 3 M methanol into the electrolyte at 400 s. For all tests, the catalyst loading is 0.1 mg cm^{-2} and the scan rate is 10 mV s^{-1} in O_2-saturated 0.1 M KOH. The catalyst loading is 0.6 mg cm^{-2} and the scan rate is 10 mV s^{-1} in O_2-saturated 0.1 M $HClO_4$.

2.4 CONCLUSIONS

In summary, we report a monodisperse hollow carbon-nanoshells material with highly efficient ORR performance by employing CdS@mSiO_2 core-shell nanoparticles as templates and $FeCl_3$•$6H_2O$ and 4, 4'-bipyridine as iron and nitrogen precursors. In respect to the commercial Pt/C catalysts, carbon-nanoshell materials demonstrate excellent ORR activity, high selectivity (direct $4e^-$ reduction of oxygen to water), superior electrochemical stability and methanol tolerance in both alkaline and acidic conditions. The use of such coordination material may have led to a more uniform distribution of Fe-N_x active sites on the catalyst surface and promote graphitization during heat treatment. Such active sites may also be more accessible with the observed larger surface area and hollow shell design. The hierarchical pore sizes also facilitate mass transport. In addition, we proposed the major active sites as the Fe−Nx species in the carbon-nanoshells. Such hollow carbon-nanoshells not only can serve as high-performance electrocatalysts for ORR, but also offer a new synthesis route to prepare efficient electrode materials.

2.5 Reference

1. Borup, R.; Meyers, J.; Pivovar, B.; Kim, Y. S.; Mukundan, R.; Garland, N.; Myers, D.; Wilson, M.; Garzon, F.; Wood, D.; Zelenay, P.; More, K.; Stroh, K.; Zawodzinski, T.; Boncella, J.; McGrath, J. E.; Inaba, M.; Miyatake, K.; Hori, M.; Ota, K.; Ogumi, Z.; Miyata, S.; Nishikata, A.; Siroma, Z.; Uchimoto, Y.; Yasuda, K.; Kimijima, K.-i.; Iwashita, N. *Chem. Rev.* **2007**, *107*, 3904-3951.
2. Gong, K.; Du, F.; Xia, Z.; Durstock, M.; Dai, L. *Sci.* **2009**, *323*, 760-764.
3. Li, Y.; Zhou, W.; Wang, H.; Xie, L.; Liang, Y.; Wei, F.; Idrobo, J.-C.; Pennycook, S. J.; Dai, H. *Nat. Nanotechnol.* **2012**, *7*, 394-400.
4. Qing, L.; Ruiguo, C.; Jaephil, C.; Gang, W. *Adv. Energy Mater.* **2014**, *4*, 1301415 (1301419 pp.)-1301415 (1301419 pp.).
5. Gang, W.; More, K. L.; Johnston, C. M.; Zelenay, P. *Sci.* **2011**, *332*, 443-447.
6. Kong, A.; Zhu, X.; Han, Z.; Yu, Y.; Zhang, Y.; Dong, B.; Shan, Y. *ACS Catal.* **2014**, *4*, 1793-1800.
7. Zhang, L.; Kim, J.; Dy, E.; Ban, S.; Tsay, K.-c.; Kawai, H.; Shi, Z.; Zhang, J. *Electrochim. Acta* **2013**, *108*, 814-819.
8. Lin, L.; Zhu, Q.; Xu, A. W. *J. Am. Chem. Soc.* **2014**, *136*, 11027-11033.
9. Lee, J.-S.; Park, G. S.; Kim, S. T.; Liu, M.; Cho, J. *Angew. Chem. Int. Ed. Engl.* **2013**, *52*, 1026-1030.

10. Aijaz, A.; Fujiwara, N.; Xu, Q. *J. Am. Chem. Soc.* **2014**, *136*, 6790-6793.

11. Liang, H.-W.; Wei, W.; Wu, Z.-S.; Feng, X.; Muellen, K. *J. Am. Chem. Soc.* **2013**, *135*, 16002-16005.

12. Ito, Y.; Qiu, H. J.; Fujita, T.; Tanabe, Y.; Tanigaki, K.; Chen, M. *Adv. Mat.* **2014**, *26*, 4145-4150.

13. Han, C. L.; Wang, S. P.; Wang, J.; Li, M. M.; Deng, J.; Li, H. R.; Wang, Y. *Nano Res.* **2014**, *7*, 1809-1819.

14. Zhou, M.; Yang, C. Z.; Chan, K. Y. *Adv. Energy Mater.* **2014**, *4*, 1400840-1400844.

15. Sanetuntikul, J.; Hang, T.; Shanmugam, S. *Chem. Commun.* **2014**, *50*, 9473-9476.

16. Wang, H.; Bo, X.; Wang, A.; Guo, L. *Electrochem. Commun.* **2013**, *36*, 75-79.

17. Yu, Y. M.; Zhang, J. H.; Xiao, C. H.; Zhong, J. D.; Zhang, X. H.; Chen, J. H. *Fuel Cells* **2012**, *12*, 506-510.

18. Schaefer, Z. L.; Gross, M. L.; Hickner, M. A.; Schaak, R. E. *Angew. Chem. Int. Ed. Engl.* **2010**, *49*, 7045-7048.

19. Li, N.; Zhang, X.; Chen, S.; Hou, X. *J. Phys. Chem. Solids* **2011**, *72*, 1195-1198.

20. Kim, J.; Kim, H. S.; Lee, N.; Kim, T.; Kim, H.; Yu, T.; Song, I. C.; Moon, W. K.; Hyeon, T. *Angew. Chem. Int. Ed. Engl.* **2008**, *47*, 8438-8441.

21. Ruggeri, S.; Dodelet, J.-P. *J. Electrochem. Soc.* **2007**, *154*, B761-B769.

22. Charreteur, F.; Jaouen, F.; Ruggeri, S.; Dodelet, J.-P. *Electrochim. Acta* **2008**, *53*, 2925-2938.

23. Wen, Z.; Ci, S.; Hou, Y.; Chen, J. *Angew. Chem. Int. Ed. Engl.* **2014**, *53*, 6496-6500.

24. Wu, G.; Zelenay, P. *Acc. Chem. Res.* **2013**, *46*, 1878-1889.

25. Guo, S.; Zhang, S.; Sun, S. *Angew. Chem. Int. Ed. Engl.* **2013**, *52*, 8526-8544.

26. Wang, L.; Yang, R. T. *J. Phys. Chem. C* **2012**, *116*, 1099-1106.

27. Sumida, K.; Rogow, D. L.; Mason, J. A.; McDonald, T. M.; Bloch, E. D.; Herm, Z. R.; Bae, T. H.; Long, J. R. *Chem. Rev.* **2012**, *112*, 724-781.

28. Phan, A.; Doonan, C. J.; Uribe-Romo, F. J.; Knobler, C. B.; O'Keeffe, M.; Yaghi, O. M. *Acc. Chem. Res.* **2010**, *43*, 58-67.

29. Ferrandon, M.; Kropf, A. J.; Myers, D. J.; Artyushkova, K.; Kramm, U.; Bogdanoff, P.; Wu, G.; Johnston, C. M.; Zelenay, P. *J. Phys. Chem. C* **2012**, *116*, 16001-16013.

30. Jaouen, F.; Proietti, E.; Lefevre, M.; Chenitz, R.; Dodelet, J.-P.; Wu, G.; Chung, H.

31. Kothandaraman, R.; Nallathambi, V.; Artyushkova, K.; Barton, S. C. *Appl. Catal., B* **2009**, *92*, 209-216.

32. Gang, W.; Johnston, C. M.; Mack, N. H.; Artyushkova, K.; Ferrandon, M.; Nelson, M.; Lezama-Pacheco, J. S.; Conradson, S. D.; More, K. L.; Myers, D. J.; Zelenay, P. *J. Mater. Chem.* **2011**, *21*, 11392-11405.

33. Zhao, Y.; Watanabe, K.; Hashimoto, K. *J. Am. Chem. Soc.* **2012**, *134*, 19528-19531.

34. Kong, A.; Kong, Y.; Zhu, X.; Han, Z.; Shan, Y. *Carbon* **2014**, *78*, 49-59.

35. Hu, Y.; Jensen, J. O.; Zhang, W.; Cleemann, L. N.; Xing, W.; Bjerrum, N. J.; Li, Q. *Angew. Chem. Int. Ed. Engl.* **2014**, *53*, 3675-3679.

36. Hou, Y.; Huang, T.; Wen, Z.; Mao, S.; Cui, S.; Chen, J. *Adv. Energy Mater.* **2014**, *4,* 1400337-1400344.

37. Ramaswamy, N.; Tylus, U.; Jia, Q.; Mukerjee, S. *J. Am. Chem. Soc.* **2013**, *135*, 15443-15449.

CHAPTER THREE: NANOPOROUS CARBON DERIVED FROM A FUNCTIONALIZED METAL-ORGANIC FRAMEWORK AS HIGHLY EFFICIENT OXYGEN REDUCTION ELETROCATALYSTS

3.1 Introduction

Development of non-precious metal catalysts (NPMCs) has become a well-known strategy to replace the platinum-based catalysts for the ORR at the cathode of fuel cells, metal–air batteries and air-breathing cathodes in industrial electrocatalytic processes.[1-5] Among different alternative NPMCs catalysts, transition-metal-coordinating nitrogen-doped carbon catalysts (especially, Fe) (Fe-N/C) have been found to possess excellent catalytic activity and durability.[2, 3, 6-17]

Metal–organic frameworks (MOFs) as new classes of crystalline porous materials with high surface area, large pore volume and uniform pore distribution have been used as templates and precursors for the formation of high quality porous carbons for ORR application.[8, 12, 18-46] Up to now, two main strategies have been developed for the synthesis of Fe-N/C based carbon from MOFs. In one approach, Fe based MOFs materials are used as the sole precursors for the electrocatalyst preparation. However, there are not many Fe based MOFs containing Fe-N bonding. Materials with Fe-N sites are considered important for the ORR catalytic activity. Because of scarcity of Fe-N bond containing MOFs and their limited ORR activity, an

alternative approach has been developed which utilizes non-Fe based MOFs with high nitrogen content and large pore volume as the support for Fe and N precursor. In order to synthesize transition-metal-containing nitrogen-doped carbon catalysts from MOFs, the metal-functionalized guest molecules, such as iron and nitrogen containing complexes are incorporated as whole into the nanospace of the MOF via impregnation.[18, 28, 30] Nevertheless, this method is often limited by the window size of MOF materials which is either inaccessible for larger sized molecules or the pore size is too big for smaller sized molecules that can leach out from the pore easily. Self-assembly of small species in the framework has demonstrated to be able to circumvent this limitation.[47-49] Another way to overcome this limitation is to design MOF materials with strong interaction sites for the target species.[47-49] Some open coordination sites or functional groups in the ligands attract the target species and serve as the specific interaction sites and be further utilized for the post-synthesis. [47-49] This inspires us to use a MOF with open coordination sites in the ligand to encapsulate the selected guest molecules step-by-step with the targeted chemical functions. Compared with traditional impregnation method, this approach can allow the encapsulation of functional guest molecules in a larger size range domain leading to materials with desirable properties.

Another crucial factor for the selection of MOFs to synthesize nitrogen containing porous carbons depends on the nitrogen sources contained on the MOFs. Among these, the N-rich zeolitic imidazolate frameworks (ZIFs) are a family of suitable candidates for preparing nitrogen-doped porous carbons.[20, 25, 26, 28, 34, 38, 42, 44] Other

nitrogen-containing MOFs, such as Fe-BTT, amino-MIL-53(Al), can also be regarded as precursor and nitrogen source to synthesize porous carbons.[35, 40] However, little reports are focused on the preparation of nitrogen doped porous carbon from MOFs precursor with pyridine-based ligands.[41, 50] Pyridine-based ligands with N atoms embedding in the aromatic ring can facilitate the incorporation of nitrogen containing active sites into the graphitized carbon matrix in the presence of iron.[7, 41, 50, 51]

3.2 Experimental Section

3.2.1. Synthesis of MOF-253 Al(OH)(bpydc):[53, 54] A mixture of $AlCl_3 \cdot 6H_2O$ (0.625 mmol), glacial acetic acid (15.0 mmol) and bpydc (0.625 mmol) (bpydc = 2, 2'-bipyridine-5, 5'-dicarboxylic acid) in 10 mL of N, N'-dimethylformamide (DMF) was added to a Teflon-capped 20 mL scintillation vial. The mixture was stirred for 30 min, and then heated on a hot plate at 120 °C for 24 h. The resulting white microcrystalline powder was then filtered and washed with DMF. After filtering, the resulting white powder was stirred in DMF at 80 °C for 3h, followed by washing with methanol via soxhlet extraction for 24 h and dried at 200 °C overnight in vacuum.

3.2.2 Synthesis of MOF-253-Fe: [53, 54] The compounds Al(OH)(bpydc) (3.5 mmol), $FeCl_2$ (3.5 mmol) were stirring for 2 h in acetonitrile (500 mL). The resulting solid was collected by filtration and washing with acetonitrile.

3.2.3 Synthesis of MOF-253-Fe-phen and MOF-253-Fe-phen-C: The above obtained dry MOF-253-Fe, 1,10-Phenanthroline (7 mmol) was stirred in acetonitrile (500 mL) for 6 h followed by filtration and dried for 12 h under vacuum. The MOF-253-Fe-phen composite was then transferred into a quartz boat and pyrolyzed at 900 °C in argon atmosphere for 3 hours with a heating speed of 3 °C/min. Finally, the materials labelled as MOF-253-Fe-phen-C were etched with 1M HCl to remove Al containing particles that are produced during pyrolysis.

3.2.4 Synthesis of MOF-253-(Fe-Phen) and MOF-253-(Fe-Phen)-C: The compound Al(OH)(bpydc) (3.5 mmol) is immersed into the mixed solution of $FeCl_2$ (3.5 mmol) and 1,10-Phenanthroline (7 mmol) (with a ratio of $FeCl_2$ to 1,10-Phenanthroline of 1:2) in acetonitrile at RT for 6 hours. After filtration and dried in vacuum, the composited was transferred into a quartz boat and pyrolyzed at 900 °C in argon atmosphere for 3 hours with a heating speed of 3 °C/min. Finally, the materials denoted as MOF-253-(Fe-Phen)-C were etched with 1M HCl.

3.2.5 Electrocatalytic activity measurements

Electrochemical characterization of the catalysts was performed in a conventional three-electrode cell using CHI760D electrochemical workstation (CH Instruments, USA) controlled at room temperature and under atmospheric pressure. Ag/AgCl and platinum wire were used as reference and counter electrodes, respectively. All potentials in this report were converted into reversible hydrogen electrode (RHE).

A ring-disk electrode (RDE) with a glassy carbon disk and a Pt ring was served as the substrate for the working electrode. The catalyst ink was prepared by mixing the catalyst powder (10 mg) with 80 μL Nafion solution (5wt %) and 1.2 ml ethanol in an ultrasonic bath. Then 5.0 μL of catalyst ink was pipetted onto the GC electrode with a catalyst loading of 0.2 mg cm^{-2} in 0.1 M KOH. In 0.1M $HClO_4$ solutions, 20 μL of catalyst ink was deposited onto the GC electrode corresponding a catalyst loading of 0.8 mg cm^{-2}. As a comparison, commercial 20 wt.% platinum on Vulcan carbon black (Pt/C, Alfa Aesar) was prepared by blending Pt/C (10 mg) with 80 μL Nafion solution (5 wt.%) and 1.2 ml ethanol in an ultrasonic bath. A Pt loading about 20 μg cm^{-2} was applied both in alkaline and acidic condition.

Linear sweep voltammetry (LSV) polarization curves for the oxygen reduction reaction (ORR) were measured in an oxygen saturated 0.1 M KOH and 0.1 M $HClO_4$ electrolyte with a sweep rate of 10 mV s-1 at various rotating speeds from 400 to 2500 rpm. The cyclic voltammogram (CV) were recorded in solutions saturated with either Ar or O_2 gas without rotation with same sweep rate as that of

LSV curve. The electron transfer number (n) and kinetic current density (j_K) were analyzed on the basis of Koutecky– Levich equations shown in below:

$$1/j=1/j_L+1/j_K$$

$$j_L=0.62nFCD^{2/3}\upsilon^{-1/6}w^{-1/2}=Bw^{-1/2}$$

$$1/j=1/Bw^{-1/2}+1/j_K$$

where $B=0.62nFC_0 D_0^{2/3} \upsilon^{-1/6}$, j was the measured current density, j_K and j_L were the kinetic- and diffusion-limiting current densities, w was the rotation speed, n was the electron transfer number, F was the Faraday constant (F = 96485 C mol^{-1}), C was the bulk concentration of O_2, D was the diffusion coefficient of dissolved oxygen, v was the kinematic viscosity of the electrolyte.

3.2.6 Characterization

The crystal structures of the materials were characterized by X-ray diffractometer (XRD) (D/Max2000, Rigaku) using a Bruker D8-Advance powder diffractometer operating at 40 kV, 40 mA for Cu Kα radiation (λ=1.5406 Å). The morphology and composition of the samples were analyzed with a Tecnai T12 transmission electron microscope (TEM) and a Philips FEI XL30 field emission scanning electron microscope (FESEM) equipped with a LaB6 electron gun, and an EDAX energy-dispersive spectrometer (EDS). The surface properties and composition of the materials were studied by X-ray photoelectron spectroscopy (XPS)

characterization using a Kratos AXIS ULTRADLD XPS system equipped with an Al K monochromated X-ray source and a 165 mm electron energy hemispherical analyzer. The shifts in energy (charging) of the XPS spectra were calibrated using the C1s peak at 284.6 eV as a reference peak. Nitrogen sorption analysis was conducted at 77 K using a Micromeritics ASAP 2020 surface-area and pore-size analyzer. The specific surface areas were calculated using the Brunauer–Emmett–Teller (BET) equation from the nitrogen adsorption data in the relative range (P/P_0) of 0.04-0.20. The pore size distribution (PSD) plot was recorded from the adsorption and desorption branch of the isotherm based on the Barrett–Joyner–Halenda (BJH) and Horvath-Kawazoe (H-K) model. The elemental analysis was performed by the Atlantic Microlab in Georgia. Inductively Coupled Plasma analysis were performed with radial viewing ICP-OES system HORIBA Jobin Yvon ULTIMA 2 (Jobin Yvon, Longjumeau, France) equipment to determine the Al and Fe contents.

3.3 RESULTS AND DISCUSSION

3.3.1 Catalyst Preparation and Characterization

For the above purpose, we design and synthesize iron-nitrogen doped porous carbon materials as electrocatalysts for ORR from pyridine-containing MOFs as illustrated in Scheme 3.1. Here, Al(OH)(bpydc) (MOF-253, bpydc = 2, 2'-bipyridine-5, 5'-

dicarboxylic acid) is selected as the MOF precursor because of its high surface area, high chemical and thermal stability.[54, 55] Moreover, this framework constitutes open 2, 2′-bipyridine nitrogen sites[54, 55] which are superior for chelating with iron to form iron-nitrogen species throughout the crystal. The synthetic strategy used in this work includes two steps: first chelating $FeCl_2$ into MOF-253 via 2, 2′- bipyridine ligand subsequently 1, 10-phenanthroline is introduced via impregnation. MOF-253 with open 2, 2′- bipyridine nitrogen sites not only serves as carbon and nitrogen precursors but also provides chelate bonding sites for iron cation, leading to iron-nitrogen bonds distributing over the synthesized materials.

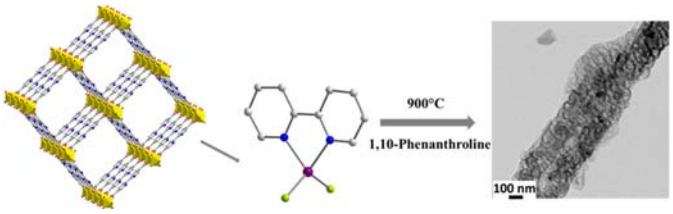

Scheme 3.1 Model structure of MOF-253-Fe, through post synthetic modifications of MOF-253 with $FeCl_2$ and subsequent synthesis of Fe, N doped porous carbon materials (MOF-253-phen-C). Yellow octahedral represent Al atoms, while purple, green, red, blue, and grey spheres represent Fe, Cl, O, N, and C atoms, respectively; H atoms are omitted for clarity.

MOF-253 is synthesized according to the procedure reported in literature.[54, 55] After the de-solvating process, it is modified with $FeCl_2$ in acetonitrile to form Fe incorporated compound that maintained the structure of MOF-253 as evidenced by X-ray Diffraction

(XRD) and X-ray Photoelectron Spectroscopy (XPS). The formed framework structure with Fe incorporated is called as MOF-253-Fe (Figure 3.1 and 3.2). The atomic ratio of Fe/Al in MOF-253-Fe is measured to be 0.7 by inductively coupled plasma optical emission spectrometry (ICP-OES) analysis (ESI).

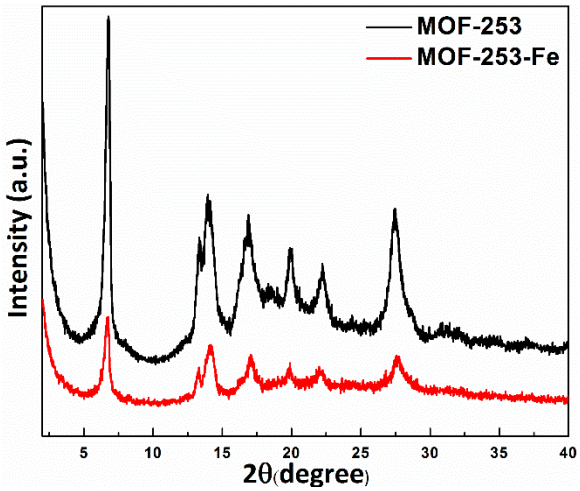

Figure 3.1 XRD patterns of MOF-253 and MOF-253-Fe.

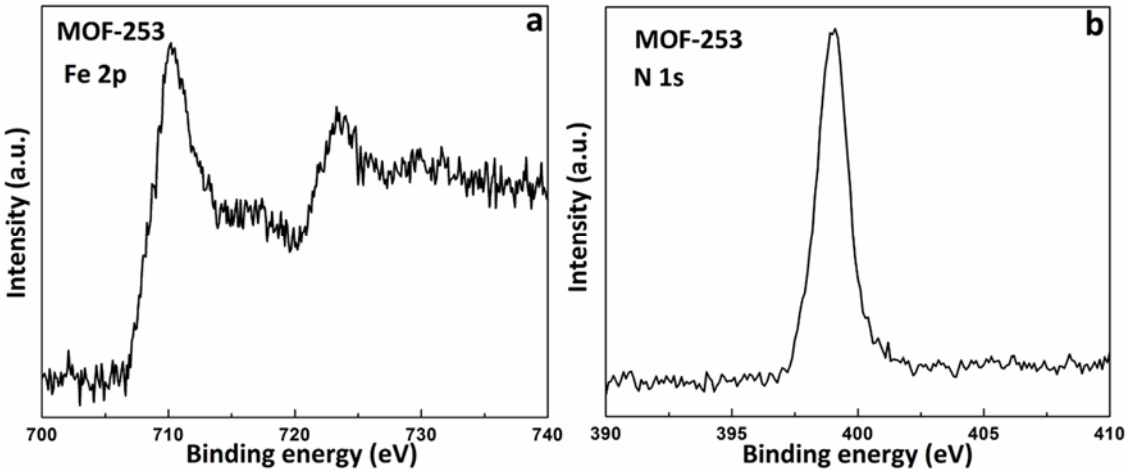

Figure 3.2 High-resolution Fe 2p and N 1s XPS spectra of MOF-253-Fe.

Since 1, 10-Phenanthroline can act as aromatic nitrogen source and promote the doping of nitrogen atoms in the graphitized carbon matrix at high temperature,[51, 55] it is introduced to MOF-253-Fe compound. After mixing of 1, 10-phenanthroline and MOF-253-Fe, the obtained solid composites (denoted as MOF-253-Fe-phen) are then thermally treated at 900 °C under Ar atmosphere. The annealed materials are then etched with diluted HCl in order to remove the aluminium in the framework. Figure 3.3 shows the XRD pattern of the sample after pyrolysis (denoted as MOF-253-Fe-phen-C) which is graphitic carbon with the (002) and (100) planes appearing at diffraction peaks of 26.1° and 43.2°.[8, 57, 58]

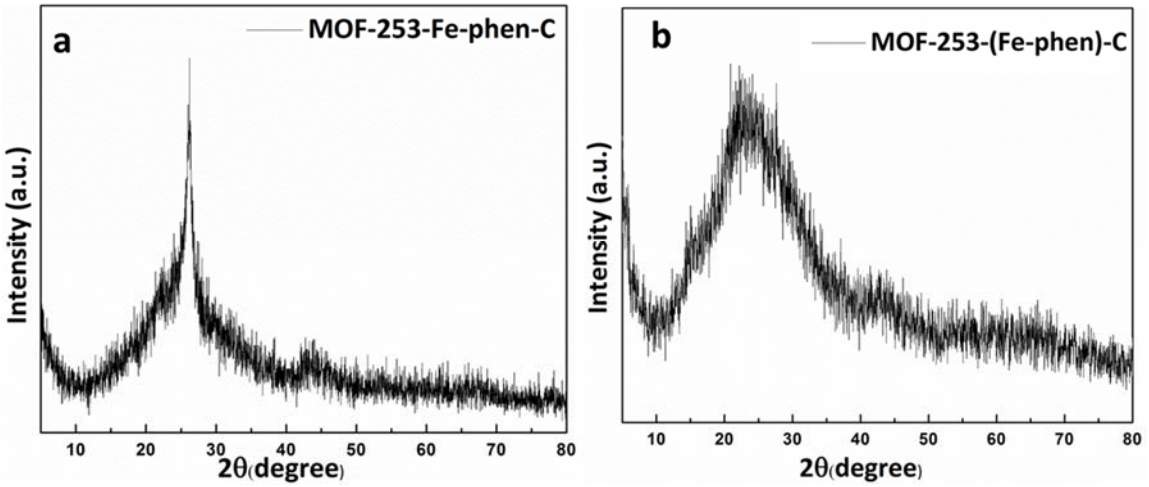

Figure 3.3 XRD patterns of MOF-253-Fe-phen-C (a), MOF-253-(Fe-Phen)-C (b).

The obtained MOF-253-Fe-phen-C particles are hollow carbon spheres with a diameter of 60 nm (Figure 3.4a, b). Such features are favourable for large surface areas, excellent electrolyte and oxygen diffusion.[28, 59, 60] Further inspection using transmission electron microscopy (HRTEM) shows that the MOF-253-Fe-phen-C features a carbon crystalline structure, as seen by the distinct lattice fringes with a spacing of 2-5 nm (0.34 nm), corresponding with the (002) plane of graphite (Figure 3.4c). Close observation reveals that some of the Fe_3C nanoparticles are wrapped by graphitic carbon layers (Figure 3.4c) that is also supported by the corresponding energy-dispersive X-ray spectroscopy (EDS) (Figure 3.5). Additionally, the selected area electron diffraction (SAED) pattern shows several rings and scattered dots (Figure 3.4d). Rings can be assigned to the diffraction planes of the graphitic carbon shells, while those scattered dots correspond to the diffraction of crystalline Fe_3C core.[8, 57, 58] Such core-shell structure was reported previously and is believed to contribute to the stability and activity in ORR.[8] In addition, graphitic carbon layers can efficiently prevent Fe_3C species aggregation.

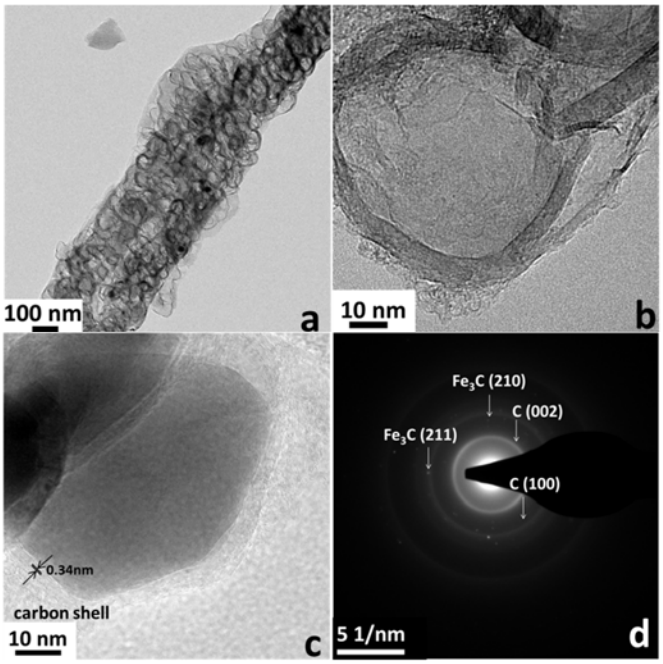

Figure 3.4 TEM images (a), HRTEM images (b, c) and SAED patterns (d) of MOF-253-Fe-phen-C.

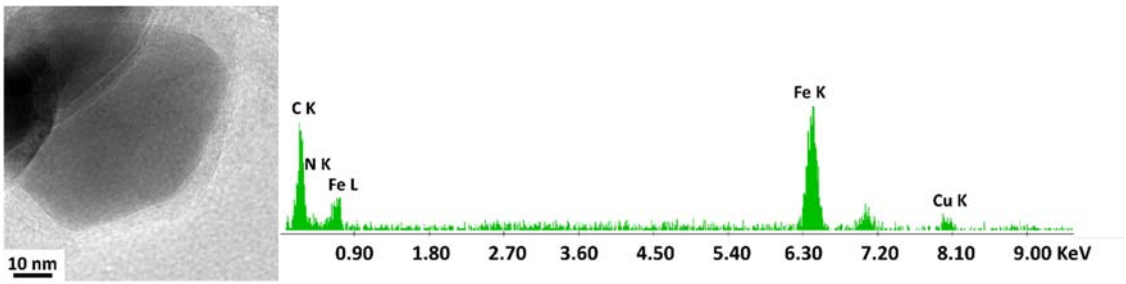

Figure 3.5 EDX spectrum of Fe_3C nanoparticles which are wrapped by carbon graphitic carbon layers in MOF-253-Fe-phen-C.

The Brunauer–Emmett–Teller (BET) specific surface area of MOF-253-Fe-phen-C is 538 m^2 g^{-1}. The close-to type IV N_2 adsorption–desorption isotherm with a clear hysteresis loop illustrates the mesoporous and microporous nature of the obtained MOF-253-Fe-Phen–C materials (Figure 3.6).[7, 22] These hierarchical pore feature is favourable for the adsorption and transportation of O_2, resulting in enhanced ORR activity. [7, 22]

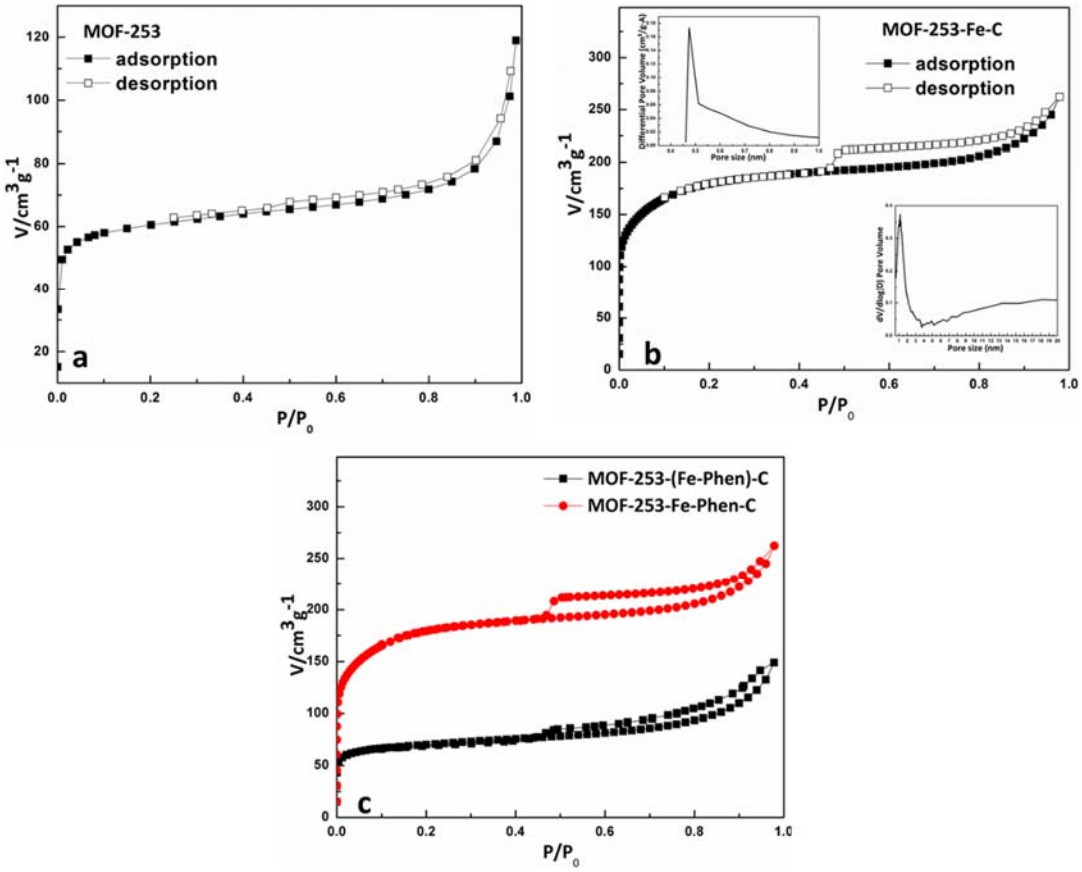

Figure 3.6 Nitrogen adsorption/desorption isotherms and the corresponding pore size distribution curves for a), MOF-253, b) MOF-253-Fe-Phen-C, c), MOF-253-(Fe-phen)-C.

XPS analysis is performed to analyse the content and chemical state of the nitrogen and iron in MOF-253-Fe-phen-C. The survey XPS spectrum (Figure 3.7) of MOF-253-Fe-phen-C reveals the presence of C, N, and Fe elements. The N 1s spectrum (Figure 3.8) are deconvoluted into three peaks at 397.9, 399.2, and 400.8 eV, which can be assigned to pyridinic, metal-coordinated and graphitic N, respectively.[7, 61] The metal-coordinated and graphitic N is reported to play a crucial role in oxygen reduction.[62-64] These two types of ORR active nitrogen are of high contents which are 22.31 % and 60.68 % in our MOF-253-Fe-phen-C electrocatalyst, which leads to a high catalytic activity. The high resolution Fe 2p spectrum of MOF-253-Fe-phen-C can be deconvoluted into three peaks with binding energies of 710.9, 717.0, and 721.0 eV (Figure 3.8), among which the binding energies of the Fe2p (around 711 eV) could be ascribed to the N-coordinated Fe^{3+} or Fe^{2+}.[15, 56, 64] Metal species stabilized by nitrogen coordination are generally believed to contribute positively in ORR activity and durability.[15, 56, 64]

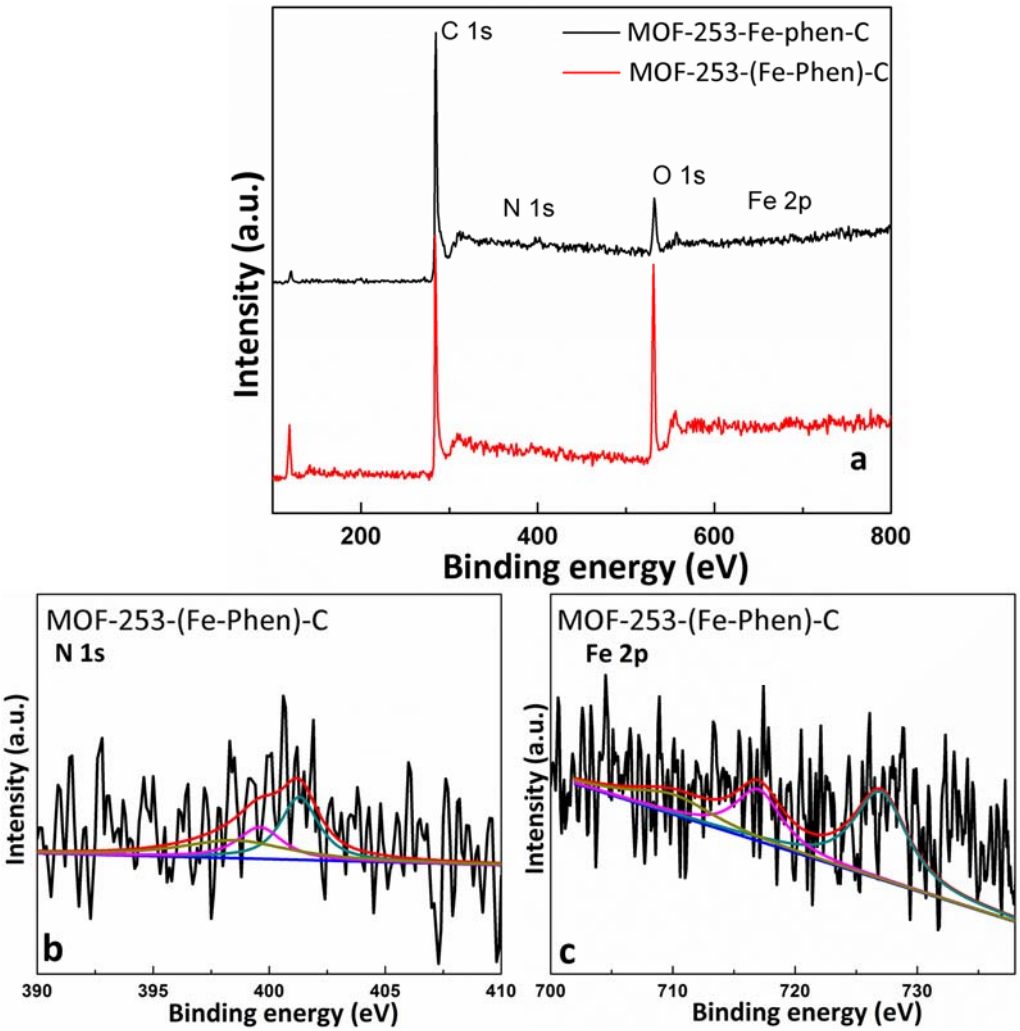

Figure 3.7 XPS survey scan of MOF-253-Fe-phen-C and MOF-253-(Fe-Phen)-C (a), high-resolution N 1s XPS spectra of MOF-253-(Fe-Phen)-C (b), high-resolution Fe 2p XPS spectra of MOF-253-(Fe-Phen)-C (c).

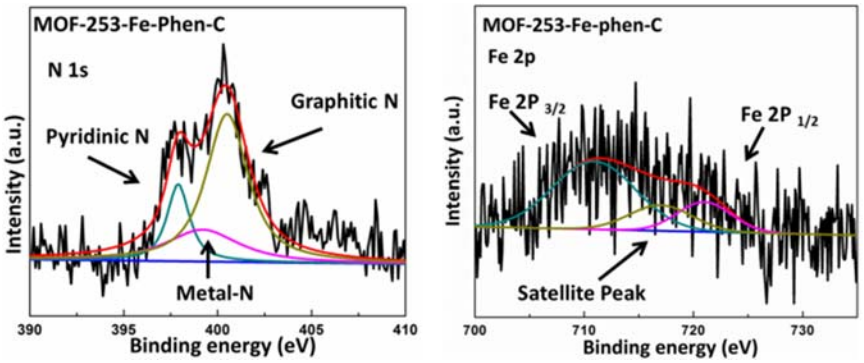

Figure 3.8 High-resolution N 1s and Fe 2p XPS spectra of MOF-253-Fe-phen-C.

For comparison, a control experiment is performed using impregnation method to encapsulate Fe-Phen complexes directly. Here MOF-253 is immersed into the mixed solution of $FeCl_2$ and 1,10-Phenanthroline with a ratio of $FeCl_2$ to 1,10-Phenanthroline of 1:2 for 6 hours. After filtration, the materials denoted as MOF-253-(Fe-Phen) is pyrolyzed and etched under similar conditions as that of MOF253-Fe-Phen. After pyrolysis and etching with HCl, the materials (denoted as MOF-253 -(Fe-Phen)-C) contains 49.2 wt.% less nitrogen and 64.9 wt.% less Fe content than that of MOF-253-Fe-phen-C which can be seen in the elemental analysis and ICP measurement (Table 3.1 and 3.2). The lower Fe content of MOF-253-(Fe-phen)-C could be caused by the low efficient incorporation method of Fe-Phen complexes. Before pyrolysis, the Fe content in MOF-253 -(Fe-Phen) is 88.5 wt. % less than that of MOF-253-Fe-Phen (Table 3.1 and 3.2). This could be due to the relatively small windows of MOF-253 (window size 1.11nm X 1.11nm) compared to Fe-1,10-Phenanthroline complex $Fe(Phen)_2Cl_2$ (molecule dimensions 1.24 nm X 1.24 nm). The MOF-253-(Fe-Phen)-C shows much lower BET

surface area (210 m^2 g^{-1}) than MOF-253-Fe-phen-C (Figure 3.6). This could be due to that the Fe- 1,10-Phenanthroline entering the nanospace of MOFs can serve as template during the calcination to further support the framework. Due to the larger loading amount of Fe- 1,10-Phenanthroline in MOF-253-Fe-phen-C, it shows a larger surface area than that of MOF-253-(Fe-phen)-C. The control experiment highlights that the window limitation problems of MOFs can be circumvented in certainly degree. By applying step-by-step synthetic approach here, complexes larger than the window sizes of MOFs can be encapsulated into the cavity.

Table 3.1 Summarized iron contents by ICP-OES measurements.

Samples	MOF-253-Fe-phen	MOF-253-(Fe-Phen)-C	MOF-253-Fe-phen-C	MOF-253-(Fe-Phen)-C
Fe wt.%	5.50	0.63	0.77	0.27

Table 3.2 Elemental compositions of MOF-253-Fe-phen-C and MOF-253-(Fe-Phen)-C determined by elemental analysis.

Samples	C wt. %	H wt. %	N wt. %
MOF-253-Fe-phen-C	53.53	0.99	1.34
MOF-253-(Fe-Phen)-C	47.82	1.766	0.68

3.3.2 Catalytic Activity Evaluation

The electrocatalytic ORR properties of the MOF-253-Fe-phen-C catalysts are evaluated using ring-disk electrode (RDE) technique at a catalyst loading of 0.20 mg cm^{-2} in 0.1 M KOH at room temperature. For comparison, a state-of-the-art Pt/C (20 wt. % Pt, Alfa Aesar) catalyst is also tested. The influence of the pyrolysis temperature and the ratio of the MOF-253-Fe to 1,10-Phenanthroline were also investigated.[65] The best activity is achieved at 900°C with a ratio of MOF-253-Fe to 1,10-Phenanthroline of 1:2 as revealed by the onset and half-wave potentials in the ORR polarization plots (Figure 3.9).

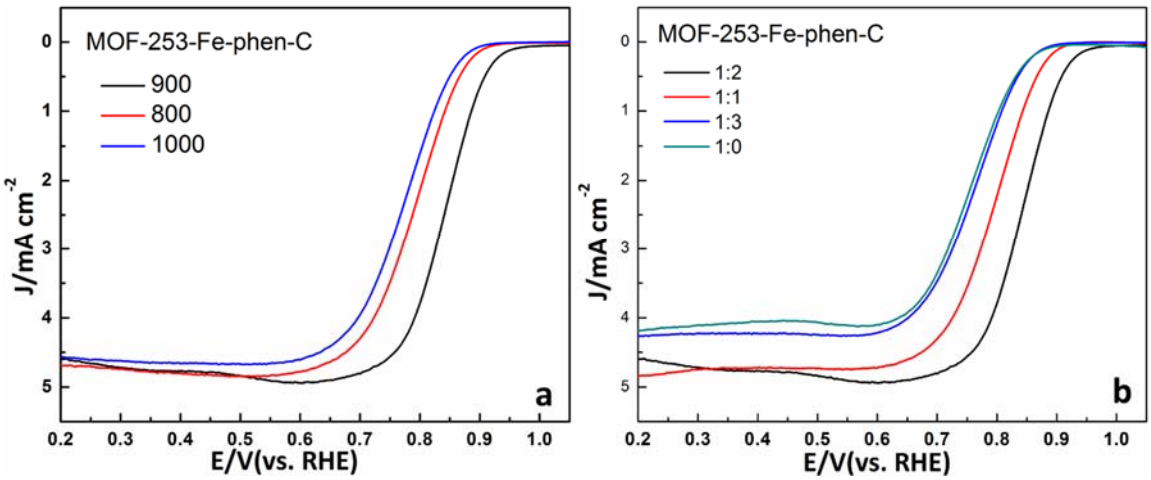

Figure 3.9 RDE voltammograms of MOF-253-Fe-phen-C pyrolyzed at different temperatures in O_2-saturated 0.1 M KOH (a), RDE voltammograms of MOF-253-Fe-phen-C pyrolyzed by heating the mixtures containing different molar ratio of MOF-253-Fe and 1, 10-Phenanthroline at 900 °C and HCl etching in O_2-saturated 0.1 M KOH. Note, 1:0 means that no 1, 10-Penanthroline is added in MOF-253-Fe precursor (b).

To examine the electrocatalytic activity of the MOF-253-Fe-phen-C catalyst, cyclic voltammetry (CV) scanning is carried out in 0.1M KOH aqueous solution saturated with Ar or O_2 gas at room temperature. The impressive ORR electrocatalytic performances of MOF-253-Fe-phen-C catalysts are presented by rotating disk electrode (RDE) experiments at 1600 rpm with a scan rate of 10 mV s^{-1}. Figure 3.10a shows that the onset potential for the MOF-253-Fe-phen-C catalyst in alkaline conditions (980 mV) is the same as that of Pt/ C (980 mV) and the half-wave potentials ($E_{1/2}$) is 840 mV, which is 20 mV more than that of Pt/ C. As shown in Figure 3.10b, a quasi-rectangular double-layer capacity current from -0.05 to 1.15 V (versus RHE) for MOF-253-Fe-phen-C in the Ar-saturated solution and a well-defined ORR peak in O_2 with a peak potential of 855 mV are observed, these are comparable to that of Pt/C (865 mV) (Figure 3.11).

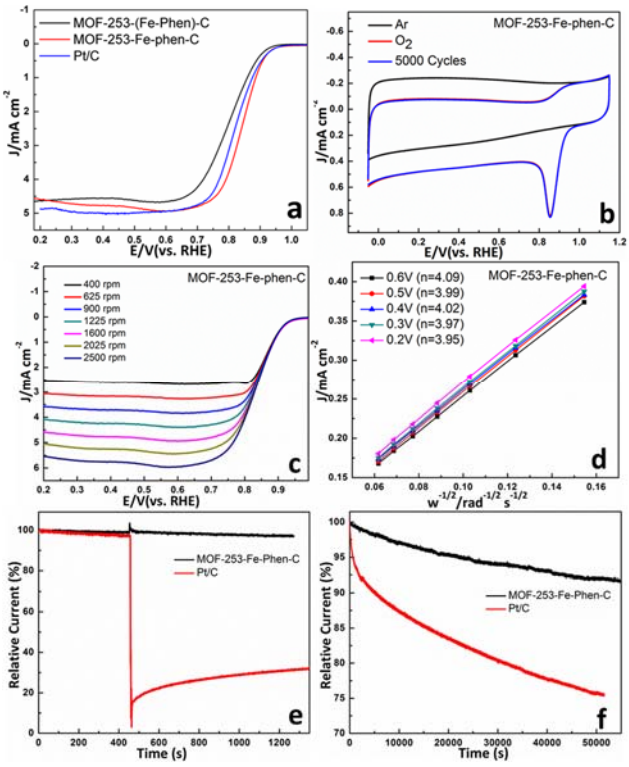

Figure 3.10 RDE voltammograms of MOF-253-Fe-phen-C, MOF-253-(Fe-Phen)-C and Pt/C (20 wt%) in O_2-saturated 0.1 M KOH (a), Cyclic voltammograms of MOF-253-Fe-phen-C in O_2-saturated 0.1 M KOH (b), RDE voltammograms at different rotation rates and Koutecky-Levich plots of MOF-253-Fe-phen-C in O_2-saturated 0.1 M KOH (c, d), Methanol crossover tests of MOF-253-Fe-phen-C and Pt/C by introducing 3 M methanol into the electrolyte at 400 s at 0.55 V vs. RHE in O_2-saturated 0.1 M KOH (e), The chronoamperometric responses (i–t) of MOF-253-Fe-phen-C and Pt/C at 0.55 V vs. RHE in O_2-saturated 0.1 M KOH (f).

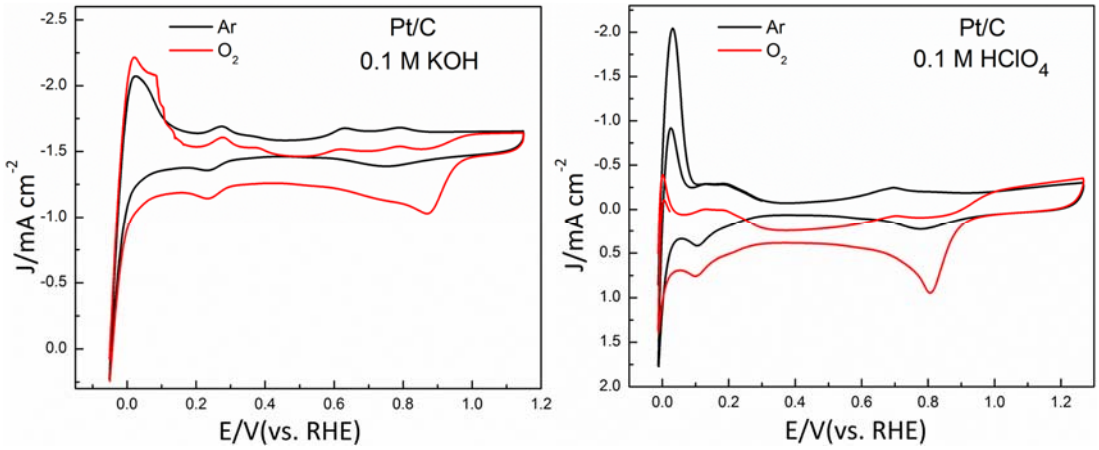

Figure 3.11 Cyclic voltammograms of Pt/C in O_2-saturated 0.1 M KOH and $HClO_4$.

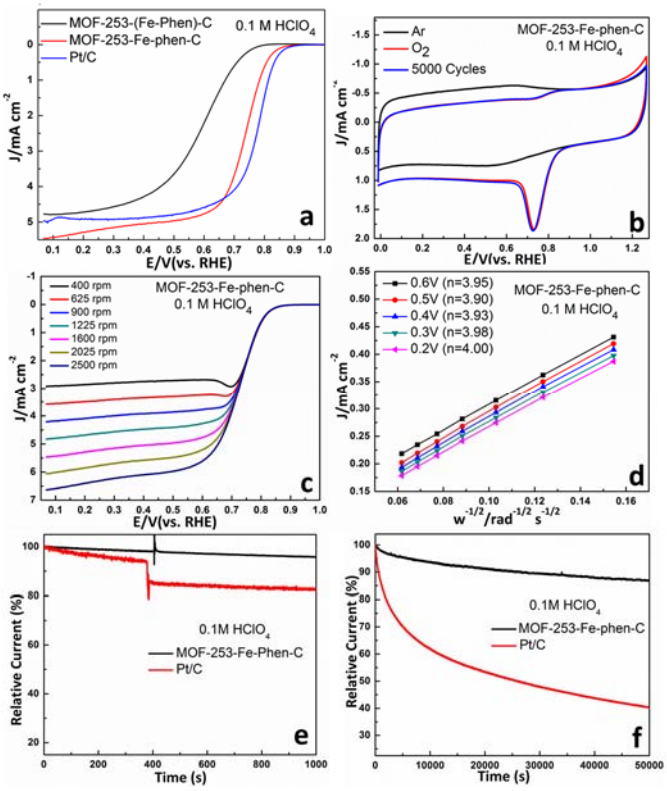

Figure 3.12 RDE voltammograms of MOF-253-Fe-phen-C, MOF-253-(Fe-Phen)-C and Pt/C (20 wt.%) in O_2-saturated 0.1 M $HClO_4$ (a), Cyclic voltammograms of MOF-253-Fe-phen-C in O_2-saturated 0.1 M $HClO_4$ (b), RDE voltammograms at different rotation rates and Koutecky-Levich plots of MOF-253-Fe-phen-C in O_2-saturated 0.1 M $HClO_4$ (c, d), Methanol crossover tests of MOF-253-Fe-phen-C and Pt/C by introducing 3 M methanol into the electrolyte at 400 s at 0.55 V vs. RHE in O_2-saturated 0.1 M $HClO_4$ (e), The chronoamperometric responses (i–t) of MOF-253-Fe-phen-C and Pt/C at 0.55 V vs. RHE in O_2-saturated 0.1 M $HClO_4$ (f). For all tests, the catalyst loading is 0.80 mg cm^{-2} and the scan rate is 10 mV s^{-1} in O_2-saturated 0.1 M $HClO_4$ for MOF-253-Fe-phen-C, MOF-253-(Fe-Phen)-C.

Generally, two electron reduction of oxygen that produces H_2O_2 is less desirable due to the production of hydrogen peroxide that is poisonous to catalysts.[65, 66] As shown in Figure 3.10c-d, the electron transfer numbers per oxygen molecule can be calculated from the slope of the K-L plots obtained from the polarization curves at various rotating speeds to be about 4 at 0.20–0.60 V in alkaline conditions, corresponding to the complete reduction of oxygen into water.

In addition, the MOF-253-Fe-phen-C catalyst also demonstrates pronounced electrocatalytic activity for ORR in acidic condition. As displayed in Figure 3.12a, MOF-253-Fe-phen-C catalyst shows comparable onset and half-wave potential to that of Pt/C at a catalyst loading of 0.80 mg cm^{-2} in 0.1 M $HClO_4$ at room temperature. The onset potential and the half-wave potential are only 20 mV and 30 mV less than those of Pt/C. As shown in Figure 3.12b, the cyclic voltammograms (CVs) of the MOF-253-Fe-phen-C catalyst in Ar and O_2 saturated 0.1 M $HClO_4$ show a well-defined reduction peak at 0.74 V in the O_2 saturated solution which is comparable to that of Pt/C. Calculated from the slope of the K-L plots (Figure 3.12c), the electron transfer number is about 4 (Figure 3.12d) at 0.20–0.60 V in acidic conditions, indicating that the four-electron reduction pathway to produce water as the main product is favoured.

Besides the activity, stability is another key factor for high-performance electrocatalysts. The stability test is conducted for MOF-253-Fe-phen-C by

chronoamperometry at a constant voltage of ~0.55V (vs. RHE) in O_2-saturated 0.1 M KOH and 0.1 M $HClO_4$ solutions at a rotation rate of 1600 rpm. As shown in Figure 3.10f and 3.12f, the MOF-253-Fe-phen-C exhibits a very slow attenuation and a high relative current of 93% and 88% are remained after 50,000 s in both solutions. In contrast, the ORR current on Pt/C declines sharply both in alkaline and acidic solutions as measured at the same conditions. In addition, a cycling stability test in O_2-saturated 0.1 M KOH and 0.1 M $HClO_4$ solution shows no peak potential or current density loss over the electrode of MOF-253-Fe-phen-C elecrocatalyst after 5,000 cycles, indicating a negligible degradation of surface active sites with time (Figure 3.10b and 3.12b). Notably, the MOF-253-Fe-phen-C catalyst also shows better tolerance toward methanol than that of Pt/C. MOF-253-Fe-phen-C shows a stable current-time (i–t) chronoamperometric response after the introduction of 3.0 M methanol in O_2-saturated 0.1 M KOH and 0.1 M $HClO_4$ solution (Figure 3.10e and 3.12e).

The values of onset and half wave potentials of the MOF-253-Fe-phen-C in alkaline and acidic are among the best in NPMCs reported to date.[11, 19, 65, 67] It is worth noting that the onset and half wave potential of MOF-253-(Fe-Phen)-C is much lower than that of MOF-253-Fe-phen-C in both alkaline and acidic condition. Overall, the high surface area, higher N and Fe content, hierarchical pore structural feature, along with Fe- N_x active sites on the MOF-253-Fe-phen-C

catalytic surface could all have contributed positively toward the ORR activity and durability of the synthesized materials in electrocatalytic performance.

3.4 Conclusions

In summary, we report a MOF derived iron-nitrogen doped hierarchical porous carbon material with highly efficient ORR performance through step-by-step post-synthetic modification. MOF-253 with open 2, 2′- bipyridine sites not only serves as precursor but also provides chelate bonding sites which can chelate with iron to form uniformly distributed iron-nitrogen species in the framework. With the introduction of 1, 10-phenanthroline into the channel of MOF-253-Fe, the catalytic activity of the materials is further improved. Compared to the commercial Pt/C catalysts, MOF-253-Fe-phen-C catalyst demonstrates excellent ORR activity, high selectivity (direct $4e^-$ reduction of oxygen to water) and stability both in alkaline and acidic condition. This work provides a new and facile synthesis route for the post-synthesis of MOF for ORR application, which set another example to expand the application of MOFs materials for fuel cells and other energy storage materials.

3.5 Reference

1 H. Wang, Y. Liang, Y. Li and H. Dai, *Angew. Chem. Int. Ed. Engl.*, 2011, 50, 10969.

2 G. Wu, K. L. More, C. M. Johnston and P. Zelenay, *Sci.*, 2011, 332, 443.

3 R. Cao, R. Thapa, H. Kim, X. Xu, M. Gyu Kim, Q. Li, N. Park, M. Liu and J. Cho, *Nat. Commun.*, 2013, 4, 2076.

4 G. Wu, K. L. More, C. M. Johnston and P. Zelenay, *Sci.*, 2011, 332, 443.

5 J. Sun, J. Zhang, M. Zhang, M. Antonietti, X. Fu and X. Wang, *Nat. Commun.,* 2012, 3, 1139.

6 G. Wu and P. Zelenay, *Acc. Chem. Res.,* 2013, 46, 1878.

7 A. Kong, X. Zhu, Z. Han, Y. Yu, Y. Zhang, B. Dong and Y. Shan, *Acs. Catal.*, 2014, 4, 1793.

8 Y. Hou, T. Huang, Z. Wen, S. Mao, S. Cui and J. Chen, *Adv. Energy Mater.,* 2014, 4, 1400337.

9 D. Deng, L. Yu, X. Chen, G. Wang, L. Jin, X. Pan, J. Deng, G. Sun and X. Bao, *Angew. Chem. Int. Ed. Engl.*, 2013, 52, 371.

10 S. Guo, S. Zhang and S. Sun, *Angew. Chem. Int. Ed. Engl.*, 2013, 52, 8526.

11 Y. Hu, J. O. Jensen, W. Zhang, L. N. Cleemann, W. Xing, N. J. Bjerrum and Q. Li, *Angew. Chem. Int. Ed. Engl.*, 2014, 53, 3675.

12 J. Tian, A. Morozan, M. T. Sougrati, M. Lefevre, R. Chenitz, J. P. Dodelet, D. Jones and F. Jaouen, *Angew. Chem. Int. Ed. Engl.*, 2013, 52, 6867.

13 J.-S. Lee, G. S. Park, S. T. Kim, M. Liu and J. Cho, *Angew. Chem. Int. Ed. Engl.*, 2013, 52, 1026.

14 F. Jaouen, E. Proietti, M. Lefèvre, R. Chenitz, J.-P. Dodelet, G. Wu, H. T. Chung, C. M. Johnston and P. Zelenay, *Energy Environ. Sci,* 2011, 4, 114.

15 H.-W. Liang, W. Wei, Z.-S. Wu, X. Feng and K. Muellen, *J. Am. Chem. Soc.,* 2013, 135, 16002.

16 L. Lin, Q. Zhu and A. W. Xu, *J. Am. Chem. Soc.,* 2014, 136, 11027.

17 M. Lefevre, E. Proietti, F. Jaouen and J. P. Dodelet, *Sci*., 2009, 324, 71.

18 Q. Li, P. Xu, W. Gao, S. Ma, G. Zhang, R. Cao, J. Cho, H. L. Wang and G. Wu, *Adv. Mater*. 2014, 26, 1378.

19 Z. Xiang, D. Cao, L. Huang, J. Shui, M. Wang and L. Dai, *Adv. Mater.,* 2014, 26, 3315.

20 D. Zhao, J. L. Shui, L. R. Grabstanowicz, C. Chen, S. M. Commet, T. Xu, J. Lu and D. J. Liu, *Adv. Mater*., 2014, 26, 1093.

21 M. Jahan, Z. Liu and K. P. Loh, *Adv. Funct. Mater.,* 2013, 23, 5363.

22 H. X. Zhong, J. Wang, Y. W. Zhang, W. L. Xu, W. Xing, D. Xu, Y. F. Zhang and X. B. Zhang, *Angew. Chem. Int. Ed. Engl*., 2014, 53, 14235.

23 S. Pandiaraj, H. B. Aiyappa, R. Banerjee and S. Kurungot, *Chem. Commun.,* 2014, 50, 3363.

24 Y. Zhang, X. Bo, C. Luhana, H. Wang, M. Li and L. Guo, *Chem. Commun.,* 2013, 49, 6885.

25 D. Zhao, J.-L. Shui, C. Chen, X. Chen, B. M. Reprogle, D. Wang and D.-J. Liu, *Chem. Sci.*, 2012, 3, 3200.

26 W. Chaikittisilp, N. L. Torad, C. Li, M. Imura, N. Suzuki, S. Ishihara, K. Ariga and Y. Yamauchi, *Chem. Eur. J*, 2014, 20, 4217.

27 S. Ma, G. A. Goenaga, A. V. Call and D. J. Liu, *Chem. Eur. J*, 2011, 17, 2063.

28 T. Palaniselvam, B. P. Biswal, R. Banerjee and S. Kurungot, *Chem. Eur. J*, 2013, 19, 9335.

29 J. Mao, L. Yang, P. Yu, X. Wei and L. Mao, *Electrochem. Commun.*, 2012, 19, 29.

30 A. Morozan, M. T. Sougrati, V. Goellner, D. Jones, L. Stievano and F. Jaouen, *Electrochim. Acta,* 2014, 119, 192.

31 J. Sanetuntikul and S. Shanmugam, *Electrochim. Acta,* 2014, 119, 92.

32 Z.-s. Yin, T.-h. Hu, J.-l. Wang, C. Wang, Z.-x. Liu and J.-w. Guo, *Electrochim. Acta,* 2014, 119, 144.

33 A. Morozan and F. Jaouen, *Energy Environ. Sci,* 2012, 5, 9269.

34 P. Zhang, F. Sun, Z. Xiang, Z. Shen, J. Yun and D. Cao, *Energy Environ. Sci.*, 2014, 7, 442.

35 F. Afsahi and S. Kaliaguine, *J. Mater. Chem. A,* 2014, 2, 12270.

36 M. Jiang, L. Li, D. Zhu, H. Zhang and X. Zhao, *J. Mater. Chem. A,* 2014, 2, 5323.

37 J. Li, Y. Chen, Y. Tang, S. Li, H. Dong, K. Li, M. Han, Y.-Q. Lan, J. Bao and Z. Dai, *J. Mater. Chem. A,* 2014, 2, 6316.

38 W. Xia, J. Zhu, W. Guo, L. An, D. Xia and R. Zou, *J. Mater. Chem. A,* 2014, 2, 11606.

39 G. Zhang, C. Li, J. Liu, L. Zhou, R. Liu, X. Han, H. Huang, H. Hu, Y. Liu and Z. Kang, *J. Mater. Chem. A,* 2014, 2, 8184.

40 X. Zhao, H. Zhao, T. Zhang, X. Yan, Y. Yuan, H. Zhang, H. Zhao, D. Zhang, G. Zhu and X. Yao, *J. Mater. Chem. A,* 2014, 2, 11666.

41 F. Afsahi, H. Vinh-Thang, S. Mikhailenko and S. Kaliaguine, *J. Power Sources,* 2013, 239, 415.

42 A. Aijaz, N. Fujiwara and Q. Xu, *J. Am. Chem. Soc.,* 2014, 136, 6790.

43 M. Jahan, Q. Bao and K. P. Loh, *J. Am. Chem. Soc.,* 2012, 134, 6707.

44 L. Zhang, Z. Su, F. Jiang, L. Yang, J. Qian, Y. Zhou, W. Li and M. Hong, *Nanoscale*, 2014, 6, 6590.

45 J. S. Li, S. L. Li, Y. J. Tang, K. Li, L. Zhou, N. Kong, Y. Q. Lan, J. C. Bao and Z. H. Dai, *Sci. Rep.*, 2014, 4, 5130.

46 Y. Chen, C. Wang, Z. Wu, Y. Xiong, Q. Xu, S. Yu, H. Jiang. *Adv. Mater.,* 2015, 27, 5010.

47 B. Li, Y. Zhang, D. Ma, T. Ma, Z. Shi, and S. Ma, *J. Am. Chem. Soc.,* 2014, 136, 1202.

48 M. Yoshizawa, T. Kusukawa, M. Fujita, K. Yamaguchi, *J. Am. Chem. Soc.* 2000, 122, 6311.

49

M. Shakeri, R. J. M. Klein Gebbink, P. E. de Jongh, and K. P. Krijn, *Angew. Chem. Int. Ed. Engl.*, 2013, 52, 10854.

50 D. Zhu, L. Li, J. Cai, M. Jiang, J. Qi and X. Zhao, *Carbon*, 2014, 79, 544.

51 Y. Wang, A. Kong, X. Chen, Q. Lin, and P. Y. Feng. *Acs Catal.,* 2015, 5, 3887.

52 W. Gang, K. L. More, C. M. Johnston and P. Zelenay, *Sci.*, 2011, 332, 443.

53 L. Zhang, J. Kim, E. Dy, S. Ban, K.-c. Tsay, H. Kawai, Z. Shi and J. Zhang, *Electrochim. Acta*, 2013, 108, 814.

54 E. D. Bloch, D. Britt, C. Lee, C. J. Doonan, F. J. Uribe-Romo, H. Furukawa, J. R. Long and O. M. Yaghi, *J. Am. Chem. Soc.,* 2010, 132, 14382.

55 T. Zhou, Y. Du, A. Borgna, J. Hong, Y. Wang, J. Han, W. Zhang and R. Xu, *Energy Environ. Sci,* 2013, 6, 3229.

56 A. Kong, Y. Kong, X. Zhu, Z. Han and Y. Shan, *Carbon*, 2014, 78, 49.

57 Z. Wen, S. Ci, F. Zhang, X. Feng, S. Cui, S. Mao, S. Luo, Z. He and J. Chen, *Adv. Mater*., 2012, 24, 1399.

58 H. T. Chung, J. H. Won and P. Zelenay, *Nat. Commun.,* 2013, 4, 1922

59 M. Zhou, C. Yang and K.-Y. Chan, *Adv. Energy Mater.,* 2014, 4, 1400840.

60 C. Han, S. Wang, J. Wang, M. Li, J. Deng, H. Li and Y. Wang, *Nano Res.,* 2014, 7, 1809.

61 A. Kong, B. Dong, X. Zhu, Y. Kong, J. Zhang and Y. Shan, *Chem. Eur. J*, 2013, 19, 16170.

62 S. Yang, X. Feng, X. Wang and K. Mullen, *Angew. Chem. Int. Ed. Engl.*, 2011, 50, 5339.

63 W. Gang, C. M. Johnston, N. H. Mack, K. Artyushkova, M. Ferrandon, M. Nelson, J. S. Lezama-Pacheco, S. D. Conradson, K. L. More, D. J. Myers and P. Zelenay, *J. Mater. Chem.,* 2011, 21, 11392;

64 Y. Zhao, K. Watanabe and K. Hashimoto, *J. Am. Chem. Soc.,* 2012, 134, 19528.

65 L. Lin, Q. Zhu and A. W. Xu, *J. Am. Chem. Soc.,* 2014, 136, 11027.

66 T. N. Ye, L. B. Lv, X. H. Li, M. Xu and J. S. Chen, *Angew. Chem. Int. Ed. Engl.*, 2014, 53, 6905.

67 W. Wei, H. Liang, K. Parvez, X. Zhuang, X. Feng and K. Mullen, *Angew. Chem. Int. Ed. Engl.*, 2014, 53, 1570.

CHAPTER FOUR: POROUS CARBON NANOMATERIALS DERIVED FROM MOFS IN MOLTEN SALTS FOR OXYGEN REDUCTION REACTION AND GAS ADSORPTION

4.1 Introduction

It is well-known that carbon dioxide (CO_2) released into the atmosphere has harmful effects on the environment such as the greenhouse effect and ocean acidification.[1] CO_2 levels in the atmosphere have been increasing steadily over the time and it continue to rise at the current rate. Fossil fuel burning have been identified as the major reason for the increase of CO_2 concentrations in the atmosphere. Over the next decades, fossil fuels would remain a large part of the energy source. This triggers commence interest in developing cost-efficient methods and materials for CO_2 capture nowadays.[1-3] CO_2 can be captured by physisorption using different solid absorbents, such as carbon, zeolite, metal–organic frameworks (MOFs), organic–inorganic hybrid/composite adsorbents, calcium oxide, and others.[1] Compared with chemisorption, physisorption of CO_2 can provide the regeneration of adsorbents by applying minimal heat or through the vacuum swing adsorption process at room temperature. Of these adsorbents, porous carbon material has attracted much interest due to its low cost, lightweight, large surface area, porous structure, and high physiochemical stability. Moreover, heteroatoms such as nitrogen, boron, sulfur, and oxygen doped into the porous carbons can tune the properties of carbon materials.[3-5] Among them, nitrogen doped carbon materials arouse a lot of attention for

CO_2 capture because it can lead to basicity and charge delocalization in the vicinity of the carbon matrix which is favorable for the absorbing of acidic CO_2 molecules.

Apart from the CO_2 adsorption, the development of new energy sources with zero CO_2 emission is the way to reduce CO_2 emissions for long-term. The products of emerging technologies, such as fuel cells and metal–air batteries, have been widely considered as the most promising alternatives to conventional energy sources due to their high efficiency, no pollution, and short construction period.[6-8] The oxygen reduction reaction (ORR) is the major barrier of these creative inventions owing to the inherently sluggish kinetics of the ORR process. Currently, Pt and Pt-based alloys with high current density and activity for ORR are still the best candidate under alkaline, and acidic conditions. However, due to the scarcity, the high cost, as well as the poor durability and methanol tolerance, it is not suitable for large scale commercialization. Much efforts have been done to the development of efficient eletrocatalysts such as lean-Pt catalysts, transition metal catalyst and non-precious metal catalyst.[7,8] Among them, carbon based materials have been regarded as the most potential candidate due to its high surface area, tunable porous structure, excellent electrical conductivity, long term stability and low price compared other materials. Particularly, nitrogen doped carbon materials which can break the electroneutrality of the carbon matrix, can create charge redistribution favorable for oxygen adsorption and reduction.[6,9-14]

The nitrogen doped carbon materials have intrinsic features favorable for CO_2 adsorption and ORR catalysts, the larger surface area and porous structure feature are also important for these applications. For CO_2 adsorption, the porous structure of carbon materials can enable fast gas diffusion and provide high surface area.[1,2,4,5] When it comes to ORR activity, large surface area and porous structural feature can introduce more active sites and facilitate the transportation of electrons and oxygen species.[8,15,16] Compared to traditional method of preparing carbon-based catalysts with direct pyrolysis of the mixed carbon and nitrogen precursors, introduction of multi-porous materials such as mesoporous silica materials or metal-organic framework materials as templating and/or precursors can result in high surface area, porous structure, and more exposed ORR active sites.[7,8,16,17] However, the complex preparation process of mesoporous silica hard template may increase the cost and consume the time. Metal–organic frameworks (MOFs) as a new class of crystalline porous materials with high surface area, large pore volume and uniform pore distribution are unique candidates as precursors and templates for the synthesis of nitrogen doped porous carbon materials.[6,7,9-11,16,18] However, the calcined products of MOFs tends to lose some of the unique features due to the destruction of the frameworks during the calcination. To further maintain the high surface area and porous structure of MOFs through the high temperature pyrolysis, new method can be used to sustain the bone structure of MOFs.

Here, we propose a facile and simple MOFs calcination in molten salt process for the fabrication of microporous graphitic carbon materials. A mixture of eutectic salts NaCl-

$ZnCl_2$ (with a NaCl mole ratio of 33%) are used as template to sustain the bone structure of MOFs.[15] Here ZIF-8 material are chosen as the precursor because it has high surface area, high chemical, and thermal stability. Moreover, the nitrogen source in the ligand can lead to in situ synthesis of nitrogen doped carbon porous materials. Since the eutectic salts has a lower melting temperature around 240 °C, it can enter the pore space of ZIF-8 at a lower temperature and remain liquid during calcination in inert atmosphere. After the high temperature pyrolysis, the mixture of salts can be easily removed leading to nitrogen doped porous carbon materials. Moreover, the salt template which is a green and feasible protocol entering the pore structure of MOFs can help retain the original porous structure of parent MOFs in the obtained carbon materials. Based on the different ratios between eutectic salts of NaCl-$ZnCl_2$ and ZIF-8 during the high temperature pyrolysis, a systematic tuning of BET surface area but with relatively similar nitrogen content and pore size distribution of nitrogen doped carbon materials can be obtained. The ORR activity of the obtained materials increase as the BET surface increases. In addition, this work also show that CO_2 adsorption is not linearly based on the BET surface areas for the nitrogen doped carbon material but based on the nitrogen content

4.2 Experimental Section

4.2.1 Synthesis of ZIF-8 Nanocrystals: The synthesis of ZIF-8 nanocrystals was based on a previous procedure.[13] Typically, $Zn(NO_3)_2 \cdot 6H_2O$ (1.68 g) was dissolved in 80 mL of methanol. A mixture of 2-methylimidazole (3.70 g) with 80 mL methanol was added to the above solution with vigorous stirring for 24 h. The product was separated by

centrifugation and washed thoroughly with methanol for twice, and finally dried overnight at 50 °C.

4.2.2 Synthesis of carbon materials: In a typical approach 500 mg of ZIF-8 was used as precursor. The mixtures with varied ratios between sodium chloride, zinc chloride and ZIF-8 were freshly prepared by grinding prior to the experiment. The precursor was thoroughly mixed with the salt mixture, transferred to a ceramic crucible, and heat-treated under argon atmosphere in a chamber furnace. All the samples were heated to 900 °C and kept for 3 h at this temperature. After cooling to room temperature, the mostly black, monolithic structure was grinded, washed twice with 10 wt. % HCl, and dried in vacuum at 60 °C overnight.

4.2.3 Electrocatalytic activity measurements: Electrochemical characterization of the catalysts was performed in a conventional three-electrode cell using CHI760D electrochemical workstation (CH Instruments, USA) controlled at room temperature and under atmospheric pressure. Ag/AgCl and platinum wire were used as reference and counter electrodes, respectively. All potentials in this report were converted into reversible hydrogen electrode (RHE).

A ring-disk electrode (RDE) with a glassy carbon disk and a Pt ring was served as the substrate for the working electrode. The catalyst ink was prepared by mixing the catalyst powder (10 mg) with 80 μL Nafion solution (5wt %) and 1.2 ml ethanol in an ultrasonic bath. Then 20 μL of catalyst ink was pipetted onto the GC electrode in 0.1 M KOH. In

0.1M HClO4 solutions, 20 μL of catalyst ink was deposited onto the GC electrode corresponding a catalyst loading of 0.6 mg cm^{-2}. As a comparison, commercial 20 wt. % platinum on Vulcan carbon black (Pt/C from Alfa Aesar) was prepared by blending Pt/C (10 mg) with 80 μL Nafion solution (5wt %) and 1.2 ml ethanol in an ultrasonic bath. A Pt loading about 20 μg cm^{-2} was applied in both alkali and acid conditions.

Linear sweep voltammetry (LSV) polarization curves for the oxygen reduction reaction (ORR) were measured in an oxygen saturated 0.1 M KOH and 0.1 M HClO4 electrolyte with a sweep rate of 10 mV s^{-1} at various rotating speeds from 400 to 2500 rpm. The cyclic voltammogram (CV) were recorded in solutions saturated with either Ar or O_2 gas without rotation with same sweep rate as that of LSV curve. The electron transfer number (n) and kinetic current density (j_K) were analyzed on the basis of Koutecky– Levich equations shown in below:

$$1/j=1/j_L+1/j_K$$

$$j_L=0.62nFCD^{2/3}\upsilon^{-1/6}w^{-1/2}=Bw^{-1/2}$$

$$1/j=1/Bw^{-1/2}+1/j_K$$

where $B=0.62nFC_0 D_0^{2/3} \upsilon^{-1/6}$, j was the measured current density, j_K and j_L were the kinetic- and diffusion-limiting current densities, *w* was the rotation speed, *n* was the

electron transfer number, F was the Faraday constant (F = 96485 C mol^{-1}), C was the bulk concentration of O_2, D was the diffusion coefficient of dissolved oxygen, v was the kinematic viscosity of the electrolyte.

4.2.4 Characterization: The crystal structures of the materials were characterized by X-ray diffractometer (XRD) (D/Max2000, Rigaku) using a Bruker D8-Advance powder diffractometer operating at 40 kV, 40 mA for Cu Kα radiation (λ=1.5406 Å). The morphology and composition of the samples were analyzed with a Tecnai T12 transmission electron microscope (TEM). CO_2 and N_2 adsorption results under a certain temperature and pressure were obtained using an ASAP 2020 analyzer (Micromeritics, USA). The specific surface areas were calculated using the Brunauer–Emmett–Teller (BET) equation from the nitrogen adsorption data in the relative range (P/P_0) of 0.04-0.20. The pore size distribution (PSD) plot was recorded from the adsorption and desorption branch of the isotherm based on the Barrett–Joyner–Halenda (BJH) and Horvath-Kawazoe (H-K) model. The elemental analysis was performed in UCR.

4.3 Results and Discussion

Eutectic salts NaCl-$ZnCl_2$ (with a NaCl mole ratio of 33%) are used as template to mix with ZIF-8. Different ratios between eutectic salts and ZIF-8 are prepared from 1:1, 1:2, 1:3, 1:4, 1:5, 1:10 and 1: 15. After the grinding of eutectic salts and ZIF-8, they are calcined at 900 °C in Ar atmosphere. Then the obtained materials are etched with 10 wt.% HCl for about 12 hours. The powder X-ray diffraction (PXRD) analyses

demonstrate that after high temperature pyrolysis and etching, the obtained materials show graphitic carbon with the (002) and (100) planes appearing at diffraction peaks of 26.1° and 43.2° (Figure 4.1).[19,20] As the ratio between eutectic composition salts and ZIF-8 increase, the crystallinity remains similar with only a minor decrease. Transmission electron microscopy (TEM) images show that ZIF-8 with an average size of 50 nm to 70 nm were first synthesized as the precursors. Through the direct pyrolysis of composites with a ratio between eutectic composition salts and ZIF-8 about 1: 10 at 900 °C in Ar atmosphere, the obtained materials consist of nanoparticles with a micro pore dominated structure (Figure 4.2). The porous features are favourable for large surface areas, excellent electrolyte, and oxygen diffusion for ORR activity.[16,21,22]

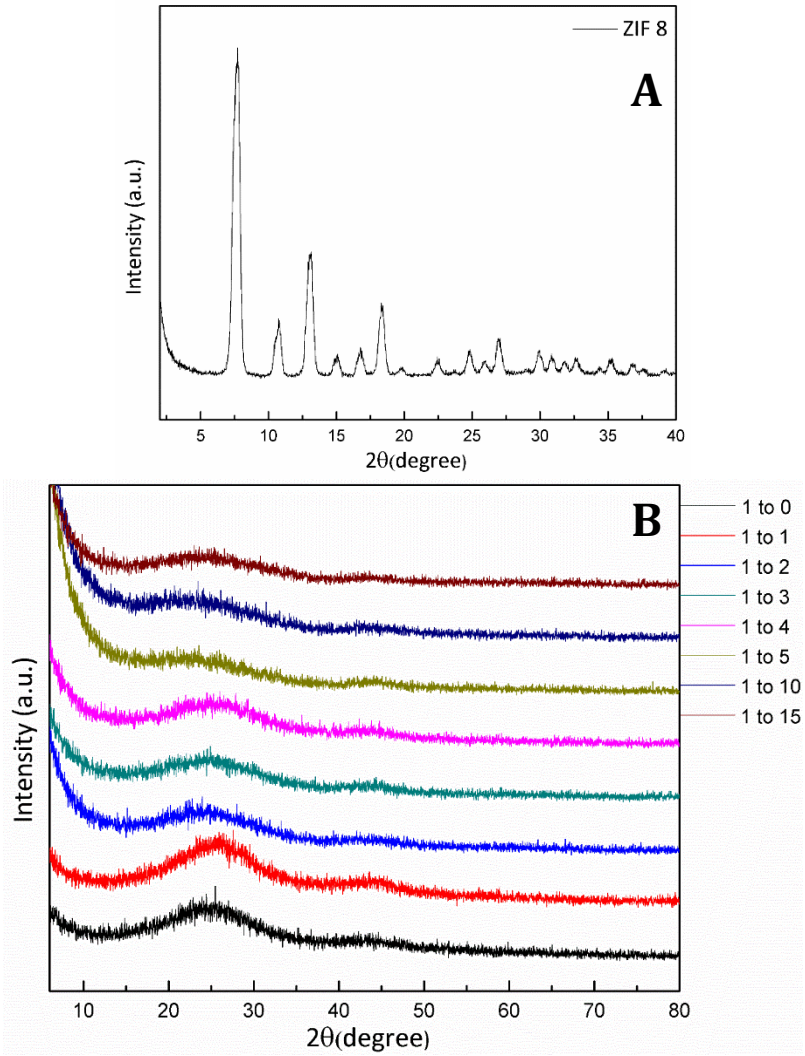

Figure 4.1 XRD patterns of ZIF-8 nanoparticle (a), obtained porous carbon materials (b).

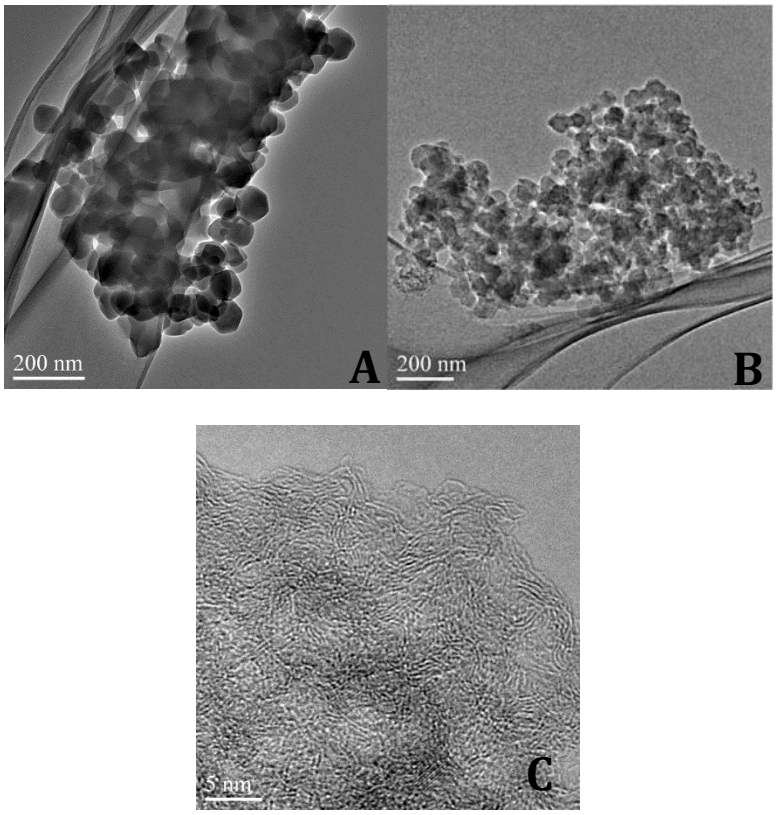

Figure 4.2 TEM and HRTEM images of a), ZIF-8 nanoparticles, b,c) carbon nanoparticles obtained from pyrolysis of composites with eutectic salts and ZIF-8 ratio of 1:10.

The obtained porous carbon materials have been shown to possess excellent ORR activity and durability. The electrocatalytic ORR performance are investigated under alkaline conditions (0.1 m KOH). To explore the ORR performance of the materials obtained from different ratio between melting salts and ZIF-8, rotating disk electrode (RDE) voltammetry was performed at 1600 rpm. The RDE curves for different ratio obtained porous carbon materials and commercially available 20 wt. % Pt/C are shown in Figure

4.3. The onsite potential of carbon materials increases as the ratio between melting salts and ZIF-8 increases. When the ratio is 1:10, the onsite potential of this carbon material reaches the highest level. The results also indicate that the 1:10 ratio material show a relatively larger onsite potential and have-wave potential than that of 20 wt.% Pt/C. RDE voltammetry was performed at various rotation rates in O_2-saturated 0.1 m KOH solutions. The electron transfer number (n) as a function of potential can be calculated from the K-L plots showing a four-electron transfer pathway for ORR catalysis, corresponding to the complete reduction of oxygen into water.[19,20,22,23]

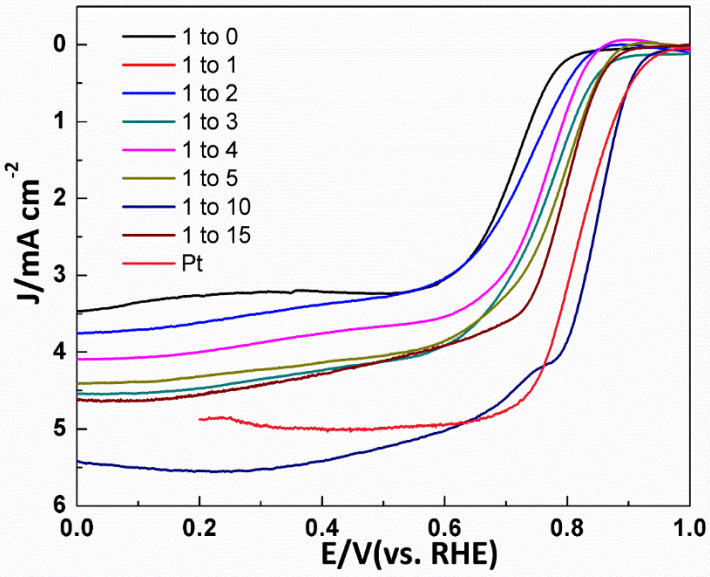

Figure 4.3 RDE voltammograms of carbon nanoparticles catalysts pyrolyzed by heating the mixtures containing different molar ratio of molten salts and ZIF-8 in O_2-saturated 0.1 M KOH.

Notably, the 1:10 material also shows better tolerance toward methanol than that of Pt/C. Subsequently, the chronoamperometric responses of the 1:10, and Pt/C were measured with the introduction of methanol to evaluate the methanol tolerance of the as-prepared porous carbons. As shown in Figure 4.4a, a strong response was observed for the Pt/C when methanol was added. However, the responses for the 1:10 under the same treatment were almost negligible, indicating that the as-prepared materials had substantially more methanol tolerance than the Pt/C. The stability test is conducted for 1:10 material by chronoamperometry at a constant voltage of ~0.55V (vs. RHE) in O_2-saturated 0.1 M KOH solution at a rotation rate of 1600 rpm. As shown in Figure 4.4b, the 1:10 material exhibits a very slow attenuation and a high relative current of over 90% are remained after 100,000 s in both solutions. However, the ORR current on Pt/C declines sharply both in alkaline and acidic solutions as measured at the same conditions.

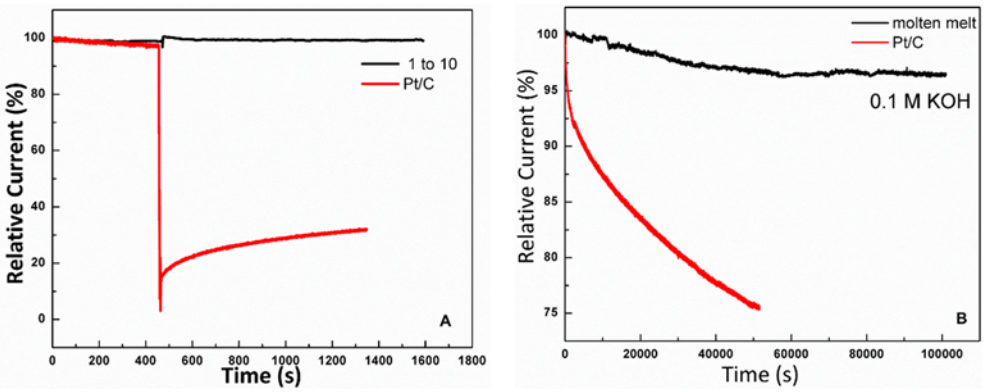

Figure 4.4 Methanol crossover tests by introducing 3 M methanol into the electrolyte at 400 s. The chronoamperometric responses (i–t) of carbon nanoparticles.

It is interesting phenomenon that the ORR activity of the material increases as the ratio between the melting salts and ZIF-8 increases. As is known that two crucial factors governing the performance of carbon-based ORR catalysts.[22] One is the intrinsic nature of the active sites that are determined by the elemental composition and the interactions between different components. Another important factor is the large surface area and porous structural feature that can introduce more active sites and facilitate the transportation of electrons and oxygen species. The intrinsic nature of the active sites in the melting salts with ZIF-8 obtained materials are based on the nitrogen doping into the carbon matrix, creating positive charge in the adjacent carbon atoms which are favorable for oxygen adsorption and reduction. Elemental analysis is performed to analyze the content of the nitrogen in the obtained carbon materials (Table 4.1). From the table, we can see that the nitrogen content of the carbon materials obtained from different ratio do not vary much from each other. Relatively about 12 wt.% nitrogen content exist in the final carbon materials.

Table 4.1 Elemental compositions of carbon nanoparticles by elemental analysis.

Zif 8 to (mixture of NaCl(33%)-$ZnCl_2$) (Weight ratio)	% (wt) N	% (wt) C
1 to 0	13.43346024	71.2537384
1 to 1	11.94606781	77.3635025
1 to 2	11.59226036	78.36100006
1 to 3	10.85015488	79.38744354
1 to 4	11.31420803	79.29163361
1 to 5	11.78593254	78.95396423
1 to 10	11.7532444	76.50777435
1 to 15	9.919985771	77.99240875

Then the surface area and porous structure of the materials are investigated by the N_2 adsorption–desorption isotherms. The BET surface area values of the materials increase as the ratio increases (Table 4.2). Maybe it is because that as the ratio of melting salt increases, more salts can enter and surround the ZIF-8 during high temperature pyrolysis thus, it can better sustain the 3D framework of the MOFs. Notably, the ratio of the 1: 10 material show a relatively high surface area about 3000 m^2/g. It is interesting that the pore size distribution of all the materials fall into 0.3 nm and 1.2 nm (Figure 4.5). It is because such pore sizes are in accordance with the window size 3.4 Å and cavity size 11.6 Å of ZIF-8, suggesting that the melting salt entering ZIF-8 precursor can help retain the pore structure and prevent the collapse of the of parent MOFs during calcination. Since the nitrogen content of the materials are relatively similar between the different materials, the increasing BET surface area play an important role for the increasing ORR activity. This method also presents a facile and simple way to systematic control the surface area of carbon materials based on the different ratio of salts added.

Table 4.2 A comparison of CO_2 adsorption performance and BET surface areas between the carbon nanoparticles

Zif 8 to (mixture of NaCl(33%)-$ZnCl_2$) (Weight ratio)	CO_2 273K cm^3/g	CO_2 298K cm^3/g	BET surface area m^2/g	Qst Value for CO_2 (KJ/mol)
1 to 0	112	77	897	32.819
1 to 1	131	80	1086	32.319
1 to 2	132	81	1369	31.302
1 to 3	131	78	2141	31.750
1 to 4	126	72	2215	32.259
1 to 5	128	65	2261	32.321
1 to 10	122	69	3000	31.455
1 to 15	126	70	2397	32.766

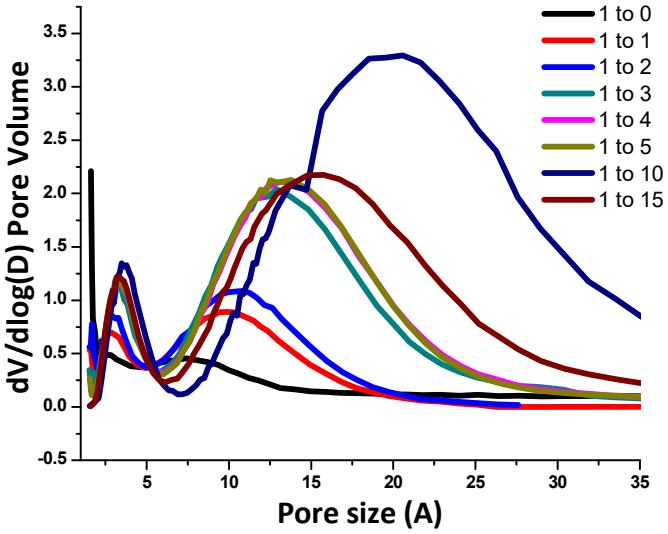

Figure 4.5 Pore size distribution of carbon nanoparticles.

Due to the high level of nitrogen doping into the carbon materials and the large micropore volume, the materials are evaluated for their CO_2 adsorption.[3,24] CO_2 adsorption isotherms were collected at 273 and 298 K at 1 bar. The results clearly demonstrate the outstanding CO_2 uptake capacity of the carbon materials. At 273 K and 1 bar, the 1:10 ratio material achieves a remarkable value of 122 cm^3/g. It also shows a high uptake about 69 cm^3/g at 298 K. Such a high adsorption capacity is among the best of the reported carbons under similar conditions.[1-3,24,25] It is also interesting that the CO_2 uptake value for the different ratio do not vary too much but around the similar values. It is usually regarded that the high CO_2 uptake are correlated with two controlling parameters, the ultra-fine porous structure, and the heteroatom content.[2,24,25] The nitrogen contents with the different ratio obtained carbon materials are similar with each other.

However, the surface areas are increasing with the ratio increases. In order to have a better understanding about the strength of the interaction between CO_2 molecules and the carbon materials, the isosteric heat of adsorption (Qst) was calculated by fitting the CO_2 adsorption isotherms at 273 and 298 K for each sample to the Clausius–Clapeyron equation (Table 4.2). The Qst value for the all carbon materials remain similar. The CO_2 interaction with surface heterogeneity and the confinement of CO_2 molecules in the ultra-fine pores are similar between these materials. The results in this work propose that the increasing surface area do not always result in higher CO_2 uptake values.

4.4 Conclusion

In summary, the synthesis of nitrogen doped porous carbon materials has been demonstrated by a facile, green, and effective approach. The carbon materials are synthesized by pyrolysis of eutectic composition mixture salts and ZIF-8. The ratio between salts and ZIF-8 can be adjusted to tailor the surface areas to achieve the best ORR activity. As the ratio increases, the obtained carbon materials contain similar nitrogen content but increasing surface area. This method represents a way to systematic tune the surface area of obtained materials. In addition, this work also show that CO_2 adsorption is not linearly based on the BET surface areas for the nitrogen doped carbon material. The nitrogen content, the Qst value all influencing the CO_2 uptake capacity.

4.5 Reference

(1) Ashourirad, B.; Arab, P.; Islamoglu, T.; Cychosz, K. A.; Thommes, M.; El-Kaderi, H. M. *J. Mater. Chem. A* **2016**, *4*, 14693.

(2) Tian, W.; Zhang, H.; Sun, H.; Suvorova, A.; Saunders, M.; Tade, M.; Wang, S. *Adv. Funct. Mater.* **2016**.

(3) Li, K.; Tian, S.; Jiang, J.; Wang, J.; Chen, X.; Yan, F. *J. Mater. Chem. A* **2016**, *4*, 5223.

(4) Gong, J.; Lin, H.; Antonietti, M.; Yuan, J. *J. Mater. Chem. A* **2016**, *4*, 7313.

(5) Paraknowitsch, J. P.; Thomas, A. *Energy & Environmental Science* **2013**, *6*, 2839.

(6) Lai, Q.; Zhao, Y.; Liang, Y.; He, J.; Chen, J. *Adv. Funct. Mater.* **2016**.

(7) Mahmood, A.; Guo, W.; Tabassum, H.; Zou, R. *Advanced Energy Materials* **2016**.

(8) Nie, Y.; Li, L.; Wei, Z. *Chem. Soc. Rev.* **2015**, *44*, 2168.

(9) Lin, Q.; Bu, X.; Kong, A.; Mao, C.; Bu, F.; Feng, P. *Adv. Mater.* **2015**, *27*, 3431.

(10) Kong, A.; Lin, Q.; Mao, C.; Bu, X.; Feng, P. *Chem Commun (Camb)* **2014**, *50*, 15619.

(11) Lin, Q.; Bu, X.; Kong, A.; Mao, C.; Zhao, X.; Bu, F.; Feng, P. *J. Am. Chem. Soc.* **2015**, *137*, 2235.

(12) He, Y.; Gehrig, D.; Zhang, F.; Lu, C.; Zhang, C.; Cai, M.; Wang, Y.; Laquai, F.; Zhuang, X.; Feng, X. *Adv. Funct. Mater.* **2016**.

(13) Chen, Y. Z.; Wang, C.; Wu, Z. Y.; Xiong, Y.; Xu, Q.; Yu, S. H.; Jiang, H. L. *Adv. Mater.* **2015**, *27*, 5010.

(14) Gu, W.; Hu, L.; Li, J.; Wang, E. *J. Mater. Chem. A* **2016**, *4*, 14364.

(15) Pampel, J.; Fellinger, T.-P. *Advanced Energy Materials* **2016**, *6*, 1502389.

(16) Zhu, Q. L.; Xia, W.; Akita, T.; Zou, R.; Xu, Q. *Adv. Mater.* **2016**, *28*, 6391.

(17) Sasan, K.; Kong, A.; Wang, Y.; Chengyu, M.; Zhai, Q.; Feng, P. *J. Phys. Chem. C* **2015**, *119*, 13545.

(18) Kong, A.; Mao, C.; Lin, Q.; Wei, X.; Bu, X.; Feng, P. *Dalton Trans.* **2015**, *44*, 6748.

(19) Gong, K.; Du, F.; Xia, Z.; Durstock, M.; Dai, L. *Science* **2009**, *323*, 760.

(20) Liang, J.; Jiao, Y.; Jaroniec, M.; Qiao, S. Z. *Angew. Chem. Int. Ed.* **2012**, *51*, 11496.

(21) Li, Y.; Zhou, W.; Wang, H.; Xie, L.; Liang, Y.; Wei, F.; Idrobo, J. C.; Pennycook, S. J.; Dai, H. *Nat. Nanotechnol.* **2012**, *7*, 394.

(22) Wang, Y.; Kong, A.; Chen, X.; Lin, Q.; Feng, P. *ACS Catal.* **2015**, *5*, 3887.

(23) Wang, S.; Zhang, L.; Xia, Z.; Roy, A.; Chang, D. W.; Baek, J.-B.; Dai, L. *Angew. Chem. Int. Ed.* **2012**, *51*, 4209.

(24) Aijaz, A.; Fujiwara, N.; Xu, Q. *J. Am. Chem. Soc.* **2014**, *136*, 6790.

(25) Zhai, Q. G.; Bu, X.; Mao, C.; Zhao, X.; Feng, P. *J. Am. Chem. Soc.* **2016**, *138*, 2524.

CHAPTER FIVE: OUTLOOK

5.1 Introduction

Developing non-precious metal catalysts (NPMCs) is a well-known strategy to replace the platinum-based catalysts for the oxygen reduction reactions (ORR) at the cathode of fuel cells, metal–air batteries and air-breathing cathodes in industrial electrocatalytic processes.[1,2]

There are two crucial factors governing the performance of carbon based ORR catalysts.[2] One is the intrinsic nature of the active sites that are determined by the elemental composition and the interactions between different components.

Among the various catalysts, transition metal−nitrogen-carbon (Me−N−C) containing materials, especially Fe−N−C, have been demonstrated as a family of promising NPMCs due to their high ORR activity in both alkaline and acidic electrolytes.[3,4] In addition, a series of heteroatom doped carbon-based catalysts have also been generated.[5-7] For example, it was proposed that the N with higher electronegativity (electronegativity of nitrogen: 3.04) than that of C atom (electronegativity of carbon: 2.55) may create the positive charge density on the adjacent carbon atom which could be favorable for the adsorption of oxygen.[3] In addition, other theoretical studies suggest that breaking the eletroneutrality of graphitic materials is also important for increasing ORR activity. In this way, both electron-rich (e.g., N) and electron-deficient (e.g. P, B) can create charged

active sites for oxygen adsorption.[2] When it comes to sulfur or selenium, whose electronegativities are similar to the carbon (electronegativity of sulfur: 2.58, electronegativity of selenium: 2.55), Zhang et al. proposed that it is the spin density rather than atomic charge density plays an important role in determining the catalytic active sites through using DFT calculation.[8]

Another important factor is the large surface area and porous structural feature that can introduce more active sites and facilitate the electrons and oxygen species transportation.

Compared to traditional method of preparing carbon based catalysts with direct pyrolysis of the mixed carbon, nitrogen, and transition-metal precursors, introduction of multi-porous materials such as metal-organic framework materials or mesoporous materials as templating and/or precursors can result in high surface area, porous structure and more exposed ORR active sites.[9,10]

5.2 Some preliminary Results:

With these design strategies, we have synthesized several ORR catalysts based on iron-nitrogen doped porous carbons materials and heteroatom doped carbon materials with either mesoporous silica nanoparticles as templates or MOFs as templates and precursors. For example, we have synthesized hierarchical porous Fe-N-doped hollow carbon-nanoshells with about 40 nm cavities by using CdS@mSiO_2 core-shell structured

materials as hard templates.[11] CdS@mSiO_2 denotes as CdS nanoparticle core and mesoporous SiO_2 (mSiO_2) shell. The obtained porous and hollow carbon-nanoshells demonstrated excellent electrocatalytic activity for oxygen reduction reaction (ORR) due to the use of a Fe-Nx containing precursor, hierarchical porous structural features and perhaps most importantly the hollow shell design strategy. Both the onset potential (0.98 V) and half-wave potential (0.85 V) are more positive than that of commercial Pt/C in alkaline conditions with the same catalyst loading (0.1 mg cm^{-2}). In acidic conditions, the onset and half-wave potentials of carbon-nanoshell electrodes are only 30 and 20 mV less than that of commercial 20 wt. % Pt/C, respectively.

In addition, Nitrogen−sulfur−iron-doped porous carbon material with high surface area (1026 m^2 g^{-1}) and large pore size was synthesized by the pyrolysis of hemoglobin, an abundant and inexpensive natural compound, with mesoporous silica foam (MS) as a template and thiocarbamide (TCA) as additional sulfur source in an argon atmosphere.[12] The electrocatalytic tests show that the materials exhibited better catalytic activity and long-term stability and higher current density and resistance than a commercial 20 wt. % Pt/C in alkaline media for ORRs. Such excellent performance could be attributed to more accessible active sites of Fe−N_4 as well as high concentrations of dual-doping heteroatoms (N and S) that could increase the catalytic activity perhaps due to induced charge distribution on the materials.

Due to their diverse pore structures and designable framework compositions, metal–organic frameworks (MOFs) have been explored as both templates and precursors for making electrocatalytic materials with distinctive structural features and unique properties.[1] By one-step pyrolysis of a unique "cage-in-cage" cobalt metal–organic framework, nitrogen-doped carbon cubes embedded with numerous metallic Co nanoparticles were obtained.[13] A considerable amount of Co particles was encapsulated in thin carbon shells and formed the core–shell-like Co@C structure. The nanocomposites of Co nanoparticles and nitrogen-doped carbon show electrocatalytic activity with an ORR half-wave potential ($E_{1/2}$) value of 0.76 V.

In addition, our group have developed a new route for the development of nonprecious metal ORR catalysts from stable metalloporphyrinic MOFs.[14] Four cubic zirconium-porphyrin frameworks, CPM-99(H2, Zn, Co, Fe), were synthesized by a molecular-configuration-guided strategy. The materials with Zr_6-polyoxo-cluster and uniformly embedded (metallo)-porphyrin centers could serve as excellent precursors for ORR catalysts. The pyrolytic products not only retain the microcubic morphology of the parent CPM-99 but also possess porphyrinic active sites, hierarchical porosity, and highly conducting networks. As a result, CPM-99Fe-derived carbonization product exhibited high ORR activity (with onset potential of 0.950 and 0.875 V in alkaline and acidic electrolytes, respectively) comparable to 20 wt. % Pt/C catalyst (0.978 and 0.880 V, respectively).

Moreover, our group have also demonstrated the use of alternately conjugated networking method to prepare highly porous heterometalloporphyrin materials of PCN-FeCo, which is the first example of heterometallic porous covalent solids with ordered alternation of iron and cobalt chelate complexes.[15] Its subsequent carbonization gives rise to Fe and Co co-doped azotized-carbon composite of PCN-FeCo/C.[15] It was determined that the PCN-FeCo/C displayed a more positive onset potential (1.00 V) than that of PCN-FeFe/C (0.97 V), and PCN-CoCo/C (0.92 V) in 0.1 M KOH solution. Furthermore, the heterometallic product afforded a half-wave potential of 0.85 V, comparable to that of 20% Pt/C (0.84 V) in 0.1 M KOH solution. As further determined by RDE experiments and relative to the Fe-free product, a significant improvement in activity is also observed with the PCN-FeFe/C sample, as evidenced by positive shifts in onset (from 0.85 to 0.88 V) and half-wave $E_{1/2}$ (from 0.71 to 0.74 V) potentials in 0.1 M $HClO_4$. Again, the binary catalyst PCN-FeCo/C was found to give the highest activity, i.e., the most positive onset (0.90 V) and $E_{1/2}$ (0.76 V) potentials. The ORR polarization curve of the PCN-FeCo/C catalyst in 0.1 M $HClO_4$ was nearly identical to that of the 20 wt. % Pt/C. The prominent performance of the PCN-FeCo/C can be attributed to its advanced features including large surface area, substantial graphitization, and high density of uniformly distributed heterometallic active moieties.

5.3 Future Plans:

As can be seen, Metal–organic frameworks (MOFs) as new classes of crystalline porous materials with high surface area, large pore volume and uniform pore distribution can be suitable candidates as precursors and/or templates for the formation of high quality porous carbons for ORR application. The diversity in types of metal ions and organic ligands in MOFs with cavities and pore spaces make them versatile precursors and/or templates for the synthesis of carbon/metal oxide composites and doped carbon-metal materials.[9,13] Metals play an essential role in the catalytic properties of MOFs derived porous carbons. Heterometallic MOFs can have a better control over the composition in the final MOFs derived metal incorporated carbon materials.[1,15] This could bring much desired advantageous over random blending and nanocasting methods.[15] Recently, our group have successfully synthesized a large family of cluster based MOF materials with diverse chemical compositions (Figure 5.1).[16] In future work, firstly we plan to fully explore how the different metal combinations impact the electrocatalytic properties of the formed metal-doped carbon materials. Based on the results, with the introducing of different organic precursors such as organic molecules with N, B, S, Se, or P heteroatoms containing species into the pore of the heterometallic systems, a large family of doped heterometallic porous carbon based materials will be developed and characterized. A systematic study on their electrocatalytic properties will be fully investigated and a thorough understanding on their working mechanism will be developed. With the obtained results, by using the best doped heterometallic system, the hierarchically

ordered porous carbon materials will be developed by in-situ growing MOF in the channel of mesoporous materials like Si foams. Through carbonization (with or without the introduction of more organic species into the materials), a family of hierarchical porous carbon materials with different structural feature can be synthesized and their different properties will be characterized.

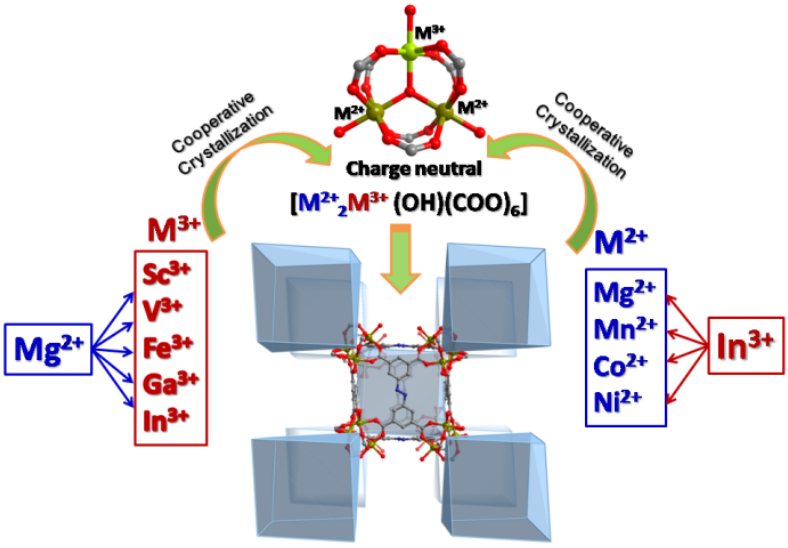

Figure 5.1 Realized M^{2+} and M^{3+} combinations for CPM-200s.

In addition to the above-mentioned approaches, there are some open coordination sites on the metals species or functional groups in the ligands of the developed MOFs.[17,18] Those open coordination sites can function as the specific interaction sites and be further utilized for the post-synthesis to introduce different heteroatoms with different coordination environments and different functionalities. Targeted species, like metals, heterometals and heteroatoms can be integrated into the targeted materials via different

interactions to further maximize the electrocatalytic activities of the synthesized materials.

In addition to develop highly functionalized materials, thorough understanding of the materials' active sites, the interactions of reactive and intermediate species during oxygen reaction process will be pursued with team efforts in this proposed research. We anticipate that the developed hierarchical porous carbon materials with different local environments and local structural features can have great impacts on their catalytic activities. These will be fully characterized and studied. The affinity of reacting moieties intermediates (O_2, O_2*, OH*, OOH*, H^+, H_2O, etc.) with the different active sites, like metal centers and other doping atoms will be studied and revealed via theoretical calculations (DFT) together with experimental efforts.

5.4 Reference

1. Mahmood, A.; Guo, W.; Tabassum, H.; Zou, R. *Adv. Energy Mater.* **2016**, DOI: 10.1002/aenm.201600423.
2. Nie, Y.; Li, L.; Wei, Z. *Chem. Soc. Rev.* **2015**, *44*, 2168.
3. Gong, K.; Du, F.; Xia, Z.; Durstock, M.; Dai, L. *Science* **2009**, *323*, 760.
4. Li, Y.; Zhou, W.; Wang, H.; Xie, L.; Liang, Y.; Wei, F.; Idrobo, J. C.; Pennycook, S. J.; Dai, H. *Nat. Nanotechnol.* **2012**, *7*, 394.
5. Liang, J.; Jiao, Y.; Jaroniec, M.; Qiao, S. Z. *Angew. Chem. Int. Ed.* **2012**, *51*, 11496.
6. Zheng, Y.; Jiao, Y.; Ge, L.; Jaroniec, M.; Qiao, S. Z. *Angew. Chem. Int. Ed.* **2013**, *52*, 3110.
7. Wang, S.; Zhang, L.; Xia, Z.; Roy, A.; Chang, D. W.; Baek, J.-B.; Dai, L. *Angew. Chem. Int. Ed.* **2012**, *51*, 4209.
8. Zhang, L.; Xia, Z. *J. Phys. Chem. C* **2011**, *115*, 11170.
9. Aijaz, A.; Fujiwara, N.; Xu, Q. *J. Am. Chem. Soc.* **2014**, *136*, 6790.
10. Liang, H. W.; Wei, W.; Wu, Z. S.; Feng, X.; Mullen, K. *J. Am. Chem. Soc.* **2013**, *135*, 16002.
11. Wang, Y.; Kong, A.; Chen, X.; Lin, Q.; Feng, P. *ACS Catal.* **2015**, 5, 3887.
12. Sasan, K.; Kong, A.; Wang, Y.; Chengyu, M.; Zhai, Q.; Feng, P. *J. Phys. Chem. C* **2015**, *119*, 13545.

13. Kong, A.; Mao, C.; Lin, Q.; Wei, X.; Bu, X.; Feng, P. *Dalton Trans.* **2015**, *44*, 6748.

14. Lin, Q.; Bu, X.; Kong, A.; Mao, C.; Zhao, X.; Bu, F.; Feng, P. *J. Am. Chem. Soc.* **2015**, *137*, 2235.

15. Lin, Q.; Bu, X.; Kong, A.; Mao, C.; Bu, F.; Feng, P. *Adv. Mater.* **2015**, *27*, 3431.

16. Zhai, Q. G.; Bu, X.; Mao, C.; Zhao, X.; Feng, P. *J. Am. Chem. Soc.* **2016**, *138*, 2524.

17. Li, B.; Zhang, Y.; Ma, D.; Ma, T.; Shi, Z.; Ma, S. *J. Am. Chem. Soc.* **2014**, *136*, 1202.

18. Shakeri, M.; Klein Gebbink, R. J. M.; de Jongh, P. E.; de Jong, K. P. *Angew. Chem. Int. Ed.* **2013**, *52*, 10854.